THERMOMECHANICAL MANUFACTURING OF POLYMER MICROSTRUCTURES AND NANOSTRUCTURES

A Dissertation
Presented to
The Academic Faculty

by

Harry D. Rowland

In Partial Fulfillment
of the Requirements for the Degree
of Doctor of Philosophy in the
George W. Woodruff School of Mechanical Engineering

Georgia Institute of Technology
May 2007

THERMOMECHANICAL MANUFACTURING OF POLYMER MICROSTRUCTURES AND NANOSTRUCTURES

Approved by:

Dr. William P. King, Advisor
George W. Woodruff School of Mechanical Engineering
Georgia Institute of Technology

Dr. Cliff Henderson
School of Chemical & Biomolecular Engineering
Georgia Institute of Technology

Dr. Samuel Graham
George W. Woodruff School of Mechanical Engineering
Georgia Institute of Technology

Dr. Ken Gall
School of Materials Science & Engineering
Georgia Institute of Technology

Dr. Ting Zhu
George W. Woodruff School of Mechanical Engineering
Georgia Institute of Technology

Date Approved: March 9, 2007

ACKNOWLEDGEMENTS

This document has been many years in the making and would not have been accomplished without the constant support from family, friends, colleagues, and collaborators.

I would first like to thank my advisor Bill King for the doors of opportunity that he has continually opened for me. Through his efforts paving the way for collaborative research around the world, Bill has presented me with research opportunities and life experiences that I could not have imagined when I signed on this project over 4 years ago. Samuel Graham has always taken time to discuss applied research and encourage my entrepreneurial musings. Cliff Henderson has provided invaluable advice and access to equipment that enabled much of my experimental work. Ting Zhu has continually made himself available as a committee member. Ken Gall has likewise lent his flexibility to my benefit and provided valuable advice on career paths.

Much of my time in Atlanta has not really been in Atlanta. I am indebted to the many folks at Sandia National Laboratories who kindly tolerated my continual prodding to advance my simulations. Randy Schunk, Amy Sun, Allen Roach, Tom Baer, and Rekha Rao never hesitated to lend their experience and efforts to assist my sometimes quixotic hopes for simulation results. Chris Monroe made sure I felt like a fellow staff member. John Emerson continually looked after me. I enjoyed the company of Chris Brotherton and Robert Butler helping me through many frustrating days staring at the glare of the monitor.

The staff and members of SFI at Trinity College Dublin welcomed me with open arms to excellent facilities and an even better community of minds. Their hospitality and

humor throughout my days taking data in the dungeon helped me enjoy the long hours in pursuit of data. Graham Cross was phenomenal. He lent his time, brain power, friendship, and home to help me succeed. Barry O'Connell's guidance, friendship, and lucky charms allowed me to go from complete lab novice to expert user in mere weeks. Jason Kilpatrick's technical support and friendship refreshed my optimism during stressful times.

Above all, I would like to thank my friends and colleagues at Georgia Tech. Throughout classes, qualifiers, and research, all my friends and co-workers at GT have truly created a positive community to work and live in. Their unwavering support along every step of this journey has been instrumental to my success. I would have quit this thing long ago without the joy that everyday at the office brought. Brent Nelson, Joe Charest, and Tanya Wright are like family. Through our struggles and successes we made bonds for life. Fabian, Jay Lee, Keunhan, KJ, Marcus, Fabian, Shubham, and Andrew have all helped make our research group a fun, supportive environment. Graduates Dr. Eileen Moss, Dr. Jiann Su, and Mike Schmittdiel have all helped me immensely through qualification studying, dissertation advice, lab assistance, and a bit of fun in between. Dr. James Nichols brought me here and continues to serve as a friend and mentor. Terri Keita has always lent a helping hand, an honest word, and a good laugh.

And last but most definitely not least, I am forever indebted to my love, Natalya Zlobin, and my most amazing family. All the inspiration I need, the role models to follow, the heroes to look up to, and the friends to turn to have been right next to me all along the way. I am truly blessed and am forever thankful for the great love we share.

TABLE OF CONTENTS

LIST OF TABLES

Page

LIST OF FIGURES

Page

LIST OF SYMBOLS

AC	alternating current
AFM	atomic force microscope
ALE	Arbitrary Lagrangian/Eulerian
CMOS	complementary metal oxide semiconductor
DC	direct current
HEM	hot embossing manufacturing
IC	integrated circuit
LS	Level Set
NIL	nanoimprint lithography
N/MEMS	nano/microelectromechanical systems
PMMA	polymethylmethacrylate
PS	polystyrene
SEM	scanning electron microscopy
SFA	surface force apparatus
WLF	Williams Landel Ferry

nm	nanometer
μm	micrometer
mm	millimeter
cm	centimeter
m	meter
in	inch
Pa	Pascal
sec	seconds
°C	degrees Celsius

A_{fill}	percent area filled
C_1	WLF constant 1
C_2	WLF constant 2

Ca	Capillary number
C_p	heat capacity
E^*	dimensionless small deformation strain tensor
H^*	dimensionless curvature
H	film thickness
$\dot{H}$	time derivative of film thickness
M_C	critical molecular weight
M_W	molecular weight
P	embossing pressure
ΔP	pressure difference across the fluid interface
P^*	dimensionless body force of the embossing load
P_o	characteristic pressure, applied load
P_{rep}^*	dimensionless repulsive force
R_1, R_2	principal radii of curvature
R	universal gas constant
Re	Reynolds number
R_g	polymer radius of gyration
R_{tip}	AFM tip radius
S	indenter width
T	temperature
T_α	α transition temperature
T_β	β transition temperature
T_{emboss}	embossing temperature
T_g	glass transition temperature
T_o	characteristic time
U_o	characteristic speed
W	cavity half width
X_o	characteristic length, tool width
a	dimensionless parameter describing transition to power-law
d^*	dimensionless distance of polymer boundary normal to solid

e^*	dimensionless small deformation volume strain
h_c	cavity height
h_i	initial polymer film thickness
h_r	residual film thickness
n	shear thinning exponent
$\hat{n}$	normal vector
q	conduction heat flux
t	fill time
t_f	time when polymer has covered half master cavity floor
t_h	half the time to onset of filling
t_o	time to onset of filling
t_r	ramp time
v^*	material dimensionless velocity
$v_m{}^*$	mesh dimensionless velocity
Γ^*	dimensionless fluid stress tensor
$\Gamma_s{}^*$	dimensionless elastic stress tensor
α	polymer alpha relaxation
α_T	time shift parameter
β	polymer beta relaxation
$\dot{\gamma}$	second invariant of shear rate tensor
$\dot{\gamma}_{WR}$	shear rate at wall rim
η	polymer viscosity
η_{inf}	infinite shear limit of polymer viscosity
η_o	zero shear limit of polymer viscosity
η_{Rouse}	Rouse polymer viscosity in free space
λ	Lame lambda coefficient
μ	Lame mu coefficient
υ^*	hot embossing manufacturing effective viscosity
ξ_o	distance between polymer entanglements or polymer tube diameter

ρ	density
σ	surface tension
τ	is the embossing time
τ_d	polymer disengagement time
τ_e	polymer relaxation time denoting onset of tube constraint effects
τ_{WR}	shear stress at wall rim
ω	polymer time constant

SUMMARY

Molding is a simple manufacturing process whereby fluid fills a master tool and then solidifies in the shape of the tool cavity. The precise nature of material flow during molding has long allowed fabrication of plastic components with sizes 1 mm – 1 m. Polymer molding with precise critical dimension control could enable scalable, inexpensive production of micro- and nanostructures for functional or lithographic use.

This dissertation reports experiments and simulations on molding of polymer micro- and nanostructures at length scales 1 nm – 1 mm. The research investigates two main areas: 1) mass transport during micromolding and 2) polymer mechanical properties during nanomolding at length scales < 100 nm. Measurements and simulations of molding features of size 100 nm – 1 mm show local mold geometry modulates location and rate of polymer shear and determines fill time. Dimensionless ratios of mold geometry, polymer thickness, and bulk material and process properties can predict flow by viscous or capillary forces, shape of polymer deformation, and mold fill time. Measurements and simulations of molding at length scales < 100 nm show the importance of nanoscale physical processes distinct from bulk during mechanical processing. Continuum simulations of atomic force microscope nanoindentation accurately model sub-continuum polymer mechanical response but highlight the need for nanoscale material property measurements to accurately model deformation shape. The development of temperature-controlled nanoindentation enables characterization of nanoscale material properties. Nanoscale uniaxial compression and squeeze flow measurements of glassy and viscoelastic polymer show film thickness determines

polymer entanglement with cooperative polymer motions distinct from those observed in bulk.

This research allows predictive design of molding processes and highlights the importance of nanoscale mechanical properties that could aid understanding of polymer physics.

CHAPTER 1

INTRODUCTION

Molding is a simple manufacturing process whereby fluid fills a master tool and then solidifies in the shape of the tool cavity. The precise nature of material flow during molding has long allowed fabrication of plastic components with feature sizes typically ranging from 1 mm – 1 m simply and at high volume and low cost. Fabrication of microelectromechanical systems (MEMS) and integrated circuit (IC) components having feature sizes ranging from 100 nm – 100 μm has traditionally followed complex multi-step processing with stringent requirements on lithography for critical dimension control, pattern placement, and defect control. As feature sizes shrink to 10 nm, the demands on resists, masks, and processing equipment may render conventional micro- and nanofabrication methods cost prohibitive. Extending molding and related processes to fabrication of microstructures and nanostructures with feature sizes ranging from 1 nm – 100 μm could facilitate the widespread development and use of nanotechnology-related products.

1.1 Micro- and Nanomolding

Nanoimprint lithography (NIL) and atomic force microscope (AFM) nanoindentation use molding processes to form microstructures and nanostructures. Figure 1-1 shows the molding process during NIL and Figure 1-2 shows the molding process during AFM nanoindentation. NIL is a high resolution, high throughput, thermomechanical

manufacturing alternative to standard silicon based fabrication technologies. In NIL, a nanopatterned master tool having three-dimensional topography embosses a thermoplastic substrate, forming a negative relief of the master in the substrate. NIL offers scalable manufacture of microstructures and nanostructures with resolution better than 10 nm [1] over areas > 100 mm^2 [2]. Recent studies improved NIL resolution below 5 nm [3] while similar nanomolding processes demonstrated molecular scale resolution [4, 5]. Direct-write AFM nanoindentation represents a single, localized nanoimprint process on the order of 10 – 50 nm, whereby a sharp conical tip indents a thin polymer layer. It is possible to parallelize the AFM indentation process to more than 10,000 cantilevers operating in parallel [6].

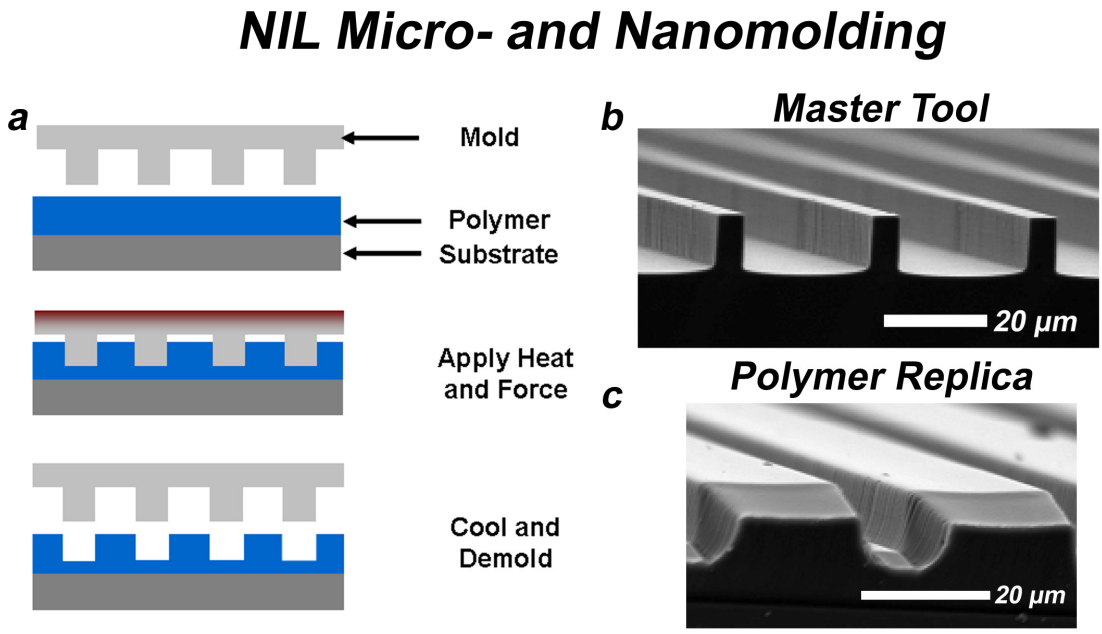

Figure 1-1 (a) Illustration of the molding process in nanoimprint lithography. (b) SEM viewgraph of microfabricated master tool. (c) SEM viewgraph of corresponding polymer replica formed by NIL molding.

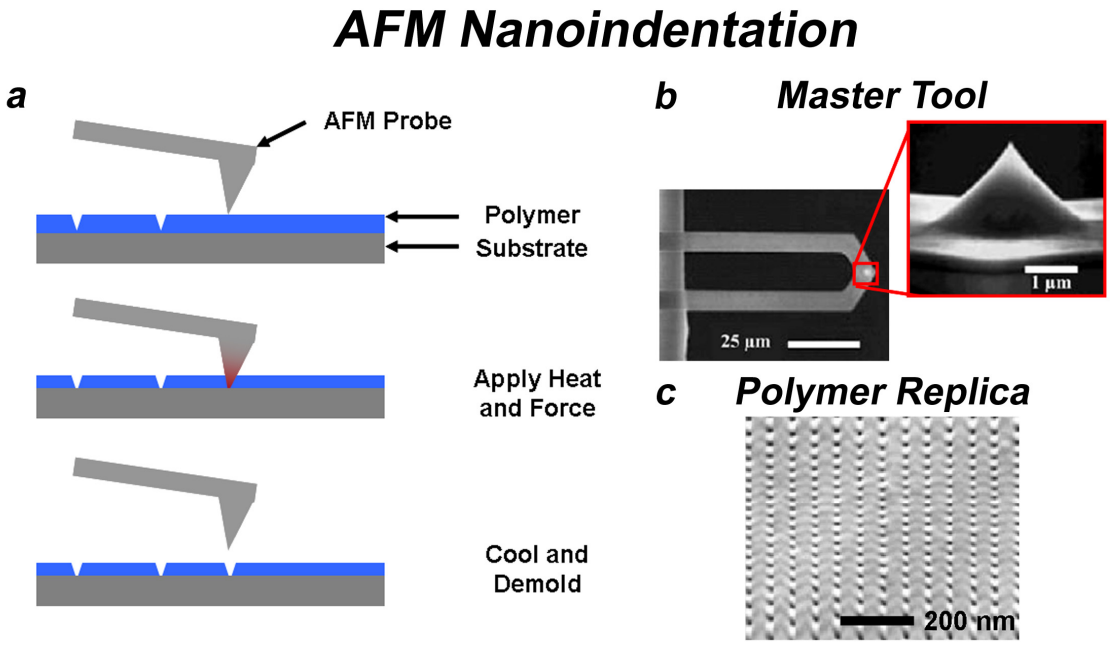

Figure 1-2 (a) Illustration of the molding process in AFM nanoindentation. (b) SEM viewgraph of AFM probe and close-up of AFM tip. (c) AFM scan of corresponding polymer replica formed by parallel AFM nanoindentation. The AFM probe viewgraphs and polymer replica scans are adapted from [7] and [6], respectively.

1.2 Motivation for Micro- and Nanomolding

Traditionally, microfabrication techniques have largely mimicked semiconductor IC fabrication, focusing on surface machining of silicon and other materials compatible with complementary metal-oxide semiconductor (CMOS) circuits. The resulting manufacturing relies on complex multi-step processing with escalating costs and throughput time for feature sizes < 1 µm that could inhibit small to medium volume production of MEMS components and microsystem prototypes. The silicon-specific fabrication also narrows the design window for optimized material selection to match function. Molding or NIL thermomechanical manufacturing offers a low cost, scalable alternative to silicon based microfabrication that capitalizes on the formability of

polymers. Direct forming of polymers through molding can reduce manufacturing steps and eliminate the need for expensive optical enhancement tooling. The available library of deformable polymers with a wide range of material properties enables fabrication of components with tailored mechanical, optical, or chemical properties.

NIL thermomechanical manufacturing has fabricated a variety of nanoelectronics and nanoelectromechanical systems (NEMS)/MEMS applications such as nanometer-scale organic transistors [8], micro-ring optical resonators [9], and microfluidic channels for lab-on-a-chip applications [10]. Perhaps the most promising applications of micro- and nanomolding are in data storage and next generation lithography for IC fabrication. The dominance of magnetic media for data storage is likely limited to data density near 100 Gbit/in^2 due to the superparamagnetic effect [11], though engineering efforts may push this limit to higher densities. Data storage based on molding has shown data density > 100 Gbit/in^2 either directly or by lithographic patterning. Scanning probe data storage based on AFM nanoindentation has demonstrated data density as high as 1 Tbit/in^2 [6], while NIL has patterned cross-bar platinum nanowire arrays for electronically addressable memory that could enable data density > 500 Gbit/in^2 [12].

NIL also holds promise for next generation lithography of feature sizes < 20 nm in IC fabrication. Current extensions of optical projection lithography at 193 nm wavelength include immersion lithography where high index of refraction lenses and fluids increase pattern resolution or extreme ultraviolet lithography where use of 13.5 nm wavelength increases pattern resolution. Both techniques introduce significant new technical challenges of contamination and material development for resists, masks, and lenses, while still requiring tooling and process costs to be less expensive than alternative

technologies. With proper mold fabrication, alignment and overlay capabilities, and defect control during molding and demolding, NIL could pattern high resolution features at high throughput without expensive optical resolution enhancement tooling. Figure 1-3 shows the process flow of NIL and lists technical challenges and active areas of research and development at each stage of the process.

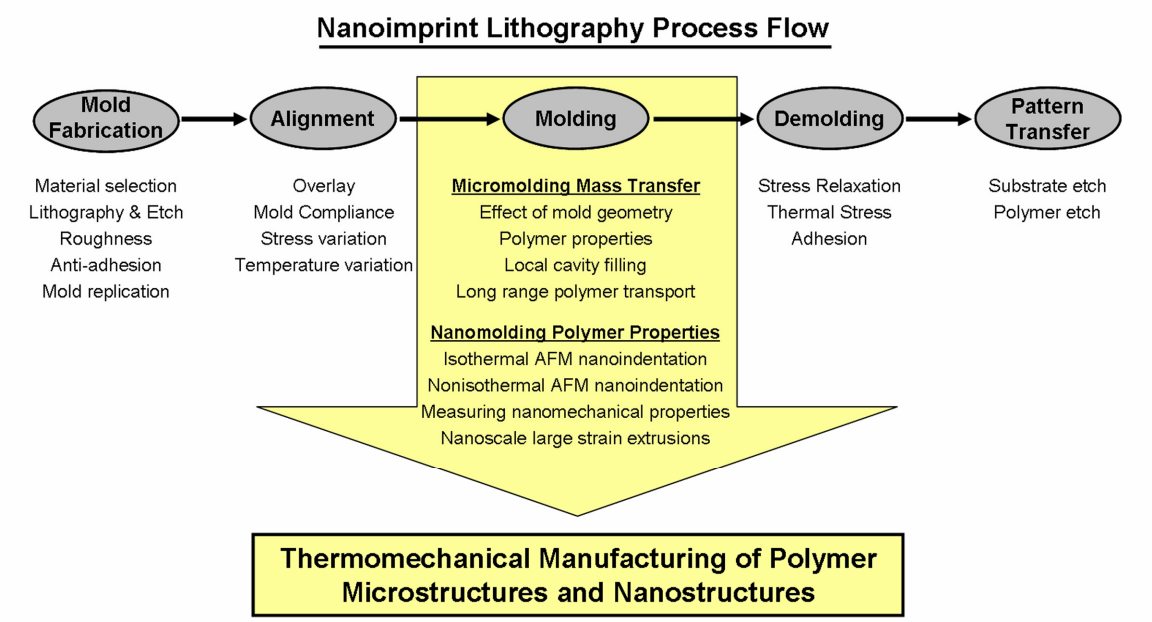

Figure 1-3 Process flow listing technological challenges associated with each stage of NIL for lithographic patterning of IC components. The highlighted molding section lists the research areas of this dissertation to enable predictive process design for NIL with feature sizes 10 nm – 100 μm.

The lack of a first principles understanding of polymer transport during printing is an impediment to production manufacturing with both NIL and AFM nanoindentation. This problem is particularly acute in high resolution nanoimprint and AFM nanoindentation when the nanoscale heat and mass transport properties of the polymer, as well as polymer relaxation processes in confined thin films, are not well understood. Simulations and experiments investigating embossing and imprint lithography from 100 nm – 1 mm offer competing phenomenological explanations of the observed behavior

and there is little agreement about the relative importance of nonlinear elasticity, residual stress, linear and nonlinear viscous flow, compressive stress, and capillary force. Furthermore, flow at small scales has been known to deviate significantly from bulk behavior [13], with conflicting observations of material behavior at film thickness < 100 nm for different measurement methods [14]. The lack of comprehensive understanding of polymer flow at length scales from 100 nm – 1 mm and polymer nanomechanical properties at length scales < 100 nm limits NIL process design to ad-hoc or recipe-based approaches.

1.3 Dissertation Overview

This dissertation reports experiments and simulations performed at Georgia Institute of Technology, Sandia National Laboratories, and Trinity College-Dublin investigating the physics underlying polymer deformation during thermomechanical manufacturing of polymer microstructures and nanostructures. The research is composed of two main areas of interest: one, mass transport during micromolding, and two, polymer mechanical properties during nanomolding at length scales < 100 nm.

The first area of interest investigates polymer flow in microembossing and NIL with feature sizes 100 nm – 1 mm to establish rational process design rules for NIL. Chapter 2 describes microembossing measurements of features 1 – 100 μm that show the influence of mold cavity size, viscous flow, local stress, and shear-thinning phenomena resulting in different shapes of polymer deformation. Chapter 3 presents simulations of microembossing and NIL with feature sizes 100 nm – 1 mm that show dimensionless ratios of mold geometry, polymer thickness, and bulk material and process properties can

predict flow by viscous or capillary forces, shape of polymer deformation, and mold fill time. Chapter 4 describes simulations of embossing molds having irregular spacings and sizes that show individual cavity size dominates replication time, with large differences in individual cavity size resulting in non-uniform, squeeze flow filling. The simulations and experiments of microembossing and NIL allow for predictive design of molding processes from 100 nm – 1 mm to optimize wafer-scale replication.

The second area of interest investigates polymer mechanical properties at length scales < 100 nm during AFM nanoindentation and nanoscale uniaxial compression and squeeze flow measurements. Chapter 5 presents continuum simulations of isothermal AFM nanoindentation that accurately model sub-continuum polymer mechanical response but highlight the need for nanoscale material property measurements to accurately model deformation shape. Chapter 6 describes the development of temperature-controlled nanoindentation to enable nanoscale material property characterization of a wide range of materials and temperature-dependent dynamical properties. Chapter 7 presents temperature-controlled uniaxial compression and squeeze flow measurements of polymer nanomechanical properties that show bulk polymer mechanics accurately predict polymer flow during extrusions from initial film thickness > 100 nm down to 10 nm residual film thickness. Chapter 8 presents similar measurements from initial film thickness < 100 nm and shows evidence of cooperative polymer motions that are distinct from those observed in bulk. The simulations and experiments of nanomolding highlight the importance of nanoscale physical processes distinct from bulk during mechanical processing. Understanding the nanoscale cooperative length scales could enhance the current understanding of polymer physics.

CHAPTER 2

POLYMER DEFORMATION AND FILLING MODES DURING MICROEMBOSSING

This chapter investigates the initial stages of polymer deformation during hot embossing micro-manufacturing at processing temperatures near the glass transition temperature (T_g) of polymer films of sufficient thickness such that polymer flow is not supply-limited. Several stages of polymer flow can be observed by employing stamp geometries of different widths and varying imprint conditions of time and temperature to modulate polymer viscosity. Experiments investigate conditions affecting cavity filling mechanisms and parameters, including apparent polymer viscosity. Stamps with periodic ridges of height and width 4 μm and periodicity 30, 50, and 100 μm emboss trenches into Poly methyl methacrylate films at $T_g - 10$ ºC < $T_{emboss} < T_g + 20$ ºC. Imprint parameters of time, temperature, and load are correlated with replicated polymer shape, height, and imprinted area. Polymer replicates are measured by atomic force microscopy and inspected by scanning electron microscopy. Cavity size and the temperature-dependence of polymer viscosity significantly influence the nature of polymer deformation in hot embossing micro-manufacturing, and must be accounted for in rational process design.

2.1 Introduction

In hot embossing manufacturing (HEM), a silicon micromachined master is pressed into a thermoplastic substrate at elevated temperature, forming a negative relief

replica mold of the master topography in the plastic. Figure 2-1 shows the hot embossing process. HEM can form features as small as 10 nm [1] over wafer-scale areas greater

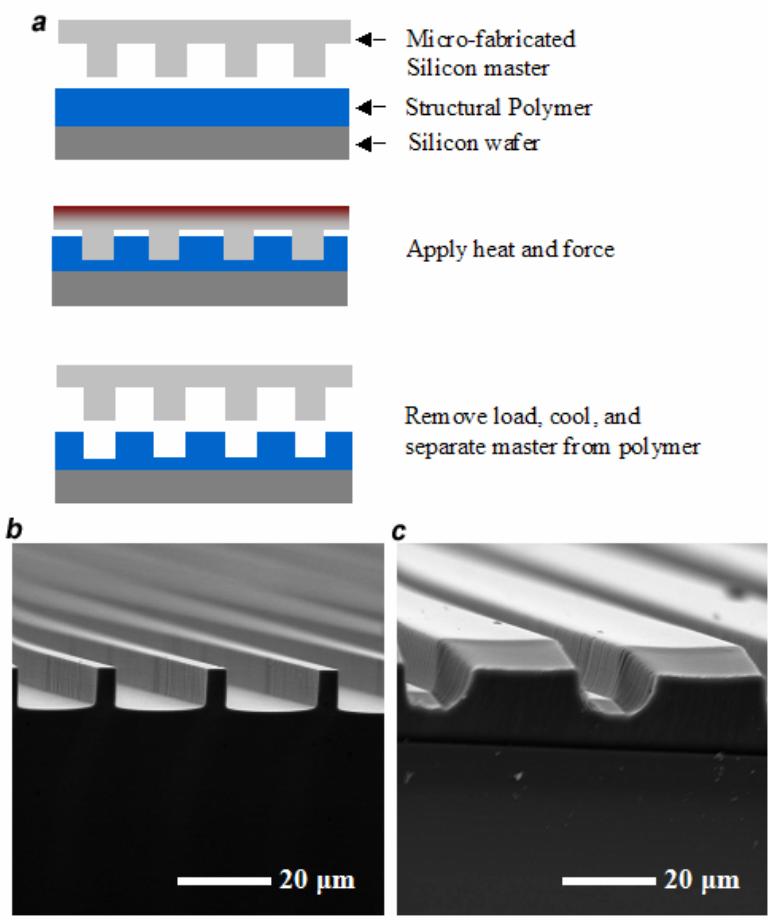

Figure 2-1 (a) Schematic of the hot embossing process (b) SEM micrograph of silicon master (c) SEM micrograph of replicated polymer.

than 1000 cm^2 [2] and thus could enable inexpensive and scalable fabrication of micro/nano-electromechanical systems (M/NEMS). HEM has been used for a wide variety of M/NEMS applications such as fabricating nanometer-scale organic transistors [8], micro-ring optical resonators [9], and microfluidic channels for lab-on-a-chip applications [10]. More recent applications include patterning partially cured polymers for tissue engineering [15] and novel micromachining using embossed thermally

sacrificial materials [16]. Because of its versatility and highly nonstrict materials compatibility requirements, HEM offers the opportunity for direct manufacture of organic microsystems.

Critical to the embossing manufacture of organic microsystems is the deformation and flow of polymer during molding and the fidelity of replication. Only a few groups have investigated polymer flow during microembossing, reporting two general deformation trends. Figure 2-2a shows two modes of polymer deformation: a dual-peak mode with vertically deforming peaks adjacent to the master sidewall, and a single-peak mode where the master cavity fills from the center. Heyderman, *et. al* [17] analyzed viscous flow of thin polymethyl methacrylate (PMMA) films of thickness near 200 nm into cavity depths of 175 nm and widths of 6, 10, and 20 μm at temperatures of 100 ºC above the PMMA glass transition temperature, T_g. Examining the filling of silicon molds at various temperatures and times, Heyderman observed dual-peak deformation where polymer moved into the cavity from cavity borders and deformed vertically along the master sidewalls, with nearly vertical polymer sidewalls. The material in the cavity region prior to embossing did not significantly contribute to vertical deformation but was instead compressed to a point of buckling, causing a downward bow at the cavity center. The authors hypothesized that shear-thinning effects near the cavity sidewalls might account for the increased polymer filling in regions adjacent to the silicon master sidewall. The study, however, focused on hot embossing lithography as a process alternative to photolithography, hence the group used master geometries with isolated cavities of large widths and small heights embossing into thin polymer films. The large

distances required for polymer flow relative to the small amount of polymer available in the thin film possibly restricted the mode of polymer deformation.

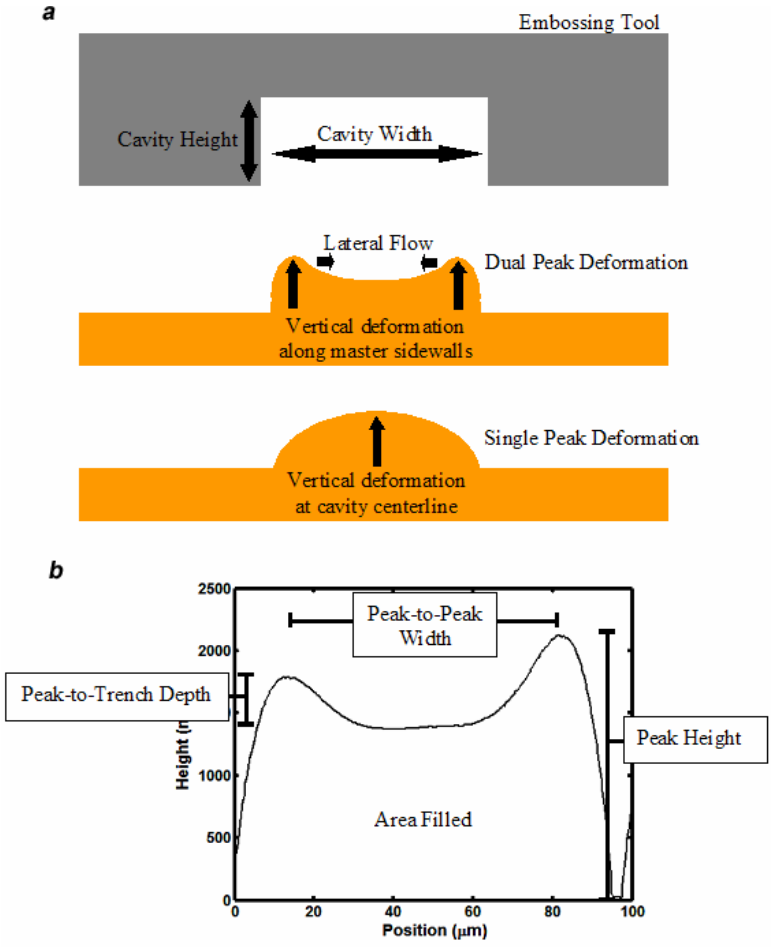

Figure 2-2 (a) Drawing of polymer deformation within master cavity. Polymer peaks deform vertically adjacent to the master sidewalls and spread laterally toward the cavity center. (b) AFM line scan of polymer replicated 100 μm wide cavity with overlaid description of measured dimensions. Dimension not shown is flat length that is measured once conformal filling begins and is the horizontal distance of the flat portion of polymer peak.

A few studies examined polymer flow during HEM where the polymer substrate thickness was much greater than embossed feature size. Scheer, *et. al* [18] investigated cavity filling where sufficient polymer was available to fill the cavity by embossing feature patterns from 400 nm to > 100 μm into polymer films of thickness 500 nm and 4

μm. The polymer was embossed at temperatures much higher than T_g, resulting in viscous polymer flow. Complete filling of pyramid cavities only occurred for 4 μm film thickness. In thick polymer films, the central region of polymer in a master cavity does not undergo a 'buckling' phenomena observed for thin films in previous studies [17]. Buckling occurs in thin films since the polymer is constrained by silicon and cannot distribute stress from flow to adjacent polymer material. Since the thick film has polymer material adjacent to the stress zone, the polymer can undergo efficient stress relaxation. The observation of laterally-flowing polymer peaks to fill large recessed areas was consistent with previously observed double peak flow. A second study [19] also found differences in polymer deformation with large feature sizes and thick films compared to thin film deformation and found that isothermal embossing with feature sizes of > 500 μm at T_g + 30 ºC in thick films (~1200 μm) could be viewed as a biaxial extensional flow of polymer. The study did not report large vertical deformation at the master sidewall for this embossing condition, though a rheological characterization of PMMA [20] showed shear-thinning behavior with a decrease in dynamic viscosity for increasing frequency or temperature. Another group [21] embossed tall 100, 120, and 200 μm diameter cavities into a 500 μm polycarbonate film. Single-peak deformation was observed for embossing at T_g + 30 ºC and at minimum times of 6 min, when the replicated polymer peak had traveled to a height of 50 μm.

Modeling and simulation has been used to understand the physical phenomena in the embossing of nano/micro scale structures. One study [22] simulated hot embossing micro/nano-manufacturing with thin films, including the effects of capillary force and width of stamp groove on the flow behavior during embossing. Simulations showed

double-peak flow for regions of large width, slow printing speeds, and with surface tension as a significant factor. When the feature width decreased, though, the deformation mode changed, with no signs of buckling in the central region of the cavity. For the case where deformation and viscous forces are significantly greater than surface tension forces, the deformation occurs in double polymer peak flow. While the simulations predicted flow behavior seen in previous experiments, the mechanism of polymer deformation was attributed to capillary-driven flow rather than shear-thinning phenomena.

Cross, *et. al* [23] recently investigated the detailed mechanics of deformation of the nanoimprint process in polymer films of thickness less than the height required to fill the embossing tool. This experiment used a simplified single indenter with a cavity of 10 μm diameter and 2 μm height. In films of thickness 450 nm, the characteristic double peak polymer deformation was observed, and the peaks reached the cavity ceiling before lateral filling took place. This deformation was similar to that seen by Heyderman but without strictly vertical sidewalls in the sidewall-adjacent peaks and no central buckling region. The smoothly sloping double polymer peaks also correlate with Jeong's simulation where viscous flow is more dominant. Flow in this thin film case was by outer region filling, where shear thinning and shear heating may be significant. In thicker films (~1.7 μm), low embossing loads resulted in a single high peak of polymer deformation with small deformation external to the cavity while high loads resulted in the characteristic twin-peak mode of polymer deformation at lower peak heights with large deformation external to the cavity. The double peak appears under the rapidly applied high loading condition due to the visco-elastic time dependent response of the polymer

and because insufficient time was allowed for polymer to flow into the cavity. At low loads, a single-peak centerline flow occurred. For this single geometry embossing, imprint time governed feature fidelity, as stress relaxation by deformation before demolding needed to occur for quality replication.

Previous simulations and experiments on embossing into thin films point to polymer flow governed by shear thinning and limited polymer supply. To date, there has been no detailed quantitative study of HEM with feature widths on the order of 1 – 100 μm where flow restrictions due to limited polymer supply is not a dominant effect. However, MEMS fabrication requires 3-dimensional structures in layers thicker than 1 μm. The flow characteristics of embossing under these manufacturing conditions are not well understood, and the lack of fundamental understanding of the polymer transport limits the rational process design in HEM.

The present chapter investigates polymer deformation during hot embossing manufacturing on the 1-100 μm scale, which are standard feature sizes for MEMS [15, 21]. The polymer films studied are of thickness greater than the master feature height. To study the onset deformation, embossing experiments are made for temperatures from 10 ºC below T_g to 20 ºC above the polymer T_g and for times less than the cavity filling time. Cavity filling is studied for three different embossing tool geometries with height 4 μm and width 30, 50, and 100 μm. Imprint force, temperature, time under maximum load, and total time of embossing are varied and correlated with replicate polymer feature dimensions. Atomic force microscopy (AFM) measures and scanning electron microscopy (SEM) inspects the shape of the master and deformed polymer. Linear regression analysis confirms the trends suggested by measurements.

2.2 Experimental Methods

A standard microfabrication process produced multiple embossing masters on 100 mm diameter silicon wafers. A thermal oxide of 100 nm was grown for an improved etch mask. Photolithography patterned the wafer, and a buffered oxide etch opened holes in the oxide, exposing the silicon. A deep reactive ion etch (Bosch Process) with an etch rate of roughly 0.3 μm per cycle for 12 cycles etched the oxide patterned wafer, and then a Piranha chemical wet etch removed the residual photoresist. Fabrication resulted in 500 μm square fields of 4 μm wide ridges with periodicity 30, 50, and 100 μm. Feature heights ranged from 3.5 to 4.0 μm. Figure 1 shows SEM micrographs of the silicon masters.

A standard photoresist was chosen as the polymer to be embossed. The polymer sample used was a PMMA-like novalac-based resin photoresist (AZ4620-Clariant) with a reported T_g of 91 °C and a boiling temperature of 134 ºC [24]. The polymer samples were prepared in the following manner. Silicon wafers were dehydration baked for 15 minutes at 120 ºC prior to polymer application. The polymer was spin-cast for 20 seconds at 2000 rpm and then hard baked for 10 minutes at 90 ºC resulting in approximately 15 μm layer thickness.

The embossing was performed with a controlled-heating, force-sensing system housed on a one-ton arbor press. The embossing system provides load response control in less than .75 sec, embossing temperature range from room temperature up to 300 ºC, and force application up to 4400 N with an accuracy of 1 N over a circular area of diameter 50 mm. The sample was loaded into the embossing press face up on top of a heating source and the silicon master was placed feature side down atop the polymer

sample. The sample and master were allowed ~60 sec to come to the embossing temperature, then the load was applied over a specified ramp rate, held, then released. The master and sample were separated after cooling to room temperature. Figure 2-1 shows SEM micrographs of embossed polymer. Load, load rate, temperature, and total loading time were recorded for loading forces of 30-40 MPa for loading times of 1 to 25 seconds. Total embossing times ranged from 30 to 65 seconds with embossing temperatures of 80 ºC, 90 ºC, 100 ºC, and 110 ºC.

Atomic force microscopy with high aspect ratio probe tips (STING-MicroMasch) enabled continuous scan over the entire topography of the silicon master ridges and imprinted polymer trenches. Scanning electron microscopy inspected polymer cross-sections to ensure accurate mapping of trench floors. Figure 2-2b shows a typical profile scan of a 100 μm imprinted area. Several characteristic features were seen in all of the replicate polymer samples. Peak height is defined from imprinted floor to peak and is averaged when two peaks occur in one field. Peak-to-peak width is the distance between two polymer peaks present in one field. Peak-to-trench depth is the distance between the average height of the two polymer peaks and the minimum height of the depression between peaks. Area filled is the Simpson's Rule approximation of the area underneath the polymer profile. One measurement not shown in Figure 2-2 is the flat length, defined when conformal filling has begun. The flat length is the horizontal length of one peak of polymer that has begun to flatten and conformally map the master floor.

2.3 Results and Discussion

By varying embossing time, temperature, and master cavity width, various stages of the initial deformation of polymer during HEM were observed. A dual-peak deformation response dominated by viscous flow and probable shear-thinning behavior occurred for cavities of 4 μm height and 50 and 100 μm width. Single-peak deformation was observed in 30 μm wide cavities. The observed deformation ties together and bridges the gap in previous studies of HEM polymer deformation limited by mass transport.

The Williams-Landel-Ferry equation [25] gives an exponential temperature dependence of viscosity,

$$log\ \alpha_T\ =\ log\ \frac{\eta(T)}{\eta(T_s)} = \frac{-C_1(T-T_s)}{(C_2+T-T_s)} \tag{2.1}$$

where α_T is the time shift parameter, η is the viscosity, T is the temperature, the subscript s denotes the reference value, and C_1 and C_2 are constants. The time- and temperature-dependent viscosity translates to a temperature-time equivalence in experimental parameters. A decrease in embossing temperature towards and even below the glass transition temperature slows the polymer deformation to enable investigation of the initial stages of polymer flow during HEM. Different cavity widths on the same master essentially allow snapshots of polymer flow at different times with a time-distance-temperature equivalence for progression of polymer flow during embossing. Combining low embossing temperatures, different cavity widths, and short embossing times with thick polymer films enables a view of polymer flow during initial stages of deformation where polymer flow is not supply-limited. Rather than a compressed central region between two polymer peaks that climb the master sidewall as observed for thin films, the

deformation observed is of two smoothly sloping polymer peaks forming adjacent to the master sidewalls and flowing upward and away from the master sidewalls.

The dual polymer peaks deforming outward from the master sidewall can be seen in Figure 2-3, which displays AFM line scans of polymer filling of a micro-cavity with widths 30, 50, and 100 μm embossed at T_g – 10 °C. Polymer deforms into the 100 μm

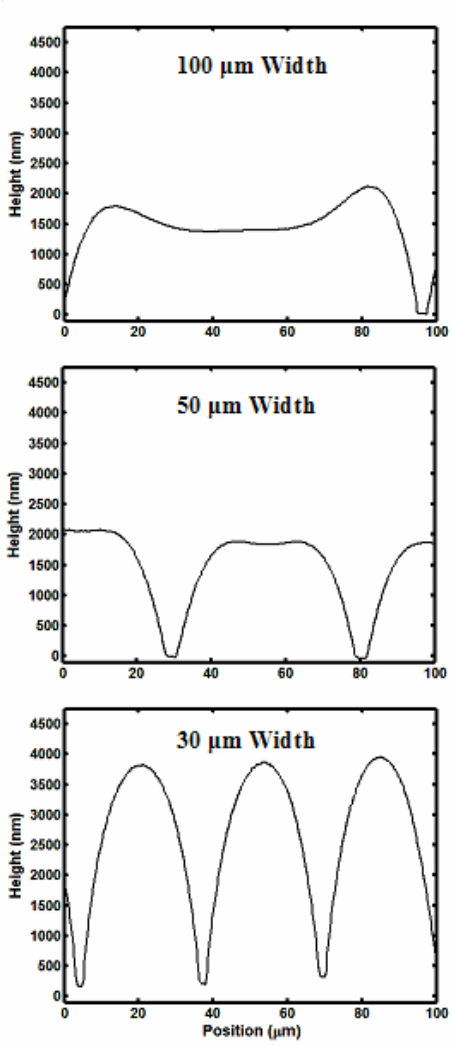

Figure 2-3 AFM line scans of polymer filling cavities of different widths embossed at T_g - 10 °C under a maximum load of 30 MPa for 45 sec for 65 sec total embossing time. The different widths freeze the polymer peaks at various stages of the embossing process, showing motion of peaks toward the cavity center.

wide cavity with two well-defined peaks of polymer at the edge of the cavity walls. Two peaks of polymer are still visible in the 50 μm wide cavity though the distance between the peaks is greatly diminished as the vertical deformation has increased. In the 30 μm wide cavity, only a single, tall peak of polymer is present. Scans of different cavity widths at the same embossing parameters show the polymer peaks forming adjacent to the master sidewall and moving upwards and toward the center of the enclosed region.

Figure 2-4 further illustrates this mode of deformation where polymer peaks deform vertically and laterally toward the cavity center for polymer deformation in a 50 μm wide cavity at different temperatures. Lower temperatures correspond to a highly viscous polymer and thus an early stage of deformation. At the highest viscosity at an embossing temperature of T_g – 10 °C, polymer flow is largely restricted, and two separate peaks are present. Longer loading times at the same temperature increase the overall height of the deformation while the peaks slowly move closer together. Conditions more favorable to polymer flow, i.e. increasing the embossing temperature to the T_g of the polymer, result in two polymer peaks merging into one peak at the cavity centerline. At even higher mobility, the single polymer peak reaches the master floor and spreads laterally as it flattens to conform to the master. A 30 μm wide cavity embossed at T_g + 10 °C, representing flow conditions of high mobility in a narrow field, are shown in Figure 2-5. A single, central deformation flattens and spreads laterally when conforming to the master.

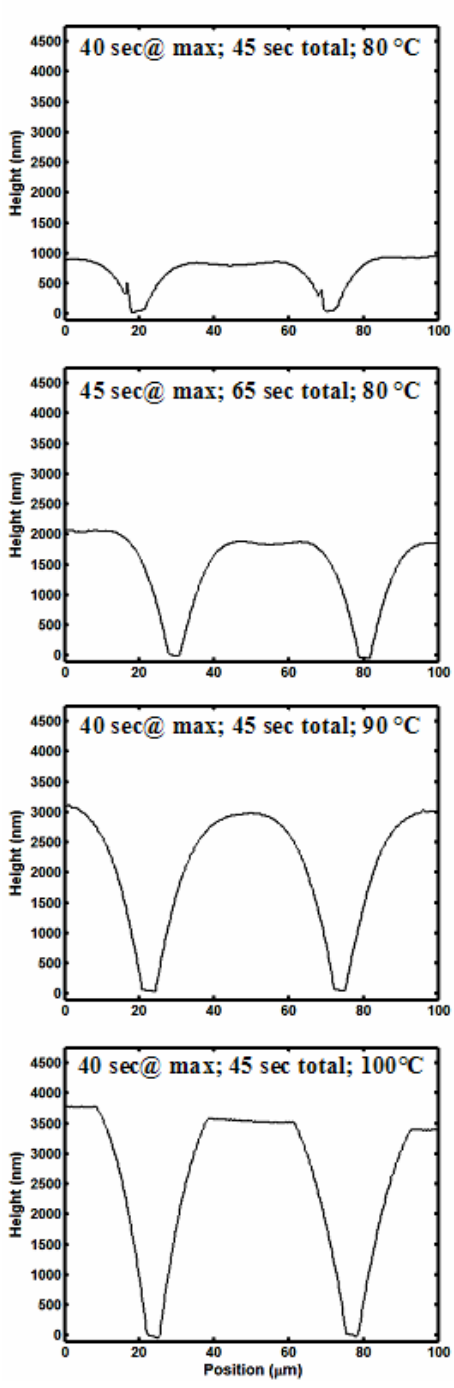

Figure 2-4 AFM line scans of 50 µm wide polymer cavities representing different stages of deformation during embossing under a maximum load of 30 MPa. Line scans depict decreasing polymer viscosity from top scan to bottom scan. As the embossing progresses, the polymer peaks coalesce into one peak deforming upward and eventually reaching the master floor.

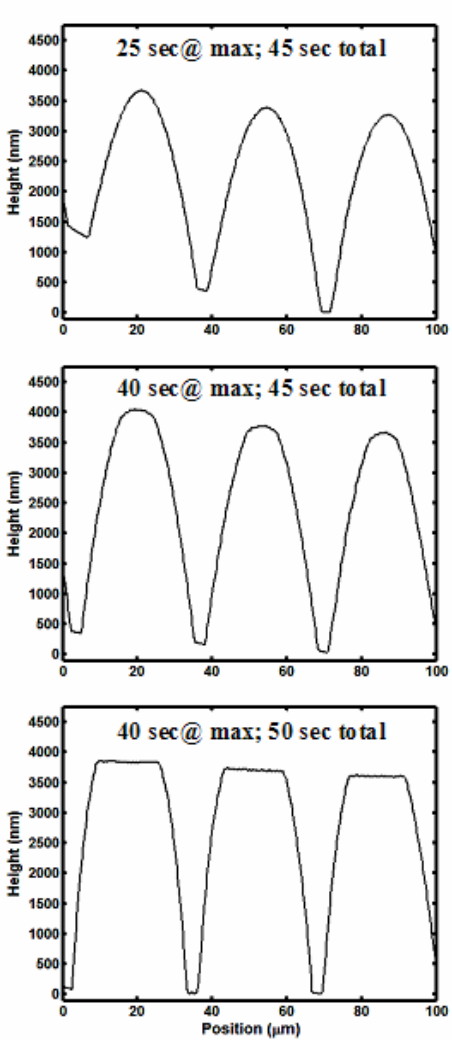

Figure 2-5 AFM line scans of 30 μm wide polymer cavities embossed at T_g + 10 °C under a maximum load of 30 MPa. The dual polymer peaks either did not form or have already coalesced at the first time shown. The single peak deforms vertically until reaching the master floor. Lateral spreading and flattening of polymer peak then ensues.

The measured peak height, percent area filled, and peak-to-peak width, shown in Figure 2-6 and Figure 2-7, further illustrates polymer deformation where dual polymer peaks deform vertically and then laterally toward the cavity center. The overall height of the peaks increases with temperature and time, shown in Figure 2-6. The area filled shows a consistent increase with temperature and time. The trend is supported by strong

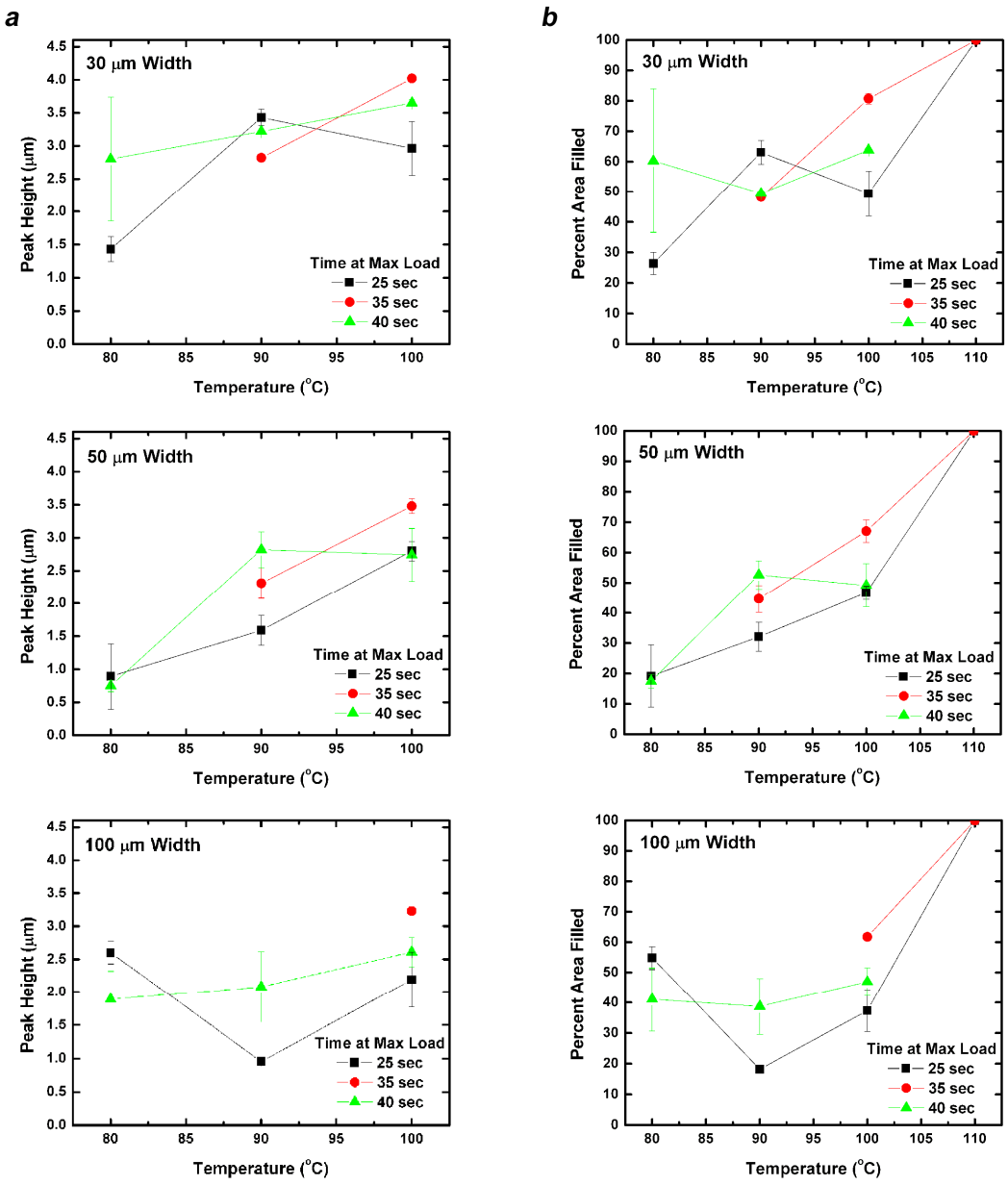

Figure 2-6 (a) Polymer peak height vs. temperature and (b) percent area filled for 3 different times under a maximum load of 30 MPa held for 45 sec total. Peak height and filled area increase with increasing temperature and time, showing deformation by vertical deformation of polymer peaks.

statistical relevance, with an overall regression F-statistic well under 1% and P-values on the individual temperature and time variables well under 10%. The area filled reaches 100% filling for embossing times as small as 30 sec at embossing temperatures of T_g + 20 °C. As shown in Figure 2-7, the peak-to-peak width decreases drastically at embossing

temperatures above T_g, indicating lateral flow. The dual peak deformation was observed in 100 μm and 50 μm wide cavities for all embossing temperatures, but at higher embossing temperatures, the dual peaks in the 50 μm wide cavities were only observed under short imprint times. The appearance of the dual peaks in the 50 μm wide cavities at embossing temperatures above T_g suggests this dual-peak polymer flow is not merely an artifact of compressive deformation at embossing temperatures below T_g. The dual peaks were not observed in the 30 μm wide cavities at any time or temperature as the peaks either did not form due to the small cavity width creating a uniform viscous flow field or they merged quickly over the short lateral distance. In the 100 μm wide cavities, conformal filling was achieved at embossing temperatures of T_g + 20 °C, with dual peaks that independently flatten and spread laterally to fill the available geometry.

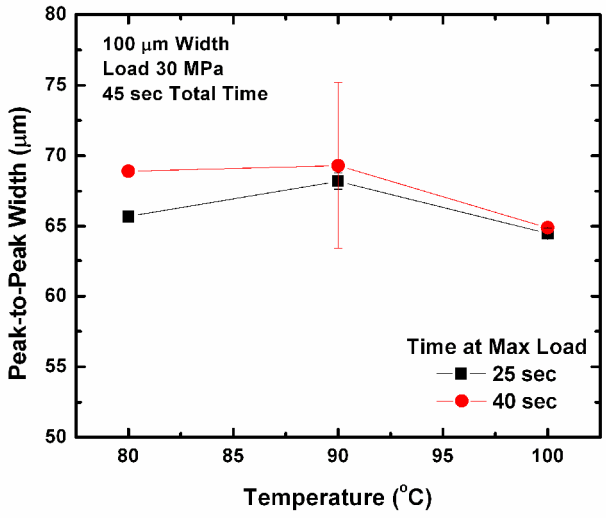

Figure 2-7 Peak-to-peak width of 100 μm wide polymer cavities embossed at 30 MPa for a total of 45 sec held at maximum load for different times. The peak-to-peak width decreases dramatically for temperatures above T_g, suggesting that polymer peaks deform laterally toward the cavity center as embossing progresses.

These observations of polymer flow during HEM suggest a mode of deformation where polymer adjacent to the master sidewall has enhanced flow properties and deforms in separate peaks upward and adjacent to the master sidewall. The dual peaks that appear in early stages of deformation appear to have a width independent of cavity size, possibly due to local stress concentrations near the cavity wall. Applying Saint-Venant's principle [26], with a minimum master sidewall width of 4 μm, a region of locally high stress would appear over a distance of approximately 1 to 2 times the sidewall width, or extend 8 μm into the cavity before the stress distributes over a constant area. The high stress region results in high strain localized near the master sidewall. Such an effect would be more pronounced in a shear-thinning material. If the cavity size, thickness of polymer film, and embossing parameters permit, these dual peaks will occur at early stages of deformation before spreading laterally and eventually merging into one peak. Such a mode of deformation supports claims [17, 18, 20, 23] of possible shear-thinning and viscous-heating phenomena on this length scale that would enhance polymer mobility adjacent to master features compared to material in central regions of the mold. The characteristic dual-peak deformation is similar to the simulations predicted by Jeong for deformation into a cavity of width 1 μm and height 500 nm with zero surface tension. With larger loading pressures and cavity dimensions, the effect of surface tension would be minimal [21, 27], thus the simulation results are consistent with the mode of deformation observed here. The single peak deformation of the 30 μm wide cavity also corresponds with Jeong's simulations of zero surface tension into a 100 nm cavity width, suggesting a characteristic cavity width and film thickness for uniform viscous flow. The dual-peak deformation observed here also is consistent with Cross' observed double peak

flow for thicker films (1.7 μm films for 2 μm cavity height) under high loads and high load rates, conditions which restrict polymer flow within the cavity. In describing the flow of a single deforming polymer peak at the cavity center, Cross sees stagnation flow at a centerline in cavity filling of thicker films forcing incoming polymer to deform as a single peak upwards at the center. At lower embossing temperatures such as those used here, however, a region of quasi-stagnation flow occurs closer to the master sidewall thus giving rise to dual peaks of deforming polymer. Polymer mobility enhancement near the cavity sidewalls due to stress concentration and/or shear-thinning produces a large difference in viscosity of polymer near the master sidewall relative to material in central regions of mold. This effect is more noticeable at lower temperatures where the viscosity of polymer in central regions strongly resists deformation. Unlike previous studies, the present experiments suggest lateral motion and merging of polymer peaks before the onset of conformal filling.

The measured flow characteristics can aid in microembossing process design. The measurement of percent area filled and imprint time can be used with loading data to calculate a hot embossing manufacturing effective viscosity, defined here as

$$\upsilon^* = \frac{P}{(A_{fill} / \tau)} \tag{2.2}$$

where P is the embossing pressure, A_{fill} is the percent area filled, and τ is the embossing time. Figure 2-8 shows calculated effective HEM viscosity for a temperature range of 10 °C below T_g to 20 °C above T_g. Approximating the viscosity as a measure of dynamic

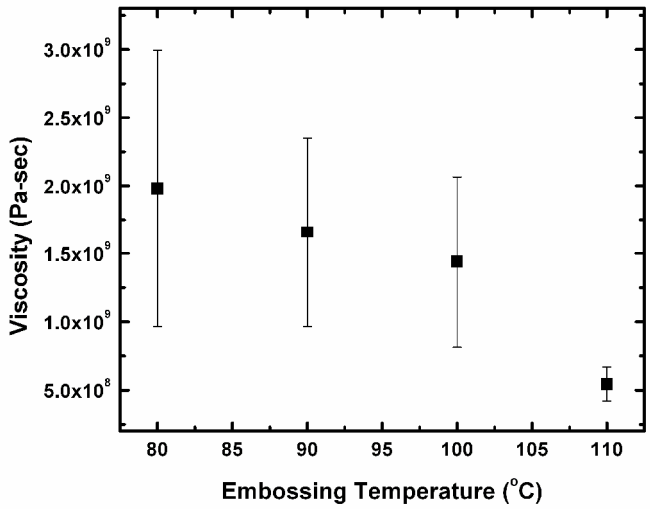

Figure 2-8 Temperature dependence of hot embossing micro-manufacturing viscosity, defined as load per percent area filled per second. The large drop in viscosity between 100 °C and 110 °C suggests a glass transition temperature in this range, higher than reported for the polymer. The possible rise in T_g could be due to extensive cross-linking during the hard bake. The HEM viscosity could be used as a manufacturing guideline in determining embossing parameters required for conformal filling of master geometries.

viscosity with frequency 1/(2π*embossing time) results in an estimate that is within an order of magnitude of that observed by Juang [20] in dynamic mode for frequency of .001 rad/sec. The measured HEM viscosity is several orders of magnitude lower than the general expected Newtonian viscosity value of 10^{12} Pa*sec for most polymers at T_g [28]. The drop in HEM viscosity in Figure 2-8 between 100 °C and 110 °C could be artificially low as conformal filling occurred in this range. This model of HEM viscosity could be used for process design to predict filling for cavity sizes, times, and temperatures not explicitly measured here.

2.4 Conclusion

This chapter measures polymer deformation during microcavity filling for the purpose of understanding and improving hot embossing manufacturing of MEMS. With

polymer films of sufficient thickness such that polymer supply is not limited, the filling of micron-sized cavities was found to occur by two separate polymer peaks that deform vertically and laterally toward the cavity center. Viscous flow, local stress, and shear-thinning phenomena dominate over surface tension effects during polymer deformation. This flow behavior is applicable to embossing of thermoplastics at high temperatures and short times and for embossing of materials at temperatures near T_g. Measured filling effectiveness allows calculation of an effective polymer viscosity, which can aid in process design. Better understanding of polymer flow characteristics for different polymers, film thickness, and cavity widths should aid the manufacture of all-polymer MEMS.

CHAPTER 3

IMPACT OF POLYMER FILM THICKNESS AND CAVITY SIZE ON POLYMER FLOW DURING EMBOSSING: TOWARDS PROCESS DESIGN RULES FOR NANOIMPRINT LITHOGRAPHY

This chapter presents continuum simulations of polymer flow during nanoimprint lithography (NIL). The simulations capture the underlying physics of polymer flow from the nanometer to millimeter length scale and examine geometry and thermophysical process quantities affecting cavity filling. Variations in embossing tool geometry and polymer film thickness during viscous flow distinguish different flow driving mechanisms. Three parameters can predict polymer deformation mode: cavity geometry and polymer thickness ratios, polymer availability, and Capillary number. The ratio of cavity width to initial polymer film thickness determines vertically- or laterally-dominant deformation. The ratio of indenter width to residual film thickness measures polymer availability which determines Stokes or squeeze flow. Characteristic NIL Capillary number based on Stokes, squeeze, or single peak pipe flow fill time distinguishes between capillary or viscous driven flows. The three parameters predict filling modes observed in published studies of NIL deformation over nanometer to millimeter length scales. The work seeks to establish process design rules for NIL and to provide tools for the rational design of NIL master templates, resist polymers, and process parameters.

3.1 Introduction

In nanoimprint lithography (NIL), a nanofabricated master tool having three-dimensional topography embosses a thermoplastic substrate, forming a negative relief of the master in the substrate. NIL offers scalable manufacture of nanoelectronics and nanoelectromechanical systems (NEMS) with resolution better than 10 nm [1] over areas greater than 100 mm^2 [2]. Recent studies have improved NIL resolution below 5 nm [3] and to the molecular scale [4]. A deep understanding of polymer flow during NIL is critical for rational design of embossing tools and processes. This paper investigates viscous polymer flow during NIL for a wide range of master tool geometry and establishes a framework for NIL process design based on geometric ratios, polymer thickness, and Capillary number.

Several groups have investigated polymer flow during imprint lithography with different embossing geometries and length scales, resulting in several competing phenomenological models of polymer flow [17, 20, 22, 29-32]. Experiments and simulations conducted from the millimeter to nanometer scale resulted in markedly different polymer deformation modes although length scale has not been the apparent cause of differentiation. Figure 3-1, showing single and dual peak viscous flow, illustrates two polymer deformation modes reported in NIL. Differences in deformation mode and replication fidelity have been attributed to a variety of factors, notably shear and extensional stretching, viscous flow and localized stress, residual stress release, shear-thinning and buckling, and surface tension.

Studies of embossing on the millimeter to micrometer scale have consistently cited the impact of shear deformation on replication while also noting other case-specific

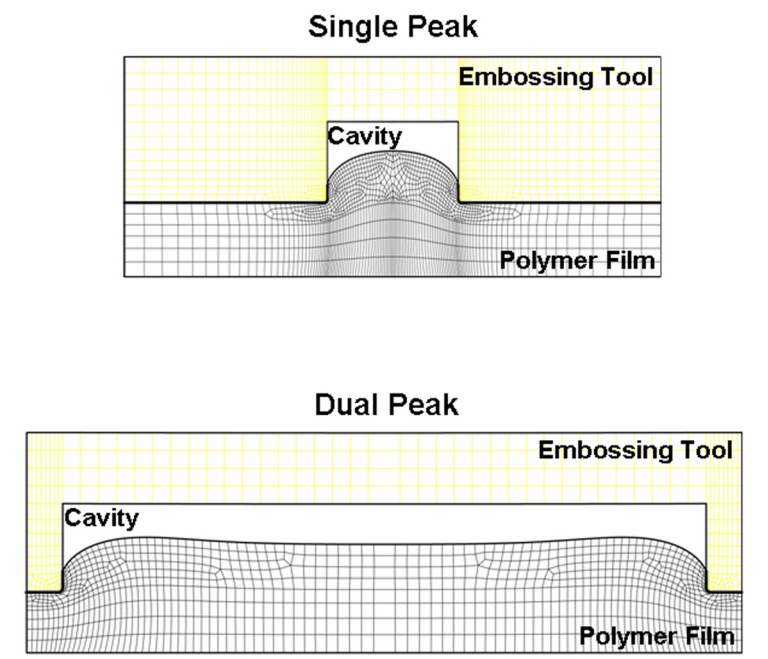

Figure 3-1 Nanoimprint lithography polymer deformation modes, exhibiting either single or dual peak deformation.

effects. Simulations and experiments at the millimeter scale [20] used a cavity of height 800 μm, width 3.5 mm, and spacing 3 mm to emboss a viscous PMMA film of thickness 1200 μm at 40 °C above its glass transition temperature (T_g). This system resulted in polymer flow with shear deformation at the mold surface and extensional stretching at the cavity center. Experiments at the micrometer scale [29] studied microembossing with indenter width 2 μm, cavity height 4 μm, and cavity widths 30 μm, 50 μm, and 100 μm and 15 – 20 μm thick PMMA films over a temperature range from T_g - 10 °C to T_g + 20 °C. A region of localized high strain occurred near the cavity sidewall, resulting in a deforming polymer peak that spread laterally and vertically to fill the cavity. The microembossing conditions resulted in viscous flow, localized stress, and shear-thinning phenomena dominant over surface tension effects. Indentation experiments at the micrometer to nanometer scale [30] pressed cylindrical micrometer sized cavities of

height 2 μm and diameter 10 μm into glassy polymer films of thickness 450 nm and 1.7 μm. In the 450 nm film, the sharp cavity entrance produced extensive shear resulting in dual polymer peak filling. Indentation into the thicker films resulted in dual peak deformation for high loads and single peak deformation for low loads. Residual stress release on demolding influenced final replicated feature size, a phenomenon also noted in [33].

A few NIL studies investigated polymer deformation for film thicknesses and cavity heights in the 100 – 300 nm range. A large area flow experiment [17] studied cavity filling of 200 nm thick PMMA films embossed at T_g + 100 °C by cavities of width 20 μm, height 175 nm, and spacing 40 μm. The resulting deformation was a flat dual peak profile with vertical sidewalls and a central buckled region, attributed to effects from squeeze flow and shear-thinning at the indenter edge and compressive stresses in the interior of the cavity. This experimental work was followed by finite element simulations of a Newtonian fluid with surface tension [22]. These simulations showed the buckling region was the result of capillary forces acting over the large cavity width, where the polymer preferentially wetted the master surface. When surface tension effects were removed from the simulations, smooth single or dual peaks were observed dependent on cavity width, as observed in viscous flow experiments [29]. Other simulations and experiments [31, 32] investigated purely nanometer scale geometries and film thicknesses. Elastic solid simulations modeled the polymer with the nonlinear stress-strain behavior of a Moony-Rivlin material. The studies showed both single and dual peak flow confined near the master sidewall as described above [29, 30], and noted the effect of film thickness to retard deformation. The authors concluded that polymer in

NIL shows rubber-like elastic dynamics above T_g with volume compression under high loads in thick polymer films, suggesting that the elastic component of polymers plays a large role in deformation even at temperatures well above T_g.

Simulations and experiments investigating embossing and imprint lithography from the millimeter to nanometer scale have yielded the common features of single or dual peak deformation that depends on a thermophysical property or process quantity. Several reported causes have been attributed to producing single or dual peak deformation. Each of the above-referenced studies offers a different phenomenological explanation of the observed behavior and there is little agreement about the relative importance of nonlinear elasticity, residual stress, linear and nonlinear viscous flow, compressive stresses, and capillary forces. There is a need for detailed and systematic study of geometric and material constraints over the length scales of interest to isolate factors causing the common features of single or dual peak deformation. The lack of a comprehensive understanding of polymer flow in the 10 nm – 100 μm range limits NIL process design to ad-hoc or recipe-based approaches.

This chapter presents simulations of liquid polymer deformation and filling modes during NIL under viscous-dominant conditions. Independent variation of imprint pressure, polymer viscosity, polymer film thickness, indenter width, and cavity width and height allows examination of parameters influencing cavity filling time and polymer deformation mode. A simple model of laminar flow between plates, Stokes flow, and squeeze flow characterizes the polymer filling time. The simulation regime is completely non-dimensionalized and the results are easily extrapolated for comparison to experiments investigating polymer flow in the 10 nm – 5 mm range. The simulation

results predict behavior seen during all previously published NIL deformation studies. We suggest that three characteristic parameters, specifically, geometry ratios, polymer availability, and Capillary number, could form the nucleus of NIL process design rules.

3.2 Simulation Overview

Prior simulations of NIL have treated the polymer as either a viscous Newtonian fluid [22] or nonlinear elastic solid material [31, 32]. Solid mechanics simulations with a Moony-Rivlin constitutive model [31, 32] used the commercially-available MARC program, based on the finite element method and rectangular plane strain elements, to model the polymer as a rubber elastic above T_g. Fluid mechanics simulations [22] used the commercial computational fluid dynamics code CFD-ACE, based on the finite volume method, to simulate NIL on an Eulerian grid using the volume of fluid method (VOF) to track the deforming polymer interface. VOF methods have also been used to model micro injection molding [34, 35], but the methods sacrifice boundary shape accuracy for a faster speed of solution [36]. The free boundary or moving boundary simulations presented in this paper are ideally suited for *GOMA* [37], a Galerkin finite element program specialized for analysis of manufacturing flows having one or more transport fields such as those that exist in two-phase flows or for the freely-moving polymer surface of NIL.

GOMA allows the liquid polymer and the solid indenter to be treated in an arbitrary Langrangian/Eulerian (ALE) reference frame, thereby separating the polymer and solid motion from the mesh motion thus allowing for large free boundary deformations [36, 38]. All surfaces move as part of a fully-implicit, fully-coupled

algorithm [36] that links the mesh motion to the material motion through surface kinematic conditions. A Newton-based solution algorithm enables the mesh motion and the rest of the problem physics to be solved simultaneously. For the simulations presented here, an implicit Backward-Euler time integration is used with a classical Gaussian elimination LU decomposition method. The maximum dimensionless time step size is 0.01 with a residual less than 10^{-7} at each time step. The mesh uses 9-node isoparametric quadrilaterals with smaller elements near the indenter-polymer interface and larger elements at the cavity center for accurate and swift solution convergence.

Figure 3-2 shows the finite element model with prescribed distinguishing conditions. The solid indenter is initially embedded in a thin layer of polymer to aid convergence at simulation start up. The model assumes the embossing geometry is

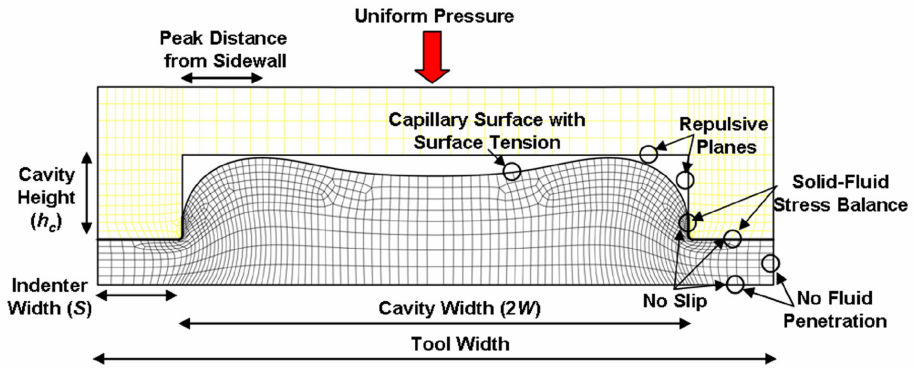

Figure 3-2 Nanoimprint lithography cavity and deforming polymer, showing simulation boundary conditions, geometry variables, and polymer peak deformation location measurement.

adequately vented or under vacuum conditions. To improve computation time and convergence, the problem is non-dimensionalized by choosing a characteristic length X_o equivalent to the tool width, pressure P_o equivalent to the applied load, time T_o equivalent to the ratio of polymer viscosity η to applied load, and speed U_o equivalent to the ratio of characteristic length to characteristic time. This form of characteristic time matches the

timescale of microembossing experiments previously reported [29] and assures non-dimensionality of the governing equations when used in conjunction with the form of characteristic speed listed above. The scaled conservation equation for mass is

$$\nabla^* \cdot v^* = 0\,, \tag{3.1}$$

and the scaled liquid momentum conservation equation is

$$Re\left(\frac{\partial v^*}{\partial t^*} + (v^* - vm^*)\cdot\nabla^* v^*\right) = \nabla^* \cdot \Gamma^*\,, \tag{3.2}$$

where Re is the Reynolds number, v^* and $v_m{}^*$ are the material and mesh dimensionless velocity, respectively, t^* is the dimensionless time, and Γ^* is the dimensionless liquid stress tensor. The dimensionless Reynolds number is $\rho U_o X_o/\eta$, or equivalently $\rho P_o X_o{}^2/\eta^2$, where ρ is the density. The right hand side of Eq. 3.2 is the divergence of the liquid stress tensor.

The boundary condition on the free surface of the liquid is modeled by a force balance of the liquid normal stress tensor with capillary forces:

$$\hat{n}\cdot\Gamma^* = \frac{1}{Ca}H^*\hat{n} + \frac{1}{X_o{}^4}\frac{P_{rep}{}^*}{d^{*4}}\,, \tag{3.3}$$

where $\hat{n}$ is the normal vector, Ca is the Capillary number, H^* is the dimensionless curvature, $P_{rep}{}^*$ is an arbitrary dimensionless repulsive force, and d^* is the dimensionless distance of the polymer boundary normal to the solid indenter. The Capillary number $Ca=\eta U_o/\sigma$, or equivalently $P_o X_o/\sigma$, is a ratio of viscous forces to surface tension forces, where σ is the surface tension. Equation 3.3 represents a force balance at the polymer-air interface that balances the surface tension force due to curvature of the surface, the normal stress from the liquid, and the contact force due to the proximity of the solid

surface. The contact force P_{rep}^{*} is not significant physically and is arbitrarily chosen to ensure no liquid penetration of the solid surface. The repulsive term is applied to the liquid surface normal to the contact plane, allowing the liquid to slip along the solid surface without penetrating the solid. The ALE framework allows the capillary boundary condition to define the material shape of the free surface and a kinematic mass balance ensures that the mesh location conforms to the material location at the boundary:

$$\hat{n} \cdot (v^{*} - v_{m}^{*}) = 0 , \tag{3.4}$$

The body of the liquid can still be represented by an immaterial mesh that does not introduce artificially high stresses on deformation while the capillary surface can determine the motion of the moving boundary. A no-slip condition is applied to the liquid at the initial liquid-solid interface with the indenter and substrate.

While the stress and strain in the solid master is important for NIL process design, the liquid deformation is of primary interest here so the simulations use a single solid cavity of small mass. Conservation of momentum transfers load from the solid to the liquid. Assuming elastic forces are much larger than inertial forces, solid momentum conservation is

$$\frac{1}{X_o} \nabla^{*} \cdot \Gamma_{s}^{*} + P_o P^{*} = 0 , \tag{3.5}$$

where Γ_{s}^{*} is the dimensionless elastic stress tensor and P^{*} is the dimensionless body force of the embossing load. The elastic stress tensor is

$$\Gamma_s = 2\mu E^{*} + \lambda e^{*} I , \tag{3.6}$$

where μ and λ are the Lame elastic coefficients, E^{*} is the dimensionless small deformation strain tensor, and e^{*} is the dimensionless small deformation volume strain.

At the liquid-solid indenter interface, a stress balance is prescribed where the stresses in the liquid directly replace the stresses in the solid material residual equation at the interface. The balance in equation form is

$$\frac{P_o}{\mu}\hat{n}\cdot\Gamma^* = \hat{n}\cdot\Gamma_s^*, \tag{3.7}$$

GOMA is capable of modeling a variety of liquid constitutive equations. Both Newtonian liquid models and non-Newtonian Carreau-Yasuda models are used, where the Carreau-Yasuda model is given in unscaled form by

$$\eta = \eta_{\inf} + (\eta_o - \eta_{\inf})\left[1+(\lambda_p\dot{\gamma})^a\right]^{\frac{(n-1)}{a}}, \tag{3.8}$$

where η_{inf} and η_o are the infinite shear limit and zero shear limit viscosity, respectively, λ_p is the polymer time constant, $\dot{\gamma}$ is the second invariant of the shear rate tensor, n is the shear thinning exponent, and a is a dimensionless parameter describing the transition between the low-rate and power-law region. For the Carreau-Yasuda model, *GOMA* assigns the value of viscosity for each meshed element based on local shear rate. With proper constants, the model fits well the material properties of a representative imprint polymer described by Fuchs *et al* [39]. A Newtonian viscosity model using the effective embossing viscosity measured near T_g in [29] correlates well to experiment, hence a simple Newtonian material model rather than a computation-intensive Carreau-Yasuda model is used for the majority of simulations to optimize processing time.

Nine independent parameters compose the simulation space: applied pressure P_o; polymer viscosity η; polymer density ρ; surface tension σ; initial film thickness h_i; ramp time t_r where t_r is the time required to linearly ramp the applied pressure from zero to P_o; indenter width or cavity spacing S; tool width $X_o = 2S+2W$ where W is the cavity half

width; and cavity height h_c. To address the largest possible solution space, nondimensionalization reduces the number of simulation variables to a Reynold's number equivalent to $\rho P_o X_o^2/\eta^2$, Capillary number equivalent to $P_o X_o/\sigma$, and several geometric quantities. For a given tool width, applied pressure, and polymer viscosity, the indenter width, film thickness, and cavity height are systematically varied to determine their effects on polymer deformation mode and dimensionless time to fill. Since density and surface tension variation among polymers are not as significant as changes in processing parameters of pressure and viscosity, density and surface tension are constant for all cases. Ramp time is not thoroughly investigated for effects on shear rate, hence the dimensionless ramp time is constant for all cases. As tool width, applied pressure, and polymer viscosity are varied, different forms of geometric ratios are investigated to distinguish significant geometric quantities influencing polymer deformation mode and dimensionless time to fill.

3.3 Results

Simulations investigated polymer deformation during cavity filling for viscous-dominant conditions, i.e. $Re << 1$ and $Ca >> 1$, where the time scale of relaxation is less than the time scale of flow. Figure 3-2 shows a representative rectangular cavity having indenter width S, cavity height h_c, and cavity half width W. Of particular interest is the location and size of the polymer peak(s), and the time required to fill the cavity. Under viscous-dominant conditions, insignificant change in polymer deformation profile and dimensionless fill time was observed for changes in Reynolds number due to variations of applied pressure and viscosity over several orders of magnitude. Thus simulations

modulated cavity geometry and polymer film thickness to examine their effect on polymer deformation mode. Most simulations modeled the polymer as a Newtonian fluid, but a few modeled the polymer as shear-thinning. Cylindrical cavities were briefly investigated as well.

3.3.1 Polymer Deformation Mode

Figure 3-3 shows the effect of rectangular cavity width and film thickness on polymer deformation, where dimensionless cavity size is the ratio of cavity width to tool width $W/(S+W)$ and dimensionless cavity height is the ratio of cavity height to film thickness h_c/h_i. The indenter width is constant and only the cavity width or polymer film thickness changes. For each configuration, deformation profiles are shown for four times: the start of imprinting t_i, half the time to onset of filling t_h, onset of filling t_o, and the time when polymer has covered half of the master cavity floor t_f. Onset of filling occurs when the polymer peak first touches the master cavity floor. The actual value of time at t_h, t_o, and t_f varies for different geometries. As cavity width increases, the deformation mode changes from single peak to dual peak deformation. The polymer deformation also transitions from single to dual peak as the initial polymer film thickness decreases, as shown in Figure 3-3b. For the largest cavity widths and thinnest polymer layers, the two peaks are highly localized near the vertical cavity walls and do not interact.

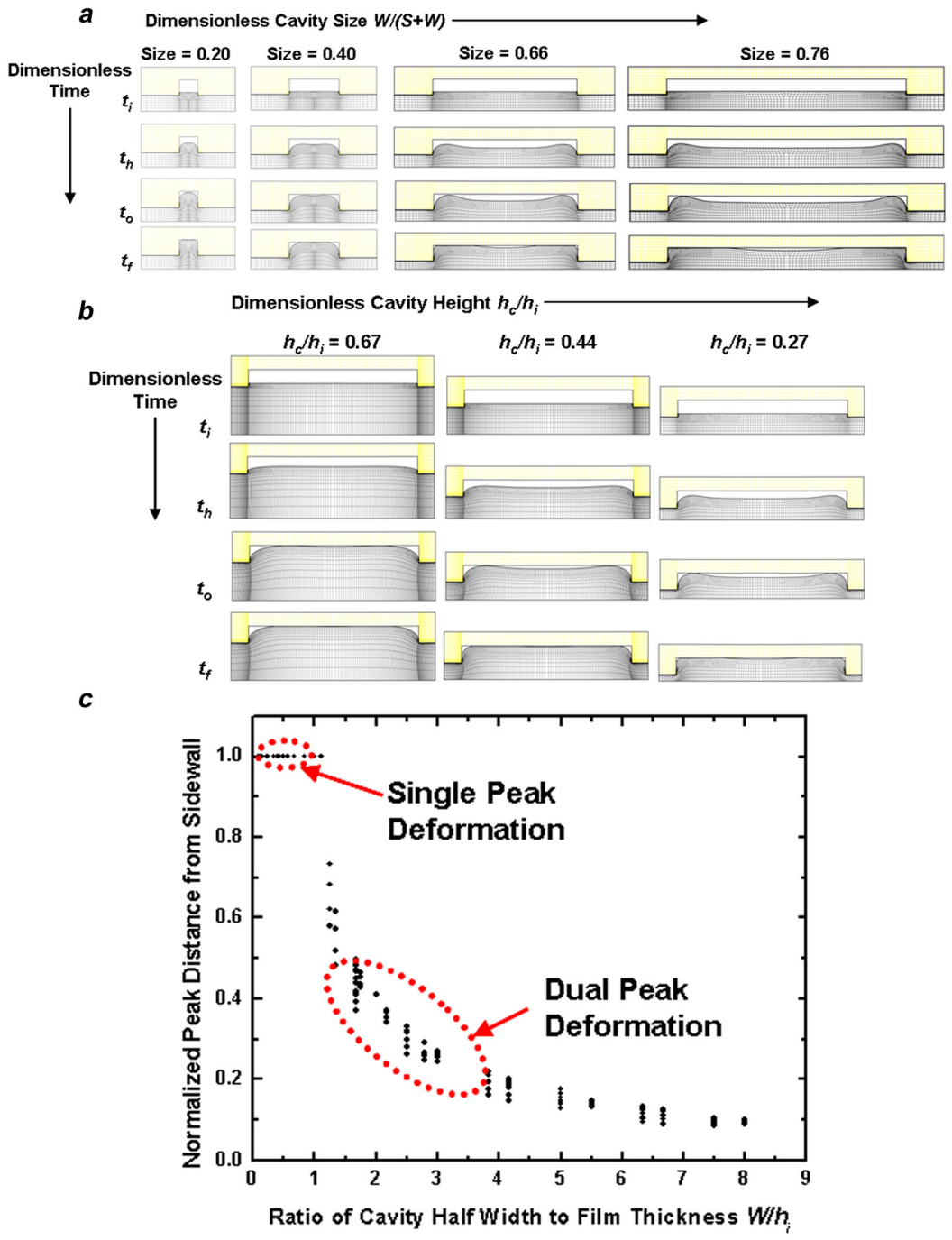

Figure 3-3 Deformation profiles for (a) increasing cavity width holding indenter width and film thickness constant and (b) decreasing film thickness holding cavity geometry constant. The nondimensional time captures both load force and polymer viscosity, through time-temperature superposition. (c) Impact of resist film thickness on cavity filling. The polymer peak distance from the sidewall is normalized by the cavity width. The location of the deforming polymer peak location is always a distance from the cavity vertical sidewall approximately equal to the polymer thickness.

For all of the simulations of this paper, the polymer deformation occurs near the indenter sidewall. Confirming the importance of cavity half width W and initial film thickness h_i in determining single or dual peak flow suggested by Figure 3-3a and Figure 3-33b, Figure 3-3c shows the transition from single to dual peak flow based on W and h_i. By normalizing the distance of the apex of the polymer peak from the sidewall at the onset of filling by cavity width, the single to dual peak transition can be clearly observed at W/h_i near 1.2. The polymer peak remains located roughly h_i from the indenter sidewall regardless of any other parameter. Small variations in peak location for a given value of W/h_i are due to polymer shear limits or complete cavity filling. High shear along the indenter sidewall reduces the peak distance from sidewall, causing slightly smaller peak distance from sidewall for smaller indenter widths than larger indenter widths. The polymer peak also spreads laterally slightly more for larger cavity heights than smaller cavity heights but the lateral motion of the peak is essentially constrained, driven by shear near the indenter.

The degree of fluid shear-thinning behavior experienced by different materials influences peak location, shown in Figure 3-4. Deformation profiles are shown after a simulation time of 1.0 for a Newtonian fluid and shear-thinning fluids of varying degree of power law exponent, where η_{inf} and η_o differ by four orders of magnitude. A shear-thinning fluid of power law exponent 0.15 moves the polymer peak 10% closer to the sidewall than a Newtonian fluid and decreases the required time to fill by nearly 50% compared to the Newtonian fluid for this cavity. In general, a shear-dependent fluid will affect polymer flow when shear is greatest, which occurs for small indenter widths, large

cavity widths, and small film thickness. The decrease in polymer shear modulus above T_g also promotes increased influence of shear-thinning parameters.

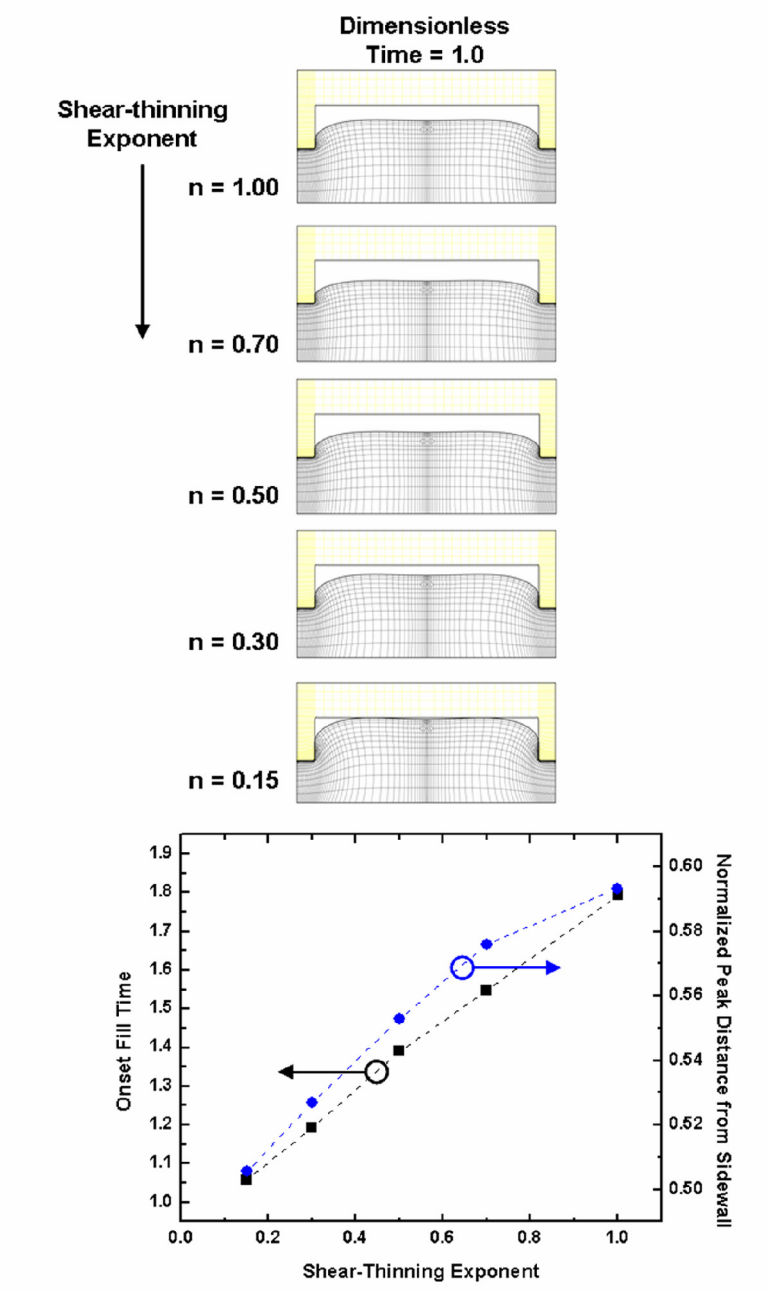

Figure 3-4 Effect of shear-thinning on deformation. Decreasing shear-thinning exponent from 1 (Newtonian) to 0.15 (highly shear-thinning) reduces the polymer viscosity near the vertical cavity wall, moving the polymer peak closer to the indenter sidewall and decreasing the time to fill.

The general trends of polymer flow are similar for cylindrical, as opposed to rectangular, embossing tools. Figure 3-5 compares Newtonian flow for a rectangular cavity and a cylindrical slot with equivalent cavity width and diameter. At $W/h_i = 1.4$, the cylindrical slot is in single peak deformation mode while the rectangular cavity deforms in a dual peak mode. Circumferential confinement in the cylindrical slot delays the transition from single to dual peak deformation to higher values of W/h_i. The cylindrical slot also requires longer time to fill than the rectangular cavity because of the same confinement.

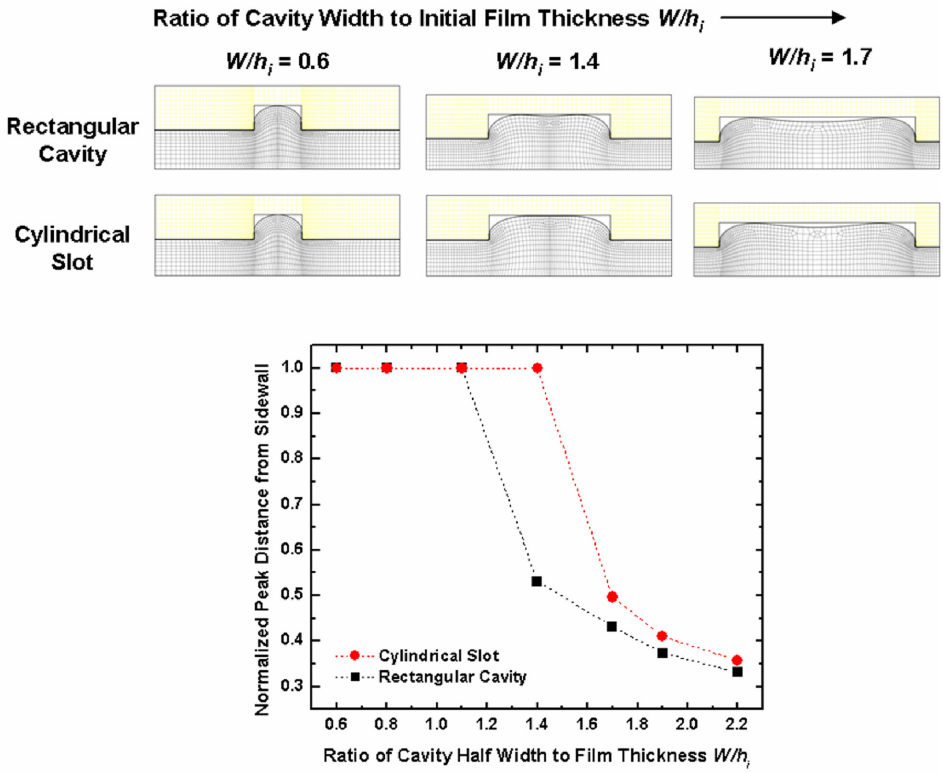

Figure 3-5 Comparison of geometric configuration for given cavity diameter or width. Confined geometry of a cylindrical slot delays the transition from single to double peak for increased cavity diameter. Cylindrical slot also requires longest time to fill.

3.3.2 Cavity Filling Times

Figure 3-6 shows the impact of rectangular cavity geometry and film thickness on fill times for a viscous Newtonian fluid, for several values of *W/(S+W)* and constant *S+W* and h_i. In general, wider cavities fill faster than narrower cavities, and taller cavities on thin polymer films fill slower than shorter cavities on thick polymer films. In all cases, single vs. dual peak deformation mode affects cavity filling time, as the degree of shear

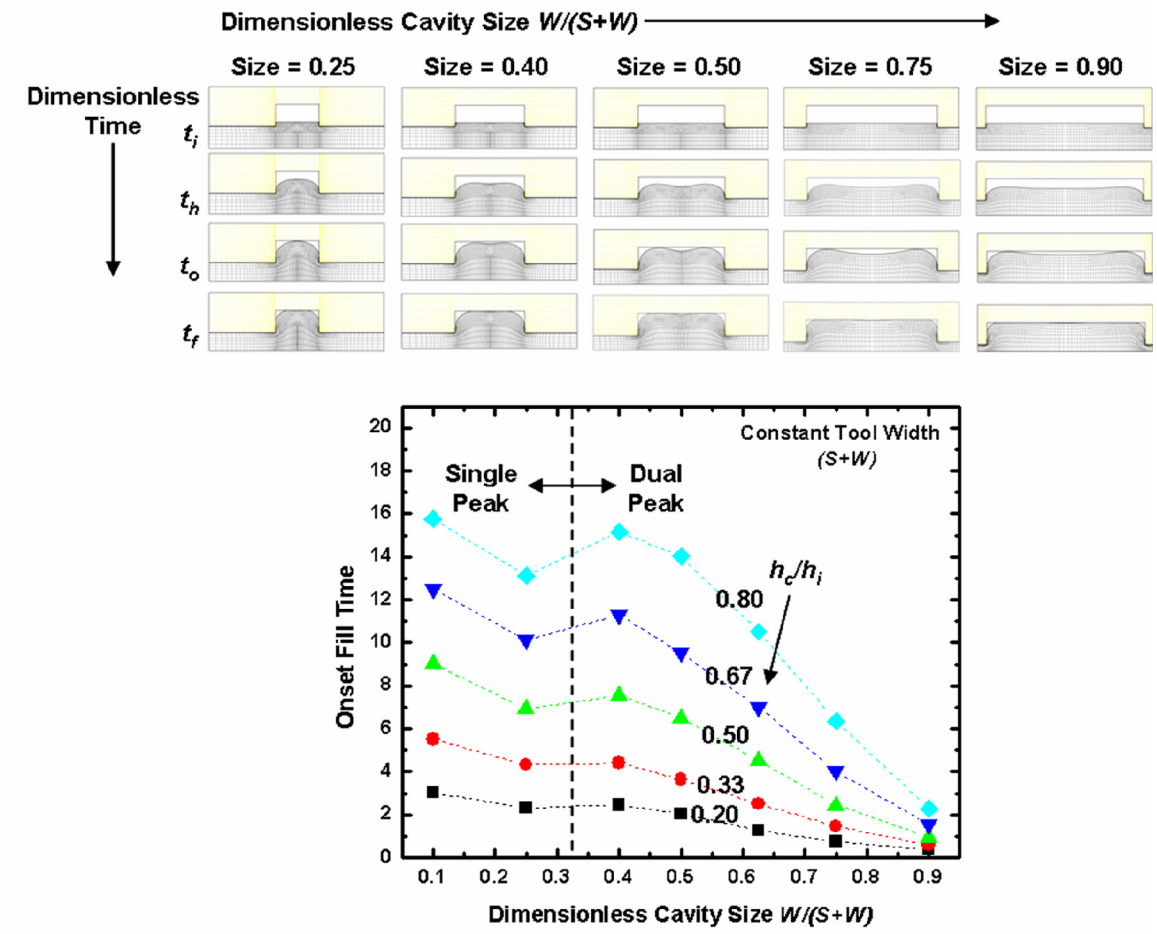

Figure 3-6 Impact of indenter width and cavity height to film thickness ratio on cavity filling. Increasing cavity height to film thickness increases time to fill. For both single and dual peak deformation, increasing the indenter width increases time to fill. Time to fill levels off at decreasing dimensionless cavity size as deformation transitions to single peak and begins to decrease for single peak flow. As cavity size continues to decrease, time to fill eventually increases dramatically as evenly distributed pressure forces polymer to travel thru confined slot.

in the polymer drives the filling. In both single and dual peak flow, it is possible to increase cavity width and/or decrease indenter width to promote shear. Figure 3-7 shows the effect of dimensionless cavity height on fill time. In general, taller cavities fill slower than shorter cavities. The wider cavities reach filling onset more rapidly than the narrower cavities but the overall filling time is not necessarily governed by cavity width.

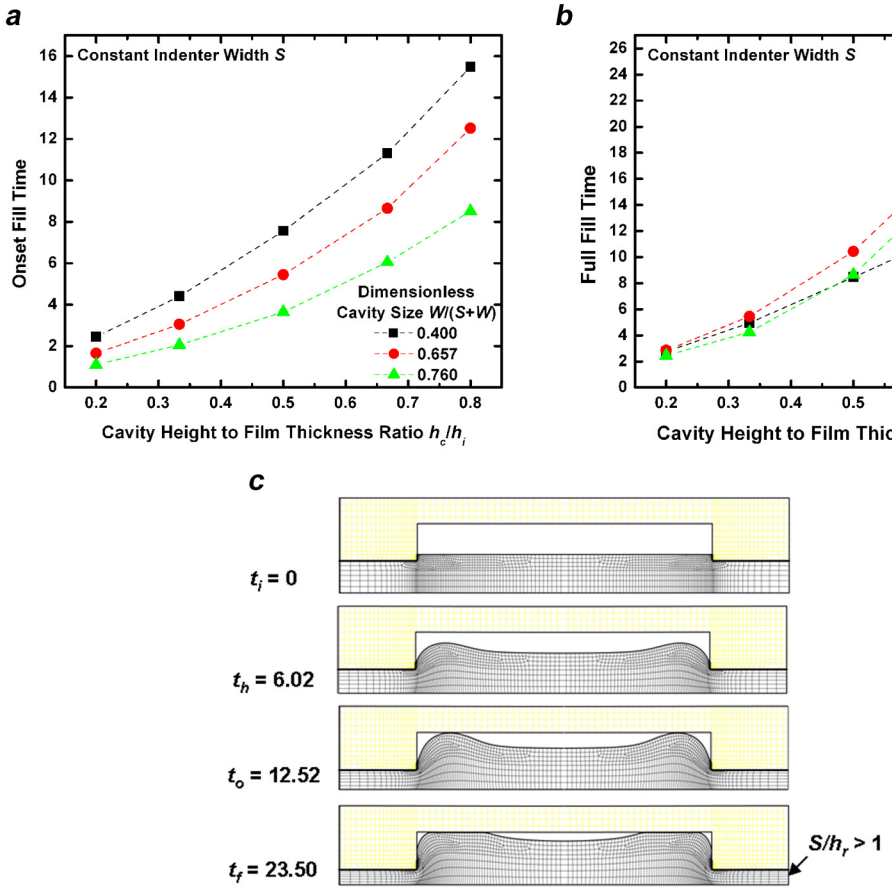

Figure 3-7 Impact of polymer availability on filling time. (a) Small cavity sizes require longest time to begin filling. (b) At large ratios of cavity height to initial film thickness, the indenter width becomes greater than the residual film thickness, resultig in squeeze flow between the indenter and the substrate and a dramatic increase in time to fill. (c) Deformation profile showing the increasing time between fill onset and full filling.

Instead, cavity height and dimensionless cavity size combine to determine overall filling time. Ignoring elastic effects, the residual film thickness h_r, or mold flash, is defined in terms of the initial polymer thickness, cavity height, and dimensionless cavity size as

$$h_r = h_i - \frac{Wh_c}{S+W}. \tag{3.9}$$

As h_c/h_i increases in Figure 3-7b, the ratio of indenter width to residual film thickness increases, resulting in a squeeze flow. As Figure 3-7 shows, once filling begins, the main restriction to polymer flow is not inside the cavity but between the indenter and the hard substrate. Squeeze flow in the polymer film becomes important as the indenter width S becomes greater than the residual film thickness h_r, i.e. when $S/h_r > 1$.

3.4 Discussion

The polymer deformation predicted here agrees well with a number of articles that measure and model polymer deformation from the 10 nm to 1 mm scale. Nearly every report observed deforming polymer peaks located ~h_i from the master sidewall [20-22, 29-32], with single peak deformation when the cavity half width was less than polymer film thickness, $W < h_i$, and dual peak deformation for cavity half width greater than polymer film thickness, $W > h_i$. The value W/h_i defined dual vs. single peak polymer deformation for measurements on films of thickness 1.2 mm [20], 500 μm [21], and 20 μm [29]. Experiments in 1.7 μm films [30] found single peak deformation at $W/h_i > 2$ while the present simulations predict dual peak deformation at $W/h_i > 1.2$, however the discrepancy can be attributed to stress relaxation upon demolding following elastic rather than viscous deformation. Simulations that excluded surface tension examined

embossing of 200 nm thick polymer films and produced single peak deformation for $W/h_i < 1$ and dual peak deformation for $W/h_i > 1$ [22]. The Newtonian liquid deformations presented here agree with nonlinear solid elastic deformations [31, 32] that also noted cavity geometry and initial film thickness modulate deformation mode. The similarity of results between the nonlinear solid elastic and Newtonian liquid simulations arises since both material models represent the polymer as an incompressible, isotropic material under conditions where surface tension is not important.

The effects of film thickness and cavity geometry on filling time also agree well with reported values over a significant breadth of length scales. All of the referenced studies state that decreasing h_i or increasing h_c/h_i increases either the filling time [17, 18, 30] or the filling pressure [31, 32]. For the present viscous liquid simulations, time and pressure are linearly related in the non-dimensionalization. In solid mechanics simulations [32], both low and high aspect ratio structures required higher pressures to fill the cavity than intermediate aspect ratios. The present simulations agree with this previous finding and explain the phenomena by linking filling time to deformation mode, as shown in Figure 3-6 and Figure 3-7.

The ratio W/h_i accurately predicts single vs. dual peak deformation, indicating whether the polymer flow is mostly vertical or mostly lateral. As such W/h_i can be thought of as the *directional flow ratio*. The ratio S/h_r predicts shear flow vs. squeeze flow, providing a metric for the amount of polymer that must be displaced from beneath the indenter to fill the cavity. As such S/h_r can be thought of as the polymer supply ratio. Figure 3-8 shows contours of the mean shear rate (deviatoric shear stress) for three cavity widths on the same polymer film, for which there is single and dual peak deformation and

free shear flow between the indenter and substrate, and also for dual peak flow and squeeze flow between the indenter and substrate. For the cases that there is no squeeze flow between the indenter and the substrate, there is a plug of non-deforming polymer in the cavity center. This plug is pushed upward in single-peak flow, but does not move in

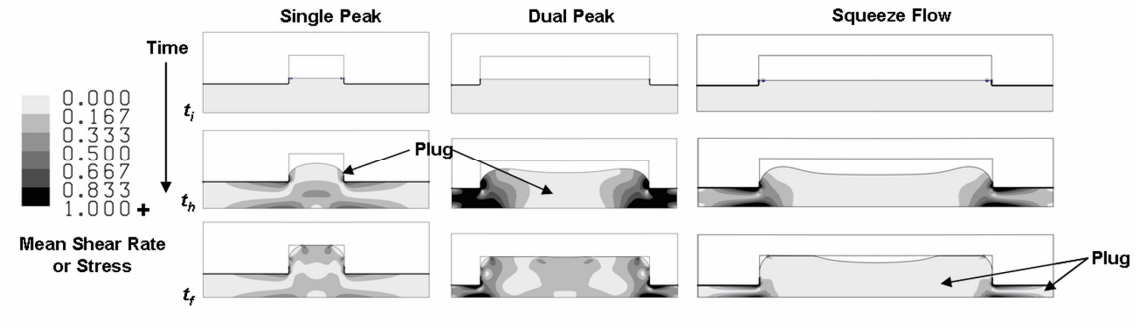

Figure 3-8 Mean shear rate or deviatoric stress profile. Single peak flow pushes non-shearing fluid plug vertically in a single polymer peak. Dual peak flow results from shear near the indenter sidewall with non-shearing fluid plug in cavity center. As flow transitions from shear-dominant to squeeze-dominant, a non-shearing fluid plug develops underneath the indenter as well as in the cavity center.

the case of dual peak flow, as it is too far from the indenter sidewall to be affected by the induced shear. When the polymer film between the indenter and substrate becomes thin, squeeze flow dominates the polymer filling, with consequences for filling time as well as deformation mode as illustrated in Figure 3-7.

The three different characteristic flow profiles in Figure 3-8 suggest cavity geometry governs filling behavior. Simple viscous flow theory, based on mold geometry ratios, can estimate a characteristic NIL filling time, t_{NIL}, for the filling of each geometry. The case of single peak flow, occuring when $W/h_i < 1$ regardless the value of S/h_r, resembles the classic fluid mechanics problem of steady laminar flow between infinite plates or within a pipe [40]. Assuming fully developed flow in a pipe of length

equivalent to the cavity height with fluid pressure $P(S+W)/S$ and no slip conditions at the boundaries, a characteristic single peak pipe flow fill time can be defined as

$$t_{NIL} = \frac{12\eta h_c^{\,2} S}{P(2W)^2(S+W)}, \tag{3.10}$$

and a characteristic velocity, V_{NIL}, may be found by dividing the distance the polymer must travel, i.e. the cavity height, by t_{NIL}:

$$V_{NIL} = \frac{P(2W)^2(S+W)}{12\eta h_c S}, \tag{3.11}$$

Fill times estimated by Eq. 3.10 correlate well with single peak fill times simulated here when $W/h_i < 0.5$. However, when $W/h_i > 0.5$, Eq. 3.10 underestimates simulated fill times by a factor of ~ 3 - 5. For these cases, simulated fill times seem to resemble flow through an abrupt expansion from a flow channel of h_i to $h_i + h_c$, resulting in roughly 60 - 80% head loss for the geometries simulated here [40]. Modifying Eq. 3.10 accounting for the expansion loss coefficient provides a better estimate for fill time when $0.5 < W/h_i < 1$. For the case of dual peak squeeze flow, when $W/h_i > 1$ and $S/h_r > 1$, the cavity filling time can be estimated by applying the lubrication approximation when assuming a fluid is squeezed out between infinite plates of width twice the indenter width moving at constant velocity due to an applied load. The situation of cavity filling in NIL cannot be accurately defined so simply since the polymer is expelled into a finite pressure field due to confinement and because the effective pressure decreases as more polymer comes into contact with the cavity surface, thus slowing the imprint. An approximation near the upper bound of cavity filling time for the squeeze flow process could use infinite plates of width twice the tool width rather than the indenter width, however this approximation can grossly overestimate the required time to fill. A reasonable characteristic squeeze

flow filling time can be estimated as the time required to squeeze a fluid from the initial film thickness to the residual film thickness by infinite plates of width twice the tool width weighted by the ratio of indenter width to tool width:

$$t_{NIL} = \frac{\eta(S+W)^2}{2P}\left(\frac{1}{h_r^{\,2}} - \frac{1}{h_i^{\,2}}\right) * \left(\frac{S}{S+W}\right), \tag{3.12}$$

This time is similar to the fill time defined by [17] but different by choice of plate width and weighting. A characteristic squeeze flow velocity can be found by dividing the difference in initial film thickness and residual film thickness by t_{NIL}: $V_{NIL}=(h_i-h_r)/t_{NIL}$. V_{NIL} is therefore

$$V_{NIL} = \frac{2P}{\eta S(S+W)} \frac{h_i^{\,2} h_r^{\,2}}{h_i + h_r}, \tag{3.13}$$

This velocity is close to the imprint velocity defined by [22] but again different by choice of plate width and weighting. The squeeze flow characteristic fill time best approximates simulated fill times at large W/h_i when the polymer squeezed from beneath the indenter meets low pressure resistance in the cavity center. For dual peak shear free flow when $W/h_i > 1$ and $S/h_r < 1$, a different characteristic fill time may be defined based on Stokes flow [41]. Like squeeze flow filling, shear flow filling will be slowed as more polymer contacts the cavity surface. Hence a practical estimate for a characteristic Stokes fill time can be defined using the tool width, rather than the indenter width, as the indenting surface, giving

$$t_{NIL} = \frac{6\eta}{P(S+W)}(h_i - h_r), \tag{3.14}$$

and a corresponding characteristic Stokes velocity of

$$V_{NIL} = \frac{P(S+W)}{6\eta}, \tag{3.15}$$

The parametric simulation study presented in this paper identifies two geometric ratios that distinguish four characteristic filling modes. Regardless of length scale, directional flow ratio W/h_i and polymer supply ratio S/h_r can determine constrained single peak flow, single peak expansion flow, shear or Stokes flow, and squeeze flow. Filling time predictions based on characteristic filling mode Eqs. 3.10, 3.12, and 3.14 predict simulation results well within an order of magnitude approximation for all cases. Filling time estimates for constrained single peak flow and single peak expansion flow best match simulation results. Filling time predictions for geometries near the single to dual peak transition deviate more from simulation results than geometries deforming in constrained dual peak mode. The weighted Stokes flow filling time predictions do not capture differences in filling times due to changing ratios of S/W, but geometries in Stokes flow fill in short times so that differences are often not of practical importance. The weighted squeeze flow velocity captures the importance of both the indenter width and the total tool width to provide an order of magnitude fill time estimate.

While the directional flow ratio and polymer supply ratio describe phenomena observed in a large number of embossing studies, the two geometric ratios do not distinguish all of the various physics of published NIL deformation studies. However, when the characteristic times predicted by W/h_i and S/h_r define an appropriate characteristic velocity V_{NIL}, a new Capillary number characteristic of the imprint process can be defined, $Ca_{NIL}=\eta V_{NIL}/\sigma$. From Eqs. 3.11, 3.13, and 3.15, the viscosity dependence of V_{NIL} eliminates the viscosity dependence of Ca_{NIL}.

Three parameters, Ca_{NIL}, W/h_i, and S/h_r, can predict all of the previously reported polymer deformation modes during NIL. Ca_{NIL} determines viscous vs. capillary driven flow, the directional flow ratio W/h_i predicts single or dual peak flow, and the polymer supply ratio S/h_r determines shear-dominant Stokes flow vs. squeeze flow. Table 1 lists imprint parameters from a number of articles that examined polymer flow during embossing and also lists Ca_{NIL}, W/h_i, and S/h_r. Figure 3-9 shows two regime maps of polymer filling modes and plots the simulations and experiments listed in Table 1. Figure 3-9a shows the determination of V_{NIL} from W/h_i and S/h_r and Figure 3-9b shows flow driving mechanism defined by W/h_i and Ca_{NIL}. When located on the regime maps of

Table 1 Comparisons of millimeter, micrometer, and nanometer scale imprinting. All studies are for negligible Reynolds number flows ($Re \sim 10^{-14}$). Using a characteristic velocity derived from viscous flow theory, all different flow regimes reported may be characterized by capillary number and geometry ratios. The NIL capillary number is independent of viscosity.

Experiment	h_r (nm)	h_r/h_i	W/h_i	S/h_r	V_{NIL} (nm/sec)	Ca_{NIL}	Flow Profile
Rowland [29]	5.67×10^3	0.63	**1.11**	**0.35**	6.0×10^1	$\mathbf{2.0 \times 10^3}$	Single Peak Viscous
Rowland [29]	5.30×10^3	0.59	**2.78**	**0.38**	1.4×10^2	$\mathbf{4.6 \times 10^3}$	Dual Peak Viscous
Rowland [42]	2.67×10^3	0.44	**4.17**	**1.88**	1.2×10^1	$\mathbf{4.0 \times 10^2}$	Dual Peak Viscous Squeeze
Heyderman [17]	1.56×10^2	0.78	**50**	**192**	5.5×10^0	$\mathbf{5.5 \times 10^{-4}}$	Dual Peak Capillary Squeeze
Jeong [22]	1.94×10^2	0.97	**2.5**	**77.2**	4.0×10^1	$\mathbf{4.0 \times 10^{-3}}$	Dual Peak Capillary Squeeze
Jeong [22]	1.99×10^2	0.99	**0.25**	**75.2**	5.7×10^3	$\mathbf{5.8 \times 10^{-1}}$	Dual Peak Capillary-Viscous Squeeze or Confined Singled Peak (Wet-dependent)
Cross [43]	1.29×10^3	0.76	**2.94**	**4.66**	9.8×10^{-1}	$\mathbf{3.3 \times 10^1}$	Dual Peak Viscous
Cross [43]	1.29×10^3	0.76	**2.94**	**4.66**	7.5×10^0	$\mathbf{2.5 \times 10^2}$	Dual Peak Viscous
Cross [43]	3.68×10^1	0.08	**11.1**	**163**	1.7×10^{-4}	$\mathbf{5.9 \times 10^{-3}}$	Dual Peak Capillary Squeeze
Hirai [31]	-1.5×10^1	-0.1	**4.17**	**-33.3**	3.7×10^{-4}	$\mathbf{1.3 \times 10^{-1}}$	Dual Peak Capillary-Viscous Squeeze
Hirai [31]	1.15×10^2	0.46	**2.00**	**4.35**	2.7×10^{-2}	$\mathbf{9.2 \times 10^0}$	Dual Peak Viscous-Capillary Squeeze
Hirai [31]	2.25×10^2	0.63	**1.39**	**2.22**	1.4×10^{-1}	$\mathbf{4.5 \times 10^1}$	Dual Peak Viscous
Juang [20]	6.40×10^5	0.53	**2.92**	**2.34**	1.0×10^3	$\mathbf{2.0 \times 10^4}$	Dual Peak Viscous
Shen [21]	4.50×10^5	0.90	**0.20**	**0.22**	1.2×10^2	$\mathbf{4.0 \times 10^3}$	Confined Single Peak Viscous
Austin [3]	9.50×10^1	0.95	**0.07**	**0.07**	3.4×10^{-1}	$\mathbf{1.2 \times 10^{-2}}$	Confined Single Peak Capillary (Non-wetting)
Yu [44]	4.64×10^1	0.22	**1.07**	**7.01**	2.1×10^0	$\mathbf{7.1 \times 10^{-2}}$	Single Peak Capillary (Non-wetting)

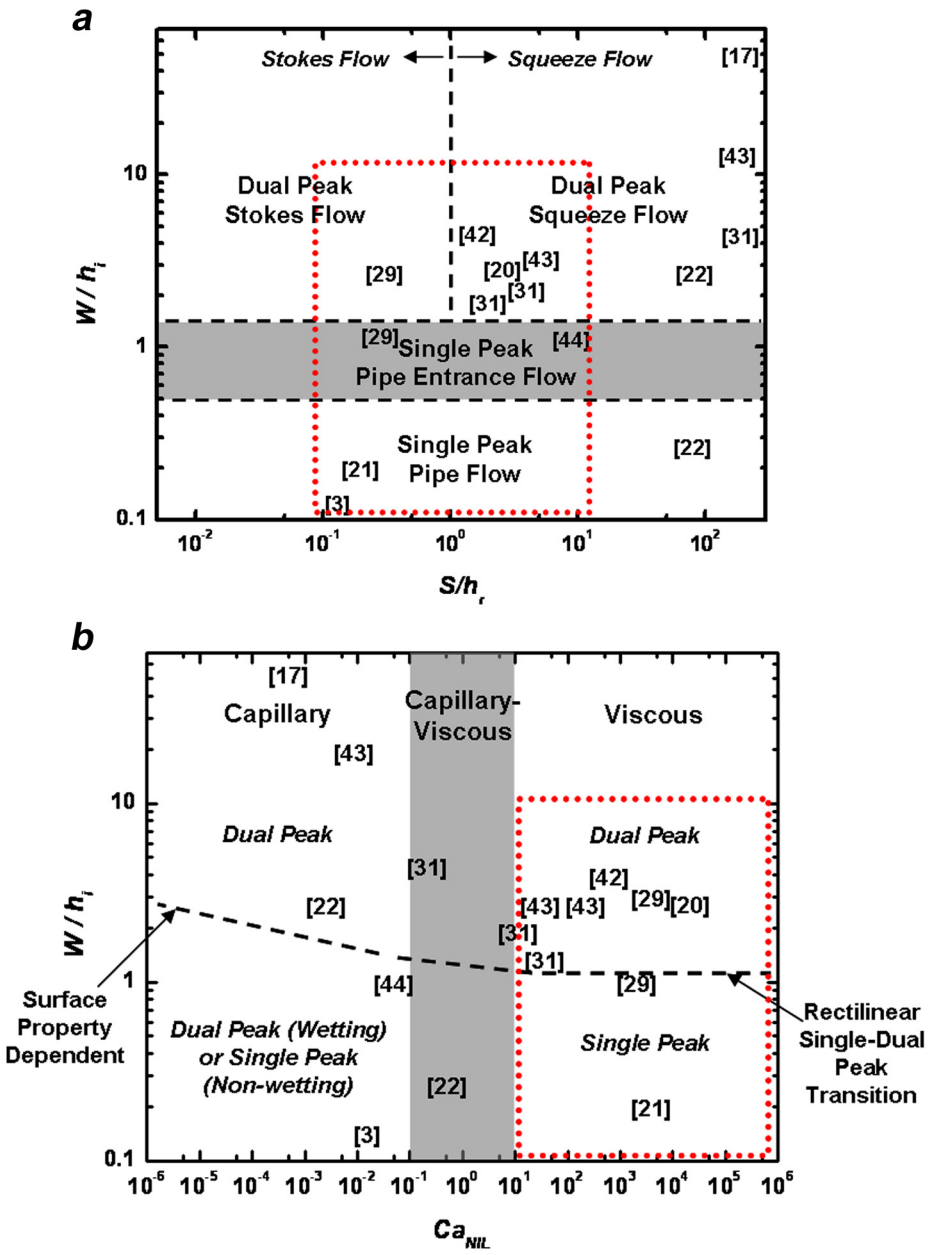

Figure 3-9 NIL polymer deformation regime maps for NIL capillary number Ca_{NIL}, directional flow ratio W/h_i, and polymer supply ratio S/h_r. All of the NIL flows reported in the reference of Table 1 are located on the maps, and fall into the polymer flow regime predicted by the theory of the present paper. The dotted square indicates the simulation space of this work. (a) Directional flow ratio and polymer availability determine characteristic velocity governing polymer deformation. When the indenter width is greater than the polymer film thickness squeeze flow between the indenter and the substrate dominates deformation, resulting in significantly longer fill times than Stokes flow. Single peak flow also requires longer filling times than Stokes flow as the small cavity width restricts free flow. (b) The effect of cavity geometry and polymer film thickness on polymer deformation. Ca_{NIL} governs viscous vs. capillary flow, and W/h_i governs single vs. dual peak polymer deformation. The dashed line indicates transition between single and dual peak deformation. Confinement in cylindrical geometries vertically shifts the single-dual peak transition line.

Figure 3-9, all of the experiments and simulations of Table 1 fall within their region of reported flow behavior. For the present simulations and the viscous deformation measurements of cited references [20, 21, 29, 30], the single vs. dual peak deformation is independent of capillary number and is determined by geometry only. A cylindrical slot can shift the transition from single to dual peak deformation to a higher value of W/h_i than occurs in rectilinear cavities.

Surface tension can influence filling time and the single to dual peak transition in capillary flows. In the capillary flow regime, capillary forces can speed up or slow down the fill time due to surface tension and wettability when the viscous timescale permits. As capillary forces become significant relative to viscous forces, the transition from single to dual peak deformation can occur at higher values of W/h_i than in purely viscous flow as the surface forces act to minimize the polymer surface area. The region where viscous forces are comparable to capillary forces is shaded in Figure 3-9. Competing viscous and capillary forces can explain the flat deformation profile resulting from a wetting fluid filling a thin cavity observed by [22]. In the strictly capillary region, transition from single to dual peak deformation depends strongly on surface chemistry. For a wetting fluid having a small contact angle with the master sidewall, the fluid will wet the master surface and climb the indenter sidewalls in a dual peak mode, independent of W/h_i. This wetting behavior has been observed by [17, 18, 22].

Extensive studies of non-wetting capillary flow in NIL have not been reported, however, the simulation results discussed here and the studies of wetting capillary flow previously published allow for predictions of possible modes of polymer deformation. The deformation behavior for a non-wetting fluid is more complex than for a wetting

fluid, and can depend on surface tension, contact angle, viscosity, pressure, film thickness, and cavity spacing. For a non-wetting fluid with large contact angle, polymer flow will be governed by the ratio of pressure and surface tension. The classical form of the Young-Laplace equation relates the radius of curvature of a fluid surface with the surface tension:

$$\Delta P = \sigma\left(\frac{1}{R_1}+\frac{1}{R_2}\right), \tag{3.16}$$

where ΔP is the pressure difference across the fluid interface and R_1 and R_2 are the principal radii of curvature. For a surface confined in only one direction, R_1 is finite while R_2 is infinite. The range of surface tension values for common engineering materials spans only 1-2 orders of magnitude [40] and thus for a given cavity, changes in embossing pressure will affect the curvature of the deforming polymer. While in the viscous regime, W/h_i alone modulates single to dual peak transition, for a non-wetting fluid in capillary flow, the single to dual peak transition also depends on surface tension and contact angle, and in general occurs at larger W/h_i. Furthermore, for a non-wetting fluid capillary flow, the impact of cavity curvature is more important than for rectangular cavities, and thus single to dual peak transition in a cylindrical cavity is shifted to higher W/h_i than for a rectilinear cavity.

The three parameters W/h_i, S/h_r, and Ca_{NIL}, can guide NIL process design. The directional flow ratio W/h_i distinguishes between vertical and lateral mold filling, which is important for replicating smooth surfaces of unfilled cavities as in the NIL manufacture of optics components. The polymer supply ratio S/h_r gauges the tradeoff between relative filling time and residual film thickness. The residual film thickness is critical for nanoelectronics fabrication where the mold flash must be removed before further

processing. High values of the polymer supply ratio may also be unattainable in glassy or glass-like polymer systems [30, 45]. Ca_{NIL} determines the dominant flow driving mechanism in NIL and defines the imprint regimes where surface chemistry must be considered. In the viscous regime, modulating polymer viscosity through pressure or temperature can improve replication time.

The above discussion of capillary and viscous flow distinguished by geometry ratios is derived from the viscous simulations of this paper. Possible simulation errors could arise due to inadequate mesh size, time step size, and mesh distortion, however the residual tolerance control of the simulation prevents these errors from dramatically influencing results. The hybrid initial no-slip, slip contact condition could influence the filling time by a factor of two-thirds, though this factor is not large enough to change filling time predictions. Elastic effects could alter the deformation profile observed and cause undesirable shape loss upon demolding after short fill times, but long dwell times or increased temperatures can reduce if not eliminate elastic contributions to flow. As resolution limits decrease, size effects due to constraining the radius of gyration of the polymer could significantly alter the fill time predicted by the guidelines of this paper, though no such effects have yet been observed during NIL.

3.5 Conclusion

This chapter performs simulations of viscous polymer flow during nanoimprint lithography, investigating the effects of imprint cavity geometry, polymer film thickness and properties, and process parameters. Polymer deformation and fill time is governed by location and rate of polymer shear during imprinting, exhibiting deformation

predominantly close to the vertical indenter sidewall that can result in single peak or dual peak deformation modes. The continuum simulations capture the NIL physics observed by numerous published articles from the 10 nm to 1 mm scale.

Three parameters, W/h_i, S/h_r, and Ca_{NIL}, accurately predict polymer deformation and filling mode. The directional flow ratio W/h_i predicts importance of deviatoric stress determining single or dual peak deformation and hence vertical or lateral flow. The polymer supply ratio S/h_r predicts the influence of squeeze flow and relative filling times independent of material rheological properties. The NIL Capillary number, Ca_{NIL}, predicts flow driving mechanism to distinguish necessary process design from external embossing setup and internal material physics. The three parameters W/h_i, S/h_r, and Ca_{NIL} combine to allow rational and predictive NIL process design and provide a step towards establishing design rules for NIL. Rather than rely on improvised trial and error, it is possible to use these tools to appropriately tailor tool geometry, process conditions, and polymer rheology and surface chemistry for optimal NIL.

CHAPTER 4

SIMULATIONS OF NON-UNIFORM EMBOSSING: THE EFFECT OF ASYMMETRIC NEIGHBOR CAVITIES ON POLYMER FLOW DURING NANOIMPRINT LITHOGRAPHY

This chapter presents continuum simulations of viscous polymer flow during nanoimprint lithography (NIL) for embossing tools having irregular spacings and sizes. Simulations varied non-uniform embossing tool geometry to distinguish geometric quantities governing cavity filling order, polymer peak deformation, and global mold filling times. A characteristic NIL velocity predicts cavity filling order. In general, small cavities fill more quickly than large cavities, while cavity spacing modulates polymer deformation mode. Individual cavity size, not total filling volume, dominates replication time, with large differences in individual cavity size resulting in non-uniform, squeeze flow filling. High density features can be modeled as a solid indenter in squeeze flow to accurately predict polymer flow and allow for optimization of wafer-scale replication. The present simulations make it possible to design imprint templates capable of distributing pressure evenly across the mold surface and facilitating symmetric polymer flow over large areas to prevent mold deformation and non-uniform residual layer thickness.

4.1 Introduction

Nanoimprint lithography (NIL) is a high resolution [1], large scale [2] thermomechanical manufacturing process where a nanostructured master tool is pressed into a thermoplastic polymer at elevated temperature, forming a negative replica of the master in the polymer substrate. The high throughput process offers an economical alternative to standard silicon based fabrication technologies for nanoelectronics or nanoelectromechanical systems (NEMS). Practical implementation of NIL will require multiple non-uniform-sized feature geometries on a single tool, while retaining small and uniform residual layer thickness. A deep understanding of both local polymer flow in simple geometries and of global polymer flow in irregular fields is required for rational process and master tool design. This chapter presents simulations embossing molds of non-uniform feature sizes and spacings into viscous polymer to investigate polymer flow and mold filling time during NIL.

Previous experiments and simulations investigating hot embossing manufacturing (HEM) and NIL have focused on understanding polymer flow in simple uniform geometries or single indenter tools [17, 22, 29-32, 42, 45]. Factors influencing polymer flow have included shear deformation, elastic stress release, non-linear rubber-like elastic dynamics, capillary flow, and viscous flow. In general, deformation mode was found to depend on geometric flow restrictions and time scale of flow [42].

A few groups have studied large-scale flow field effects with non-uniform embossing tools [18, 46-48], noting limitations in simultaneous replication of patterns having large and small features in close proximity. Correlation and crosstalk of stress and flow fields of simple geometries arises when a single embossing tool contains

multiple, non-uniform feature geometries. Non-uniform filling increases the tool-polymer contact area, slowing the speed of imprint. Viscous polymer flow over large areas limits full replication and uniformity of residual layer thickness as incomplete filling and tool warping result due to non-uniform deformation. Simultaneous replication of combined features having significantly different sizes requires long imprint times compared to uniform fields [18, 46, 47, 49]. Step and Flash NIL, laser-assisted NIL, and one-step imprint-photolithography can displace a smaller volume of material and/or imprint at lower viscosities than conventional embossing [49-51], but conventional embossing is more robust for materials compatibility.

This chapter presents simulations of viscous polymer deformation during NIL embossing with non-uniform embossing tools. Independent variation of cavity width and indenter width or cavity spacing of side-by-side non-uniform geometries allows examination of parameters governing polymer deformation and filling time. Characteristic NIL velocity, V_{NIL}, of local cavities governs order of complete cavity filling, indenter width determines order of onset of filling, and individual cavity size difference dominates overall replication time for shear and squeeze flow. Small cavity sizes generally fill first though cavities filling via constrained single peak deformation require long filling times. Non-uniform filling leads to squeeze flow dominated global filling, suggesting that process design should model high density feature areas as a solid indenter to direct global polymer flow and distribute mold pressure evenly.

4.2 Simulation Overview

Previous simulations of NIL modeled a single repeating embossing cavity with the polymer as a viscous liquid [22, 42] or nonlinear solid elastic [31, 32]. Recent computational fluid dynamics studies modeling the polymer as a viscous liquid simulated a few variations of multiple cavity embossing with non-uniform spacing [52]. The present work uses the finite element multi-physics code *GOMA* to model the moving boundary polymer surface in NIL. An applied force on a rigid silicon indenter presses the embossing tool into the viscous Newtonian liquid polymer. Details of the simulation parameters and boundary conditions are described elsewhere [42]. Briefly, both the liquid polymer and solid indenter are modeled using an arbitrary Lagrangian/Eulerian reference frame [36, 38]. No-slip conditions are applied at the indenter-polymer and polymer-substrate interface and a surface tension is applied to the free surface of the polymer. Figure 4-1 shows a representative non-uniform three-cavity geometry with outer non-symmetric cavities and an inner symmetric cavity. Outer indenter width, outer cavity width, inner indenter width, and inner cavity width are systematically varied to

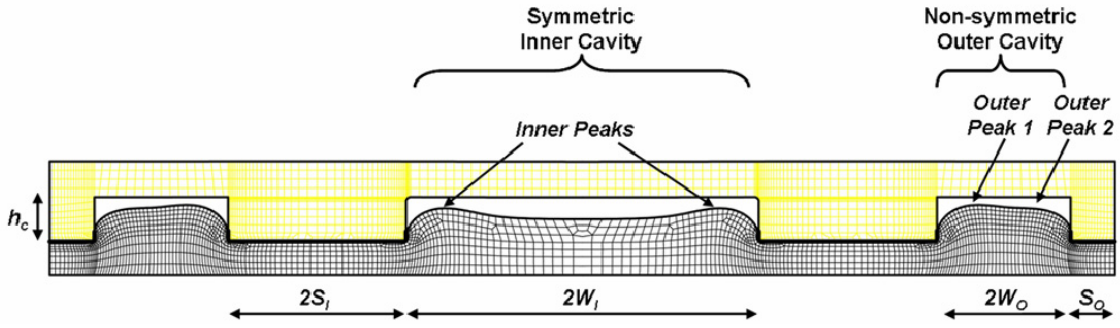

Figure 4-1 Example non-uniform geometry embossing tool showing symmetric inner and non-symmetric outer cavities.

determine which geometric factors govern polymer deformation and cavity filling time. Simulations of a simple two-cavity geometry further investigate the effects of varying indenter widths on replication time.

4.3 Results and Discussion

Simulations investigate embossing of non-uniform geometries into viscous dominant flows with no elastic stress relaxation, i.e. Reynolds number << 1, Deborah number << 1, and NIL Capillary number >> 1 [42]. Analysis of the motion of polymer peaks and the differing individual cavity fill times and global fill times allows determination of parameters governing non-uniform embossing.

Cavity filling order depends on local cavity size and filling mode. Figure 4-2 shows filling modes of non-uniform embossing for both shear and squeeze flows. Local cavity size, defined as the ratio of local cavity width to local tool width, generally predicts which cavities fill first, with smaller cavity sizes filling before larger cavity sizes. Figure 4-2a,b shows cavity filling of squeeze flow with smaller cavities filling before larger cavities. In cavities having dual peak deformation, the polymer peak nearest the largest indenter width will vertically deform faster than the polymer peak nearest the smallest indenter. In Figure 4-2a, more polymer is displaced by the inner indenter than is displaced by the outer indenter, causing the polymer peak nearest the inner cavity to reach the mold first. The indenter width determines which side of a cavity begins filling first, while the cavity size determines which cavity fills first. Figure 4-2c,d shows cavity filling of shear flow where smaller cavity sizes do not always fill before

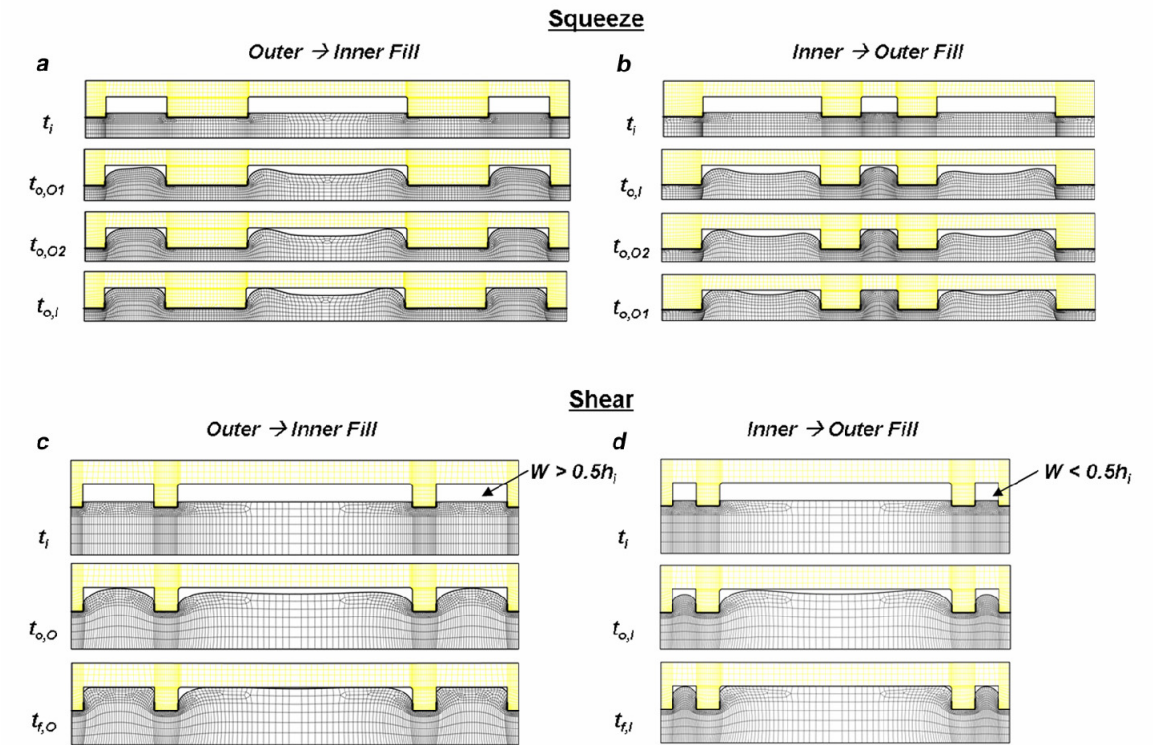

Figure 4-2 Deformation profiles for possible onset deformation modes of (a,b) squeeze flow and (c,d) shear flow. (a,b) The smallest cavity size fills first in squeeze flow, with the direction of the polymer peak governed by the maximum indenter width. (c,d) In shear flow, the smallest cavity size fills first unless the local cavity half width (W) is less than half the film thickness ($0.5h_i$). When $W < 0.5h_i$, hydrostatic stress in the small cavity slows filling, allowing large cavity sizes to fill first. V_{NIL} can predict cavity filling order.

larger cavity sizes, with small cavity sizes filling first in Figure 4-2c and large cavity sizes filling first in Figure 4-2d. The size of the single peak cavity strongly influences filling order. When the cavity size is sufficiently small, constrained single peak flow occurs, resulting in large cavity sizes filling before small cavity sizes. Constrained single peak flow occurs when the local cavity half width is less than approximately half the film thickness. The order of filling for individual cavities can be predicted by comparing the appropriate shear flow, squeeze flow, or single peak flow V_{NIL} [42] for all the individual cavities on a mold.

The difference in adjacent cavity filling times increases as the local cavity size difference increases, forcing more polymer to be displaced over larger distances than in a

uniform deformation field. Figure 4-3 shows the effects of decreasing inner cavity size due to an increasing inner indenter width. As the inner indenter width increases, more polymer is available to fill the cavity, and the excess polymer is forced longer distances to fill the remaining vacant cavities than for the case of a smaller indenter width. Figure 4-3b shows the polymer peak nearest the inner cavity is pushed away from the sidewall as filling progresses and the polymer peak farthest the inner cavity is pushed towards the

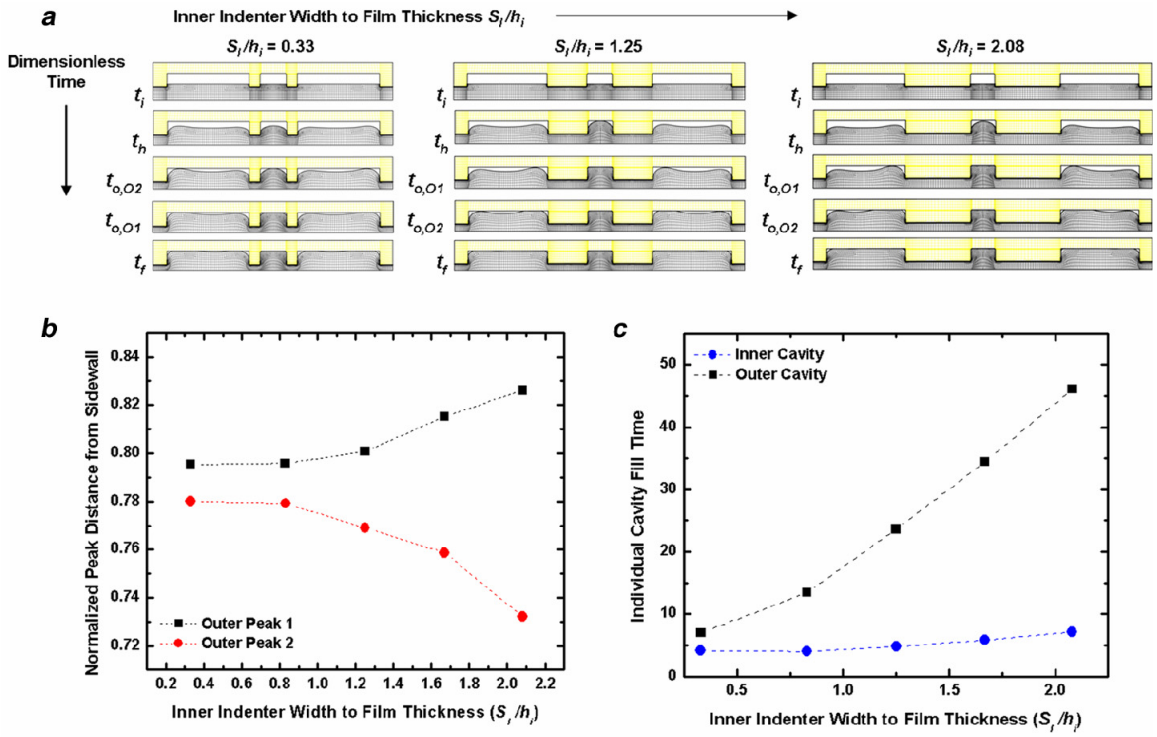

Figure 4-3 (a) Deformation profiles for increasing inner indenter width. (b) The increased material forced from beneath the inner cavity and indenter pushes the outer peak 1 away from the sidewall and outer peak 2 closer to the sidewall while (c) dramatically increasing the fill time of the outer cavity.

sidewall as inner indenter width increases. The increase in inner indenter width increases the amount of displaced polymer, resulting in a dramatic rise in time to fill for the outer cavity and global filling of the embossing tool, as shown in Figure 4-3c. The increase in inner indenter width has little effect on the filling time of the inner cavity, since ample

polymer is locally available to fill the cavity and single peak flow is limited by the flow of polymer into the cavity, not the flow of the indenter into polymer [42]. As the ratio of polymer available to polymer required for local cavity filling increases, long range flow effects develop causing polymer transport between global tool sections, as noted in [47]. Figure 4-3c shows total time to fill increasing with increasing inner indenter width and total indenter width, i.e. the sum of the inner and outer indenter width. To determine whether the total indenter width or the maximum single indenter width, i.e. the greater of the inner or outer indenter width, governs fill time, a simple two cavity geometry was modeled. Figure 4-4 shows the change of fill time due to maximum indenter width in the two cavity geometry. For constant total indenter width and varying maximum indenter width, dramatically different fill times result. The fill times depend not on total indenter width but instead on maximum indenter width. Viscous flow theory of a thin layer of fluid between plates, using the lubrication approximation, predicts a quadratic dependence of fill time on indenter width. The quadratic dependence of fill time on maximum indenter width observed here results in a characteristic NIL fill time approximated by

$$t_{NIL} = \frac{\eta S_{MAX}{}^2}{2P}\left(\frac{1}{h_r{}^2} - \frac{1}{h_i{}^2}\right) * \left(\frac{S_{MAX} + W}{S_{MAX}}\right) \tag{4.1}$$

where η is the polymer viscosity, S_{MAX} is the maximum indenter width, W is the cavity half width adjacent to the maximum indenter width, P is the embossing pressure, h_r is the residual film thickness, and h_i is the initial film thickness [42].

The fill time dependence on the maximum indenter width has consequences for global replication time. In common embossing applications, S_{MAX}/h_i usually is or

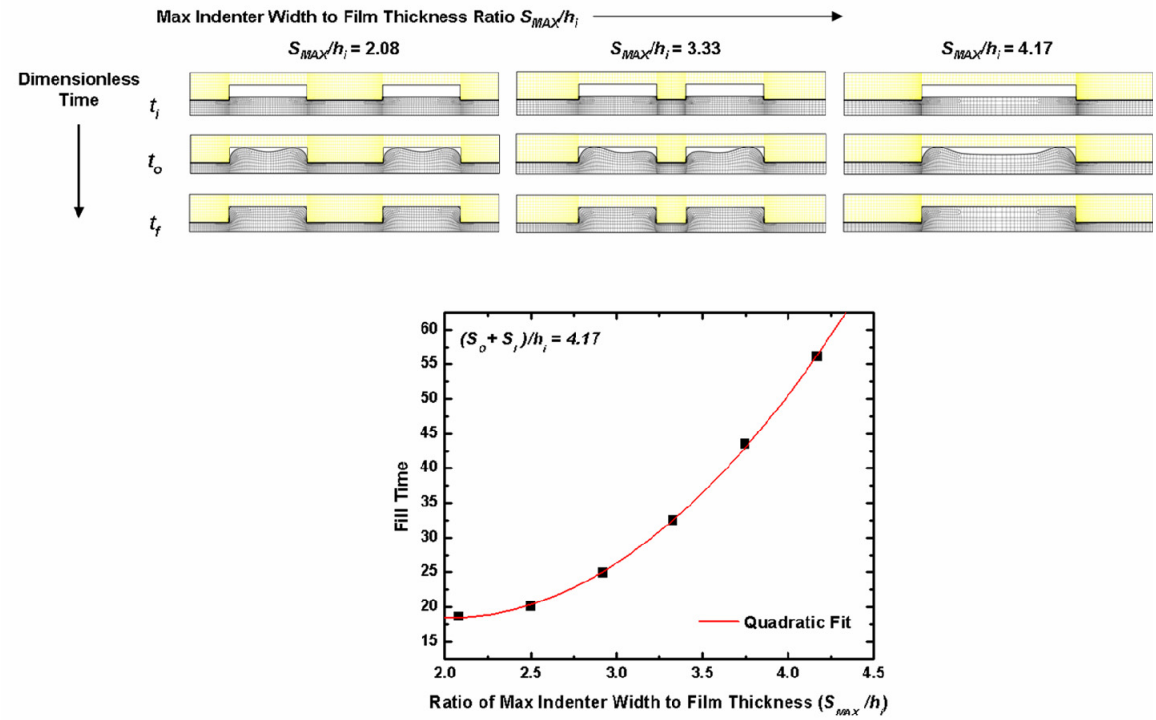

Figure 4-4 Fill times for various indenter width ratios with total indenter width constant. The quadratic fill time dependence on indenter width ratio shows that squeeze flow fill time is characterized by the maximum indenter width of the system.

becomes > 1, thus governing relations based on squeeze flow apply [42]. The quadratic dependence of fill time based on maximum indenter width shown in Figure 4-4 allows prediction of filling time. Figure 4-5 shows global fill time based on local cavity size. When large differences in cavity size exist, certain individual cavities quickly fill relative to the global filling time, and the embossing condition closely approximates squeeze flow of an indenter width that includes the filled cavity width. The close correlation of the single indenter, three cavity geometry, and squeeze limit geometry at large differences of outer and inner cavity sizes illustrates the validity of a global squeeze flow approximation. At larger negative differences of outer and inner cavity sizes than shown in Figure 4-5, the fill time of the three cavity geometry will again approach the fill time of the limiting squeeze flow case.

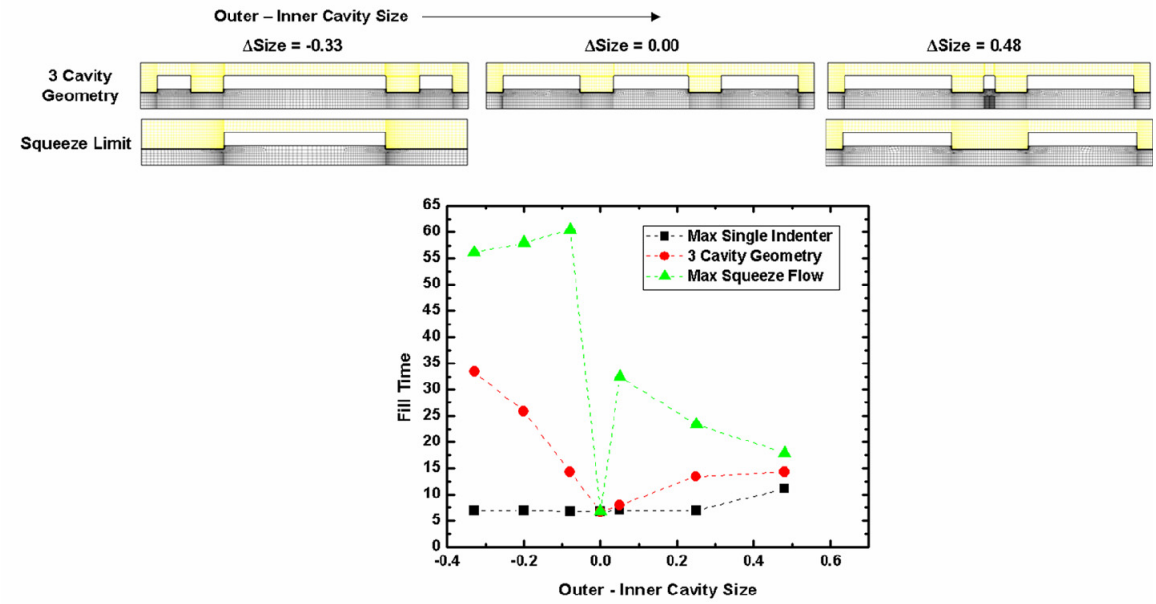

Figure 4-5 Cavity size governs filling. Small cavity sizes generally fill first unless small cavities deform via a constrained single polymer peak. Large differences in cavity size increase fill time. Lower bound is maximum time to fill of a single, symmetric cavity. Upper bound is maximum time to fill for a squeeze flow configuration assuming one cavity initially filled. Global filling of molds can be approximated by squeeze flow of polymer over large areas.

For global mold design of a non-uniform embossing tool, maximum indenter width governs global filling time. In combined large scale and nano-scale imprinting, the quickly filled nano-scale cavities will represent a larger effective maximum indenter width than the maximum indenter width prior to embossing. Areas of slow-filling constrained single peak flow can also be approximated for global mold design as a filled area representing a maximum indenter width, since ample polymer supply is available to locally fill the cavities and excess polymer must be transported to other regions of the mold. With knowledge of field dimensions, a global time to fill can be determined from a piecewise filling of smaller geometries with

$$t_{NIL} = \frac{\eta}{2P}\sum_{i=1}^{N} {S_{MAX,i}}^2 \left(\frac{1}{{h_{r,i}}^2} - \frac{1}{{h_{r,i-1}}^2} \right) * \left(\frac{S_{MAX,i} + W_i}{S_{MAX,i}} \right) \tag{4.2}$$

where $S_{MAX,i}$, W_i, and $h_{r,i}$ depend on the filling of areas of locally small cavities. When cavity sizes vary greatly over a global embossing tool, due to the quadratic dependence of fill time on indenter width, the limiting effective S_{MAX} can alone dominate the fill time. The filled small-sized flow field characterizing non-uniform embossing agrees well with reports that long-range residual layer uniformity resulting from polymer flow between sections of different pattern density is independent of pattern size [47].

4.4 Conclusion

This chapter reports simulations of viscous polymer flow during NIL replication of non-uniform embossing geometries. Individual cavity characteristic V_{NIL} determines cavity filling order. Relative cavity size and indenter width govern local polymer deformation. Large differences in cavity size lead to non-uniform filling and non-local polymer flow. Maximum indenter width governs filling time with a quadratic dependence and the rapid filling of small cavities results in an increase in effective maximum indenter width.

These simulations suggest that non-uniform embossing tool design should be tailored based on the principles of squeeze flow. Local filling of small cavities could be accommodated by designing embossing tools with symmetric filling over the total stamp area to reduce tool warping. Process design could be tailored by increasing temperature and introducing plasticizers to reduce polymer viscosity. By designing a single, non-uniform embossing tool with knowledge of irregular filling and squeeze flow, simultaneous full replication of large-scale and nanoscale patterns and near-uniform residual layer thickness can be achieved over a predicted time scale.

CHAPTER 5

PREDICTING POLYMER FLOW DURING HIGH TEMPERATURE ATOMIC FORCE MICROSCOPE NANOINDENTATION

This chapter reports predictions of nanometer-scale polymer deformation during nanoprobe indentation at elevated temperature. The simulations assume continuum polymer properties with modified boundary conditions to model sub-continuum polymer mechanical deformation. The indenter is a heated atomic force microscope (AFM) tip and the media is a high molecular weight polymer film where tip radius, film thickness, and polymer coil radius are of similar size, in the range of 20 - 50 nm. The simulations model isothermal conditions, where the tip and polymer are at the same temperature, or nonisothermal conditions where the tip is hot while the polymer is cool. Isothermal simulations with shear-thinning bulk material behavior and full-slip polymer-tip interface predict force, displacement, and displacement rate. Nonisothermal simulations show that the polymer-tip interface temperature governs the bit writing process. The temperature-dependent polymer viscosity varies by several orders of magnitude within 50 nm of the polymer-tip interface, causing highly localized polymer deformation near the tip. Steep viscosity gradients near the tip require the polymer-tip interface temperature exceed the polymer glass transition temperature in order to form indents. In both cases the predictions compare well with experimental data. The continuum simulations allow for improved understanding of high temperature AFM nanoindentation and nanoembossing.

5.1 Introduction

Embossing and molding are simple techniques for high fidelity replication. Recent studies have shown replication of single walled carbon nanotubes with diameter 2 nm via molding [53] and crack tips of size 0.4 nm via casting [5]. Nanoimprint lithography (NIL) [54] offers scalable embossing or molding of sub-10 nm features over large areas [2]. One type of nanoembossing process with applications to data storage is atomic force microscope (AFM) nanoindentation, shown in Figure 5-1, where a sharp conical tip forms indents into a thin polymer film [6]. This chapter seeks to understand nanometer-scale polymer transport in isothermal and nonisothermal AFM nanoindentation with features as small as a few nanometers.

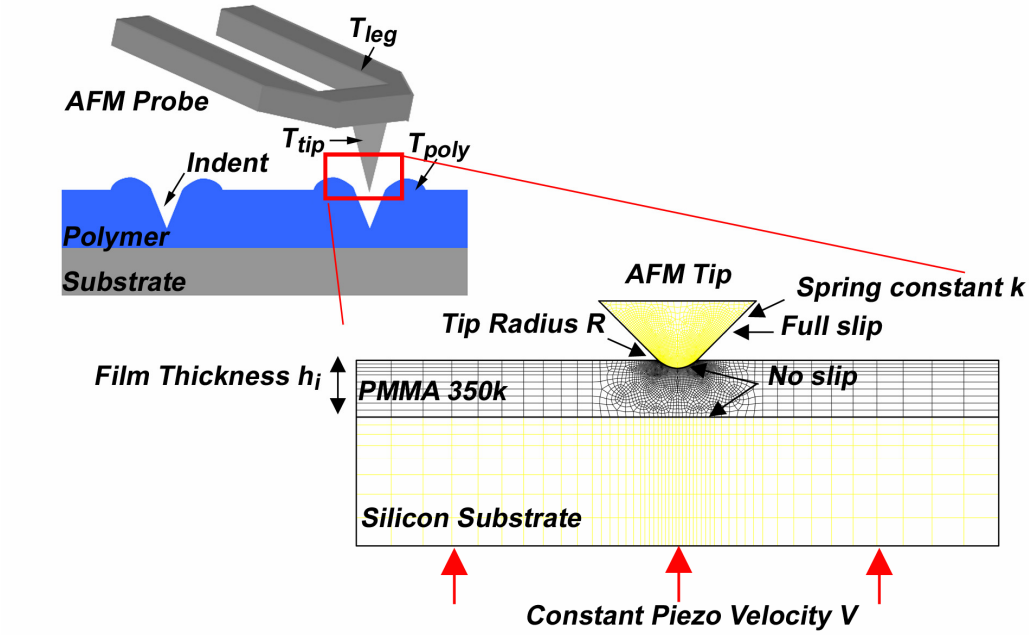

Figure 5-1 Atomic Force Microscope (AFM) nanoindentation. An AFM tip presses into a supported thin polymer layer where the probe leg temperature, tip temperature, and polymer temperature may have different values. The FEM model shows geometry and boundary conditions for isothermal nanoindentation of 350k M_W PMMA at constant piezo velocity. To aid convergence, the tip initially in contact with the polymer does not slip.

As polymer film thickness and indentation sizes shrink to 10 nm during nanoindent formation, the polymer thermomechanical behavior may deviate from that of bulk. The decrease in polymer film thickness increases surface to volume ratio and may confine the polymer molecules, resulting in increased influence of substrate interaction, stress history, and free surface properties on the glass transition temperature T_g and other modes of polymer mobility [14, 55]. Confinement effects appear at film thickness < 100 nm [56] as the polymer free surface can affect chain interactions, resulting in nonuniform T_g profiles across the film [57, 58], reduced temperature dependence of viscosity [59], and suppressed particle diffusion [60].

For data storage [6] and direct-write lithography [61], an AFM tip embosses a thin polymer film that is constrained by a substrate. The polymer is typically a high molecular weight (M_W) thermoplastic. Figure 5-1 shows the AFM nanoindentation process, where the polymer deformation is localized to the region near the tip. The key length scales in these nanometer-scale deformations are the tip radius, R_{tip}, polymer radius of gyration, R_g, Navier slip length, and tube diameter or distance between polymer entanglements ξ_o [62]. In AFM nanoindentation of high M_W polymer films, $R_{tip} > \xi_o$ and $R_{tip} \sim R_g$, suggesting that the viscous flow will be full-slip at the polymer-tip interface [62]. However, polymer viscosity at this scale may deviate from bulk viscosity due to molecular confinement in the film of thickness < 100 nm [56].

Several experiments of AFM nanoindentation have shown that the measured polymer response is different than would be expected in bulk polymer, both for isothermal [63-65] and nonisothermal [6] indentation conditions. For nonisothermal AFM nanoindentation, heat was applied only to the AFM tip while the polymer was

initially at room temperature [6]. For isothermal AFM nanoindentation, the polymer and AFM tip were at identical temperature [63-65]. Isothermal indentations at room temperature found that within 5 nm of the polymer free surface, the polymer modulus was 30 % lower than that of the bulk [64]. Similar experiments also found anisotropy in the film mechanical properties [65]. Isothermal indentations above and below T_g found that the temperature-dependence of the polymer mechanical properties was reduced compared to the bulk [63]. Possible explanations for the observed behaviors included free surface mobility reducing modulus [64] and enhancing wetting [63], strain induced structuring during sample preparation [65], and high localized pressure [63]. Nonisothermal nanoindentation formation showed high frequency polymer viscosity that was independent of chain length, with the requirement that the heater temperature be well above bulk T_g in order to form indents [6]. Simulations accounting for phonon scattering and contact resistance at the polymer-tip interface showed shear rate- and temperature-dependent viscous and elastic polymer response explained the observed behavior [66], yet analytical models showed instantaneous compressive heating could also explain the behavior [67]. Because of the complex polymer mechanical response, heat transfer characteristics, and observed deviation from bulk behavior, there is a lack of understanding of polymer deformation during polymer thin film nanoindentation.

This chapter uses modified continuum simulations to investigate polymer flow during AFM nanoindentation, for both isothermal and nonisothermal conditions. The simulations examine a constant temperature sharp probe tip indenting a 35 nm film of high M_W polymethylmethacrylate (PMMA). Isothermal simulations compare well with experimental results and highlight the importance of bulk shear-thinning material

properties and slip at the polymer-tip interface. Nonisothermal simulations show the importance of high polymer-tip interface temperatures due to steep temperature and viscosity gradients within 50 nm of the polymer-tip interface.

5.2 Simulation Approach

The broad range of time scales and underlying structure of polymer melts, from angstrom level backbone to R_g of tens of nanometers, prohibits any one simulation method from capturing all physical processes [68]. An accurate model of AFM nanoindentation should capture the physics of highly entangled polymers of M_W near 500k on length scales 10 – 100 nm and time scales 1 – 100 nsec. Molecular dynamics methods can track individual atoms but are generally limited to 100 monomer chains and 5 nm computational space with picosecond time steps [68]. Coarse-grained potentials can simulate non-Newtonian [68] and viscoelastic flow [69] with nanosecond time steps and microsecond processes [70] of polymers with M_W > 100k [71] by modeling 10 – 20 monomers as bonded blobs. In AFM nanoindentation, large penetration depths and temperature gradients can confine deformation zones to 5 - 10 nm, limiting coarse-grained solution methods to only 5 – 10 effective monomer blobs in the area of interest. Further, at present coarse-grained methods are appropriate for a limited temperature range [71]. The three dimensional, multiscale heat transfer and polymer deformation in AFM nanoindentation render it beyond reach of atomistic simulations [72]. This work uses continuum simulations with modified boundary conditions to model polymer melts in AFM nanoindentation, where the boundary conditions capture length scale-dependent slip.

The present simulations are performed using *GOMA* [73], a finite element program specialized for analysis of flows having a freely moving surface. *GOMA* has been used for physical problems with length scales from 100 nm to 1 mm for processes such as deformable roll-coating and journal bearing lubrication [74], micropen lithography [75], and embossing imprint lithography [42, 76]. *GOMA* provides two solution techniques to track the moving polymer interface: a front-tracking technique, the Arbitrary Langrangian/Eulerian (ALE) method; and a front-capturing technique, the Level Set (LS) algorithm. ALE separates polymer motion from mesh motion thus allowing large free boundary deformations [36]. LS tracks the liquid interface through a fixed mesh by following a function abstracted from the velocity field [77, 78]. LS may require denser meshes than ALE to avoid mass loss and provide reliable convergence. In this chapter, isothermal AFM nanoindentation simulations use ALE for fast simulation times while nonisothermal AFM nanoindentation simulations use LS to capture the large interfacial deformation at the polymer-tip interface. Both solution methods solve proper boundary conditions and governing equations of Navier-Stokes momentum and continuity:

$$\rho\left(\frac{\partial v}{\partial t}+v\cdot\nabla v\right)=-\nabla p+\nabla\cdot\tau \tag{5.1}$$

$$\nabla\cdot v=0 \tag{5.2}$$

where ρ is the liquid density, v liquid velocity, t time, p isotropic liquid pressure, and τ liquid stress tensor. Boundary conditions differ for isothermal and nonisothermal simulations. For nonisothermal AFM nanoindentation, heat transfer is also coupled into the solution:

$$\frac{\partial(\rho C_p T)}{\partial t} = -v \cdot \nabla(\rho C_p T) - \nabla \cdot q \tag{5.3}$$

where C_p is the heat capacity, T temperature, and q conduction heat flux.

In AFM nanoindentation, two effects govern motion of tip indentation in polymer: slip at the indenter-polymer interface due to size effects when $R_{tip} \sim R_g$ [62], and slip of polymer chains within the polymer. At high strain or shear rates, such as exist in AFM nanoindentation, bulk polymer chains disentangle, resulting in segments of polymer molecules that follow Rouse dynamics [79-82]. Constitutive models for a non-Newtonian stress tensor with adjusted boundary conditions can capture behavior of confined polymer melts. Since $R_{tip} > \xi_o$ and $R_{tip} \sim R_g$, the present simulations model a full-slip polymer-tip boundary. To capture rate-dependent polymer response, an inelastic Carreau shear-thinning material models the polymer. The Carreau material model captures reptation at low shear rates and Rouse dynamics at high shear rates by Newtonian viscosities. Although the inelastic Carreau model cannot properly predict normal stress ratios during polymer flow, the Carreau model can well approximate polymer behavior similar to more advanced viscoelastic models when deformation thinning dominates over normal stresses and relaxation [83]. By applying the Cox-Merz rule [84], the Carreau model combines elastic and viscous effects to match measurements. Material data of 200k M_W PMMA at 190 °C from [39] is fit to the Carreau model with high shear rate Rouse viscosity determined by:

$$\eta_{Rouse} = \frac{\pi}{12}\left(\frac{\rho RT}{M_C}\right)\tau_e \tag{5.4}$$

where η_{Rouse} is the Rouse polymer viscosity in free space, R universal gas constant, T temperature, M_C critical molecular weight for high M_W polymers, and τ_e polymer

relaxation time denoting onset of tube constraint effects [82]. Equation 5.4 is based on $\eta_{Rouse}(M_C)$ and not $\eta_{Rouse}(M_W)$ as appropriate [81, 82, 85] since $\eta_{Rouse}(M_W)$ at high shear rates underestimates measurements of complex viscosity at similar shear rates [39]. Further, rheological measurements at high shear rates have shown the high shear rate Newtonian regime to be independent of M_W [86]. The temperature dependence of the polymer viscosity is accounted for by the Williams-Landel-Ferry (WLF) equation. The Carreau model fits PMMA of various M_W by scaling zero shear viscosity and terminal relaxation or disengagement time τ_d by $(M_W/200k)^{3.4}$. The Carreau model represents a range of polymer deformation mechanisms: zero shear viscosity describes the viscous flow region, power law shear-thinning describes the rubbery plateau region, and high shear rate Rouse viscosity describes the glass-rubber transition region.

5.3 Results and Discussion

The present simulations investigated both isothermal and nonisothermal AFM nanoindentation into a polymer thin film. In the isothermal case, both tip and substrate were heated. In the nonisothermal case, only the AFM tip was heated.

5.3.1 Isothermal AFM Nanoindentation

The isothermal simulations modeled polymer flow in a 35 nm film of 350k M_W PMMA supported by a silicon substrate. The substrate approached a silicon AFM tip of radius 20 nm and spring constant 40 N/m at constant velocity 160 nm/sec. A no-slip polymer-substrate boundary condition modeled the interface between the polymer film and the underlying silicon [87-89]. A full-slip condition modeled the polymer-tip

interface. For swift convergence, the AFM tip was initially embedded 5 nm in the polymer with a no-slip condition. Assuming the AFM tip represents a sphere in Stokes flow, the small contact area of no-slip introduces an error < 10% from full-slip Stokes flow [90]. The goal of the isothermal simulations was to simulate a previously measured situation [63].

Figure 5-1 shows the model and boundary conditions for isothermal AFM nanoindentation. The simulations predicted indentations governed by shear-thinning polymer behavior at temperatures from 115 – 135 °C, where T_g is 120 °C [39]. The indenting AFM tip produced a distribution of shear rates in the polymer, localized near the tip. Figure 5-2a shows viscosity contours in the polymer during indentation where the viscosity was normalized by the Rouse viscosity at the indicated temperature. At 115 °C, the polymer viscosity contours were nearly constant within 100 nm of the tip. At 135 °C, the polymer viscosity contours varied by over an order of magnitude within 25 nm of the tip. The local variation in polymer viscosity only occurred at high temperatures as the Carreau model predicted a shear-rate independent Rouse viscosity at low temperatures but a shear-rate dependent power law viscosity at high temperatures. The polymer shear-thinning induced a mechanical response that was different from a constant viscosity response. Figure 5-2b shows the force on the tip during indentations where the tip velocity was constant and the tip spring constant was set to zero. As temperature increased, the force on the tip decreased due to a logarithmic WLF reduction of viscosity with temperature. The force on the tip however did not follow the logarithmic WLF reduction, due to shear-thinning near the tip.

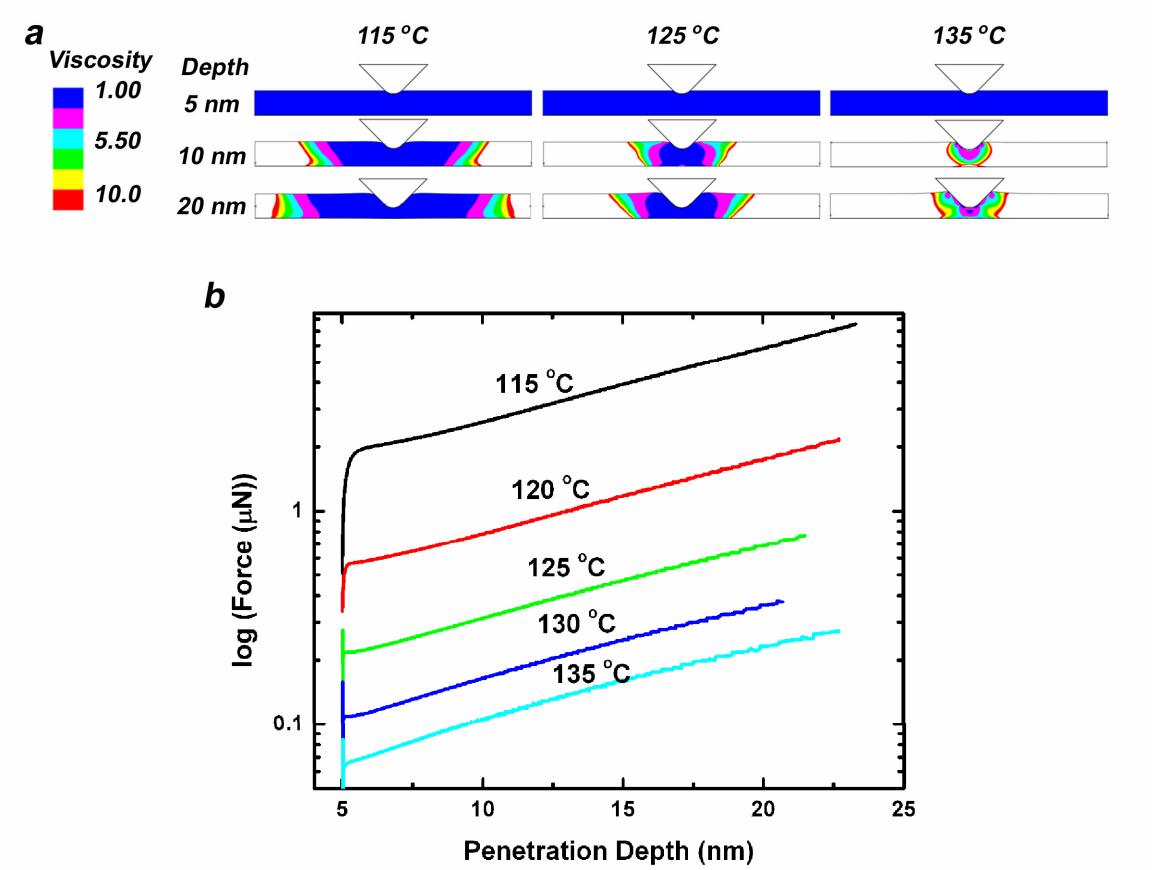

Figure 5-2 Deformation profiles and loading curves for isothermal AFM nanoindentation. a) Indentation profiles showing viscosity contours for isothermal indentation at different temperatures. Dimensionless viscosity of 1.00 corresponds to polymer Rouse viscosity at indicated temperature. Shear rates increase at deeper penetration depth. b) Semi-log loading curves under isothermal conditions. Differences between isothermal loading curves decrease at higher temperatures due to the shear-thinning polymer response. The simulation material model does not properly account for deformation processes below T_g where the simulation predicts material deformation at a constant Newtonian Rouse viscosity.

Simulated force-distance curves matched well with experimental force-distance curves over a range of temperatures. Figure 5-3a shows force-distance curves predicted by simulation and measured force-distance curves at two temperatures, where the measurements were previously published results [63]. At temperatures just above T_g, 122 °C simulation closely matched glassy 100 °C measurements. The unexpected agreement of Carreau simulation to glassy data may have been due to simulated properties different from experimental parameters. In particular, a broad glass transition, rapid quenching

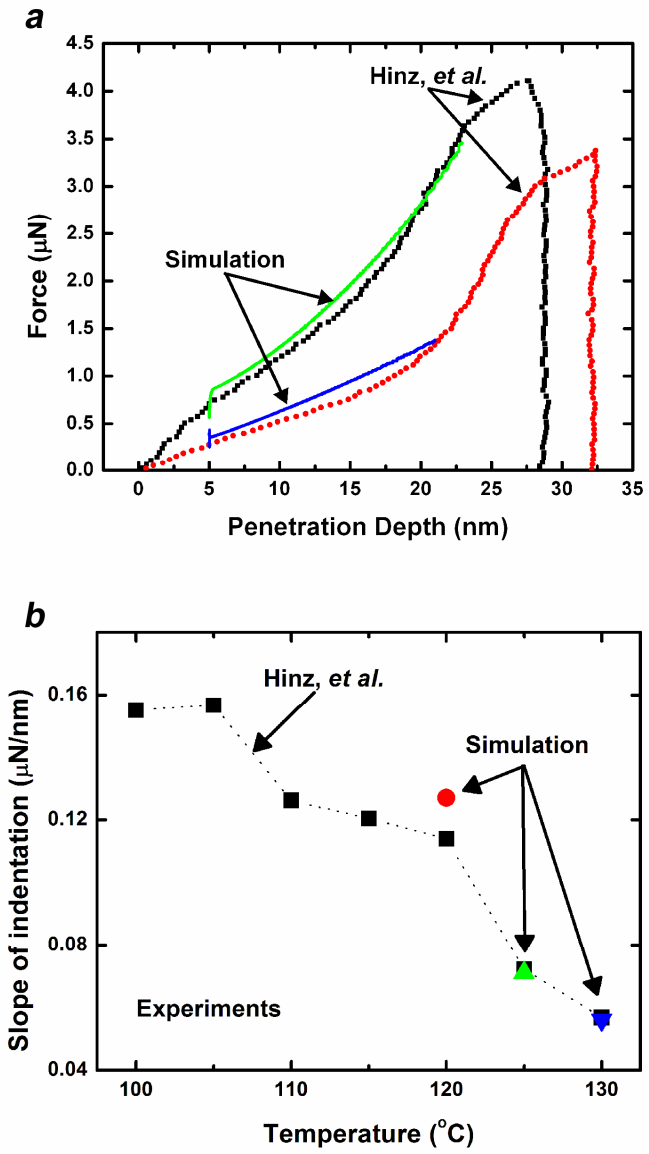

Figure 5-3 Polymer response during isothermal nanoindentation described by bulk high shear rate behavior. a) Force versus depth indentation curves show simulation just above T_g matches glassy polymer indent and simulation at 130 °C matches experiment at 130 °C. b) Simulation initial slope of indentation also closely matches experimental data over the same temperature range. At higher temperatures, the slope of indentation approaches the cantilever spring constant. Experimental measurements graciously provided by Hinz, *et al.* [63].

during film preparation, or a surface layer of enhanced mobility [57] could cause enhanced mechanical compliance near T_g. Simulated and measured force-distance curves matched well at 130 °C while simulation indentation slope at 122, 125, and 130 °C

closely corresponded to measured indentation slope at 120, 125, and 130 °C, respectively [63]. For an elastic contact, the initial slope of indentation can determine the polymer modulus [91]. The agreement of Carreau simulation slope of indentation and measurements, shown in Figure 5-3b, suggests the dominance of viscoelastic shear-thinning over elastic polymer properties during isothermal indentation near T_g. The slope of indentation at $T > 130$ °C approached 40 N/m, limiting measurements and simulation of polymer mechanical properties to $T < 135$ °C due to compliance-coupling of the polymer modulus to the cantilever stiffness.

Comparisons between model and experiment were limited to penetration depths < 20 nm due to simulation constraints of mesh deformation at large strains. At tip penetration depths > 20 nm, the simulation would underestimate polymer force response, as measurements showed a sharp increase in force versus displacement. This stiffening could be due to high shear rate elastic stiffening during squeeze flow [92] or attractive surface interactions between polymer and substrate [57, 87, 88]. At tip penetration depths < 20 nm, potential sources of simulation error could arise from contact conditions. If the polymer-tip interface or polymer-substrate interface were no-slip, the current simulations underestimated the force response by a factor of 1.5 [90] or 30% [93], respectively. The no-slip interfaces would require higher simulation temperatures to match experimental results of [63]. Any errors introduced by contact interaction will be constant across the temperature range, limiting accuracy in fitting proper simulation and measurement temperature but not the precision of the Carreau WLF material behavior.

5.3.2 Nonisothermal AFM Nanoindentation

Figure 5-4a shows the FEM model and boundary conditions for nonisothermal simulations. The conditions were chosen to represent thermomechanical data storage [6]. The polymer was 35 nm 75k M_W PMMA film with isotropic bulk thermal conductivity 0.18 W/m-K and heat capacity 1450 J/K-kg. Beneath the polymer was 80 nm crosslinked epoxy with identical thermal properties as the polymer and a silicon substrate of bulk thermal conductivity 150 W/m-K and heat capacity 700 J/K-kg. Polymer bilayer and silicon substrate boundaries were at 25 °C. The LS simulations required modeling of a small air region with density and viscosity 2 orders of magnitude less than the polymer layer, which are slightly less than bulk values. The air boundary was modeled as adiabatic since the cantilever-substrate air gap equilibrates in ~ 100 nsec and it is known that the heat transfer across this interface is not important for the indent formation [66]. The tip loading force was 30 nN, the radius 30 nm, and the spring constant negligible. The tip was also modeled with a large inertial mass equivalent to the effective mass of a typical cantilever beam, thus providing a lower limit to indentation speed based on the cantilever mechanical time constant [66]. The simulations assumed a no-slip boundary condition at the PMMA-epoxy interface and a full-slip condition at the polymer-tip interface.

Predictions showed polymer deformation localized near the AFM tip. Figure 5-4b shows deformation profiles for polymer-tip interface temperature T_{int} 250 °C. The tip locally heated the polymer, creating a temperature gradient from the tip temperature to 25 °C within 50 nm from the polymer-tip interface. Over this range, the temperature-

dependent complex viscosity varied by several orders of magnitude, resulting in localized deformation of high temperature polymer within 5 – 10 nm of the tip.

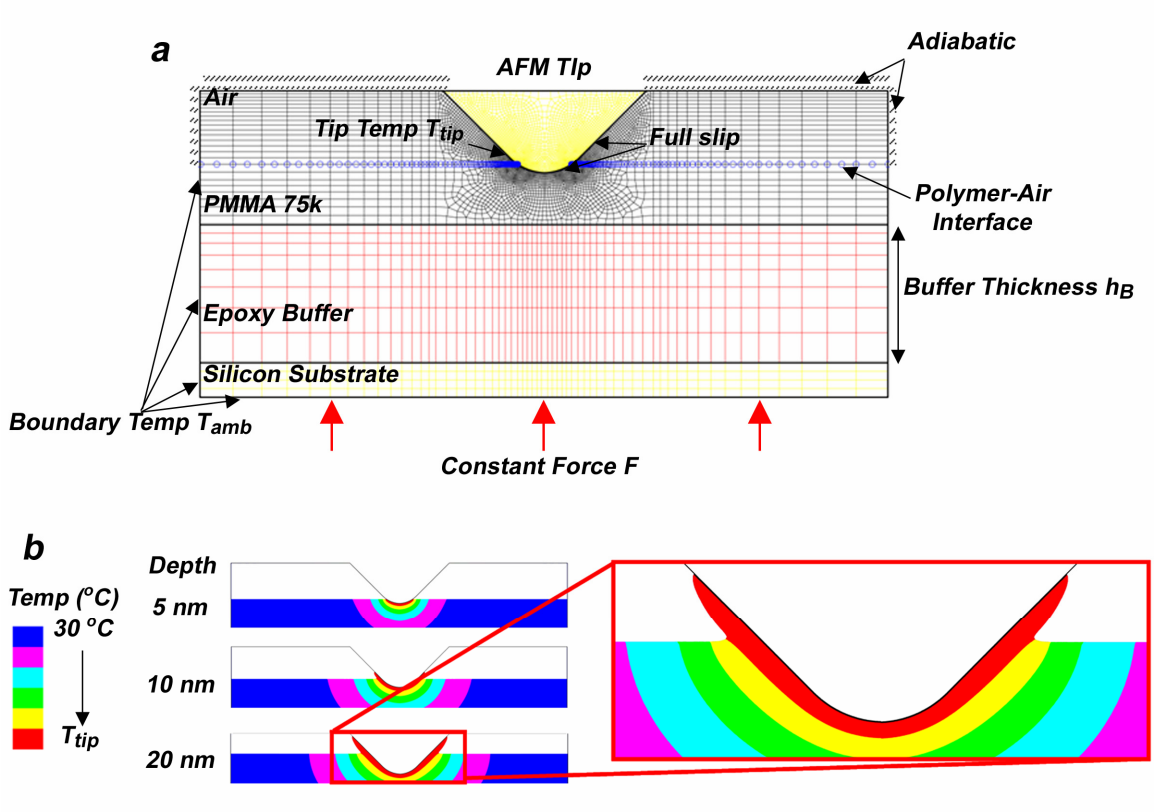

Figure 5-4 Modified continuum simulations guide predictions of nonisothermal nanoindentation. a) Nonisothermal nanoindentation of AFM tip with full slip and constant temperature tip-fluid interface into ambient polymer at constant force. b) Indentation profiles showing temperature contours in 75k M_W PMMA polymer for tip-polymer interface temperature T_{int} = 250 °C and ambient temperature T_{amb} = 30 °C. The steep spatial gradient of the temperature shift factor results in highly localized polymer deformation resembling lubrication. Relaxed shift factor and increased segmental cooperativity lengths in confined geometries would broaden deformation.

Polymer-tip interface temperatures > 200 °C were required for significant penetration depth in 10 μsec for tip pressures < 1 GPa, which corresponds with general experimental observations. Figure 5-5 shows the penetration depth after 10 μsec for AFM tip radius 20 nm at 30 nN, 100 nN, and 500 nN from T_{int} 175 °C – 300 °C. For a given polymer-tip interface temperature, increasing load increased penetration depth. However, at T_{int} < 200 °C, indentation rates were < 0.5 nm/sec regardless of load. The

steep temperature and viscosity gradient within 50 nm from the polymer-tip interface resulted in insufficient polymer softening to form deep indentations when $T_{int} < T_g + 80$ °C.

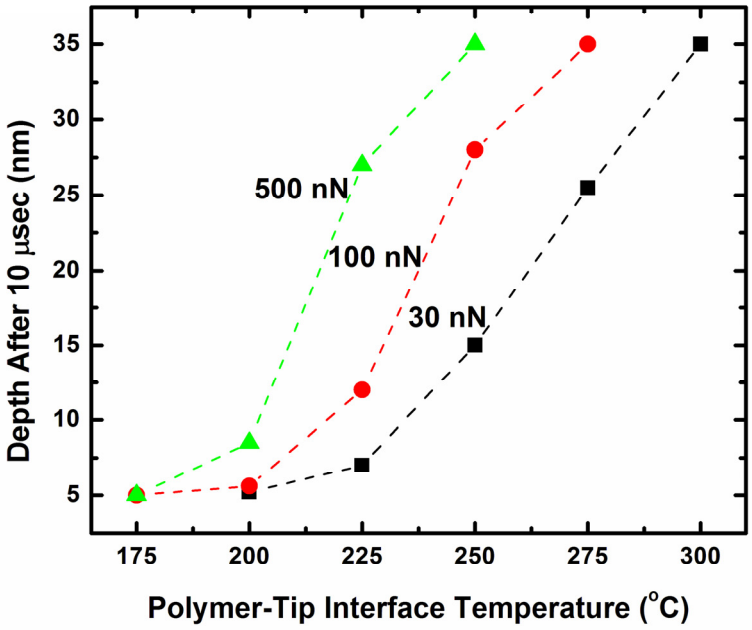

Figure 5-5 a) Required polymer-tip interface temperature for an AFM tip of radius 30 nm to form a data bit in 10 µsec. Forces > 500 nN are required to form 10 nm indentations in 10 µsec at $T_g + 80$ °C. Polymer-tip interface temperatures > 200 °C are required for significant penetration depth in 10 µsec for tip pressures < 1 GPa.

Predictions compare well with measurement, which is reported elsewhere in detail [6] and only summarized here. For the experimental measurements, a heated AFM cantilever with tip radius 30 nm indented a 35 nm film of 600k M_W PMMA supported by 80 nm SU-8 epoxy on a silicon substrate. A 28 nN load pressed the tip against the polymer surface initially at room temperature with negligible penetration. The cantilever was heated to 380 °C, transferring sufficient heat to the AFM tip to allow the tip to indent the polymer. The motion of the AFM tip was measured via laser reflection.

Figure 5-6 shows the data for indentations in 600k M_W PMMA at cantilever heater temperature 380 °C and simulation predictions for indentation into 75k M_W PMMA at T_{int} from 200 °C – 250 °C. Simulations at T_{int} 225 °C and 250 °C suggest T_{int} ~ 240 °C predicts measured material response, in agreement with heat transfer modeling that predicts T_{int} ~ 250 °C for cantilever heater temperatures near 380 °C at 30 nN load [66]. A temperature drop along the tip of about 100 °C is appropriate in light of simulations [66] and measurements [94] of heat flow in the tip.

Simulations were limited to M_W < 75k due to numerical instabilities of the viscosity gradient in the locally deforming polymer. Modeling M_W > 75k would increase T_{int} to match measurements, though the high shear rates and strongly shear-thinning polymer would likely only increase T_{int} by about 25 °C. Hydrostatic pressures due to tip load could also increase simulated T_{int} to match measurements, however 30 nN load would only increase T_g by at most 2 °C [95]. The combined results of enhanced mobility due to the free surface [57] but reduced mobility due to the attractive substrate interface [57, 87, 88] would likely increase T_g and thus T_{int} to match measurements to within 5 °C [88].

Overall, the simulations suggest that logarithmic viscosity gradients caused by temperature gradients in the polymer govern the bit writing process. However, the simulations predict most of the polymer flow in a region of thickness 5 – 10 nm while measured AFM traces after indentation show a broader deformation profile [6]. The shape of the free surface should not greatly influence the simulation mechanical response as viscoelastic effects dominate capillary effects during the indentation timescale. Several physical phenomena not accounted for in simulations would broaden the

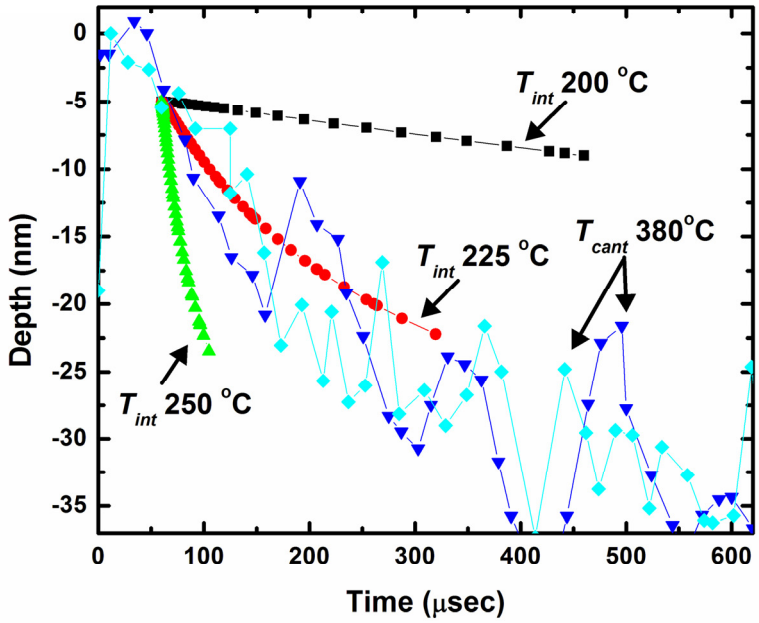

Figure 5-6 Measurements and simulations of nonisothermal AFM nanoindentation for nanoprobe data storage. Simulation of 75k M_W PMMA for tip-polymer interface temperature T_{int} ~ 240 °C matches experiment for indentation into 600k M_W PMMA at cantilever heater temperature of 380 °C. Heat transfer modeling predicts T_{int} ~ 250 °C [18] for similar conditions. Tip radius is 30 nm.

simulated free surface deformation. Enhanced cooperativity of short range elastic modes of polymer mobility [57, 96], reduced temperature dependence of viscosity [59], and anisotropic thermal conductivity [97] have been measured in thin polymer films. These effects would result in larger volumes of similar viscosity material adjacent to the tip and broaden the polymer deformation.

5.4 Conclusion

This chapter uses continuum simulations of polymer flow with modified boundary conditions to predict nanometer-scale polymer deformation. The continuum simulations accurately model sub-continuum polymer mechanical response during AFM

nanoindentation from initial film thickness ~ $2R_g$ to residual film thickness below R_g but highlight the need for nanoscale material property measurements to accurately model deformation shape. High M_W polymer films during isothermal AFM nanoindentation follow shear-thinning bulk material behavior with a full-slip polymer-tip interface, in agreement with predictions of [62]. Nonisothermal AFM nanoindentation simulations show logarithmic viscosity gradients caused by temperature gradients in the polymer govern the bit writing process. The continuum simulations allow for optimization of nanoprobe data storage and high resolution NIL based on bulk viscoelastic material properties and extend continuum descriptions of polymer mechanics to length scales below R_g.

CHAPTER 6

LOCAL TEMPERATURE-CONTROLLED NANOINDENTATION: AN EXPERIMENTAL METHOD TO DIRECTLY MEASURE GLASSY AND VISCOELASTIC NANOMECHANICAL POLYMER PROPERTIES

This chapter presents isothermal local temperature-controlled nanoindentation using focused ion beam milled flat punch molds. This nanomechanical materials testing platform extends the capabilities of nanoindentation into low modulus glassy and viscoelastic materials. The method employs contact geometries with 10:1 aspect ratio of mold diameter to film thickness to enable sensitive surface detection and load resolution. Resistive heaters and thermocouples integrated into the mold and sample permitted independent heating and thermometry. Mold and sample thermocouples were calibrated for isothermal contact conditions by controlling directional heat flux during surface approach. The indentation experiments measured dynamic properties of load, stiffness, and dissipation. Berkovich indentations in silicon and flat punch squeeze flow in polymer thin films with local heating from 20 – 125 °C properly measured dynamic mechanical properties, validating the experimental method. This work extends the temperature range of nanoindentation to 125 °C, with higher temperatures possible.

6.1 Introduction

Accurate values for temperature-dependent mechanical properties of materials that depend on specimen size are essential for engineering design of a wide variety of micro- and nanosystems [98]. Many micro- and nanoscale applications, such as lubrication [55], nanolithography [54], and data storage [6], depend on mechanical properties of thin polymer films that deviate from expected bulk behavior at length scales < 100 nm [56, 99]. Reliable manufacturing of many micro- and nanoscale devices will require characterization of *nanoscale* mechanical properties of polymer films over a wide range of temperatures. This paper presents a materials testing platform for thin polymer films via local temperature-controlled nanoindentation with flat punch molds, enabling measurements of nanoscale polymer properties in confined geometries and extending materials testing capabilities of nanoindentation into low modulus glassy and viscoelastic materials.

Few nanoscale materials testing techniques have directly measured dynamic mechanical properties of polymers over a range of temperatures. Dewetting tests [100-104] in polymer films near 100 nm thickness above and below the polymer glass transition temperature T_g investigated the rate of hole formation as a function of film thickness, molecular weight M_W, temperature T, and thermal history. However, the resulting measurements were difficult to compare with bulk material properties due to coupled effects of friction, internal residual stresses, capillary forces, and viscoelastic and plastic deformations. Modifications to exisiting bulk materials characterization techniques can better control geometry and isolate polymer mechanical properties such as the temperature-dependent modulus. Surface force apparatus (SFA) drainage flow

studies have investigated polymer mechanical properties in thin films of low M_W polymer or melts with low T_g [105-109], but low stiffness mica cylinders limit the ability of SFA to investigate high M_W polymers or highly viscous flows. Atomic force microscope (AFM) nanoindentation is also limited by compliance-coupling of mechanical probe to material modulus, making AFM nanoindentation poorly suited for comprehensive testing of polymers that exhibit large mechanical property variation. While traditional nanoindentation measurements are of sufficient stiffness to probe glassy polymer properties, low load resolution prevents measurements of low modulus polymer and requires indents of lateral and depth dimensions > 1 μm for accurate measurements [110].

Recent modifications to traditional nanoindentation have enabled measurements of nanoscale polymer mechanical properties in both the glassy and viscoelastic state by indenting thin polymer films using molds of controlled flat punch geometry [111]. Contact geometry with 10:1 aspect ratio of mold diameter to sample film thickness resulted in detectable polymer stiffness at temperatures above and below T_g. The modified nanoindentation measurements demonstrated true isothermal contact conditions up to 50 °C by global heating of the entire nanoindentation system. Possible damage to sensitive electronics required operating temperatures were < 80 °C, limiting the library of polymers available for both glassy and viscoelastic characterization.

Nanoindentation using flat punch molds with modifications for elevated temperature control could offer a versatile nanomechanics material testing platform capable of measuring temperature-dependent material properties over a large range of temperatures. A variety of nanoindentation experiments using traditional sharp tip molds have demonstrated elevated-temperature measurements via substrate heating up to 600 °C

and both substrate and mold heating up to 500 °C [112]. However, isothermal temperature control was not expressly demonstrated in either single- or double-side heating. In single-side heated nanoindentation [112, 113], a nanoindenter tip assembly consisting of a diamond tip brazed to a low thermal conductivity shaft was brought into contact with and heated to thermal equilibrium by a heated substrate while the temperature-sensitive transducers were simultaneously convectively cooled. The only thermocouple directly measuring experimental conditions was placed 2 mm adjacent to the sample. Thermal modeling assumed no changes in substrate temperature due to the indenter contact and neglected any modes of convection due to the coupled effects of the heated stage and cooled transducer that could result in nonisothermal contact conditions. In double-side heated nanoindentation, a small heater and miniature thermocouple were attached to the diamond tip for testing of metals and glassy polyimide [114]. No attempts of temperature calibration of independent heating elements were presented, suggesting that temperature mismatch of the indenter tip and sample likely resulted in some amount of heat redistribution on tip-sample contact [112]. Nonisothermal contact conditions will result in sharp gradients in mechanical properties in the contact region [19, 20], making interpretation of measured material response in nonisothermal nanoindentation difficult to impossible.

This chapter presents true isothermal local temperature-controlled instrumented nanoindentation using flat punch molds. The nanoscale materials testing platform is capable of measuring mechanical properties of polymers both above and below T_g with calibrated isothermal operating temperatures up to 125 °C. Nanoindentation molds and samples were instrumented with independent heating and thermometry for open loop

temperature control. Both glassy and viscoelastic polymer nanomechanical properties were measured using 10:1 aspect ratio of mold diameter to sample film thickness. Directional heat flux on surface approach calibrated mold and sample thermocouples for isothermal contact conditions during double-side heating. The instrumented nanoimprint experiments deviate slightly from true squeeze flow and uniaxial compression tests due to pileup of extruded material, but the high fluid pressure between nanoimprint tool and substrate should reduce the influence of edge effects on measured properties. This paper demonstrates measurements of polymer mechanical behavior above and below T_g in a squeeze flow geometry, focusing on thermal instrumentation and characterization of local temperature-controlled nanoindentation.

6.2 Experimental Methods

6.2.1 Room Temperature Instrumented Nanoimprint

Room-temperature instrumented nanoimprint was performed with a commercial nanoindentation system, Nanoindenter XP from MTS Systems, but differed from traditional nanoindentation testing by using flat punch molds representative of nanoimprint tools. Focused ion beam milling shaped defined geometries into silicon, diamond, or iridium molds. The planar geometry molds were aligned to polymer samples to less than 0.1 ° by a dual-axis tilt stage with stepper motor control (Physik Instrumente) as measured by in situ AFM scanning of replications into polymer. Nanoindentation measurements were performed under DC load control with a supplemental AC mode provided by an additional 45 Hz sinusoidal loading that was feedback regulated to provide a constant 2 nm amplitude motion of the mold. Both the amplitude and phase

relative to displacement of the loading signal were recorded. All tests followed an identical 5 segment loading history: 1) Approach surface at 5 nm/sec until 15 ° decrease in phase of oscillatory displacement relative to load determined mold-surface contact. 2) Load at constant load rate to predetermined load or depth. 3) Hold load and measure creep. 4) Unload to 80 % maximum loading. 5) Hold load to allow creep and then continue to hold load to measure thermal drift displacement rate. 6) Unload.

6.2.2 Local Heating Setup

In local temperature-controlled instrumented nanoimprint, separate, independent heaters and thermocouples were attached directly to the imprint molds and substrates. Both Berkovich diamond tip molds and flat punch silicon molds were instrumented with local temperature control. Silicon molds were fabricated by attaching 1 mm diameter polished silicon spheres onto commercial nanoindenter tool mounts (MTS). Spheres were fixed to the mounts with high temperature epoxy (Duralco) by curing at 120 °C for 4 hours then 230 °C for 4 hours. Silicon molds were then mounted in the nanoindenter, brought into contact with a polymer surface, and sheared laterally across the surface to transfer polymer to the mold marking the point of contact. Silicon molds prepared in this manner and factory-mounted Berkovich diamond tip molds purchased from MTS were then ready for local temperature instrumentation.

Thermocouples and surface mount resistive heaters attached directly to silicon and Berkovich tip molds for local temperature control. Figure 6-1 shows a fully-connected local temperature-controlled nanoimprint flat punch silicon mold. Solder of melting temperature > 220 °C (Alpha Fry) connected three 1 kΩ surface mount resistors

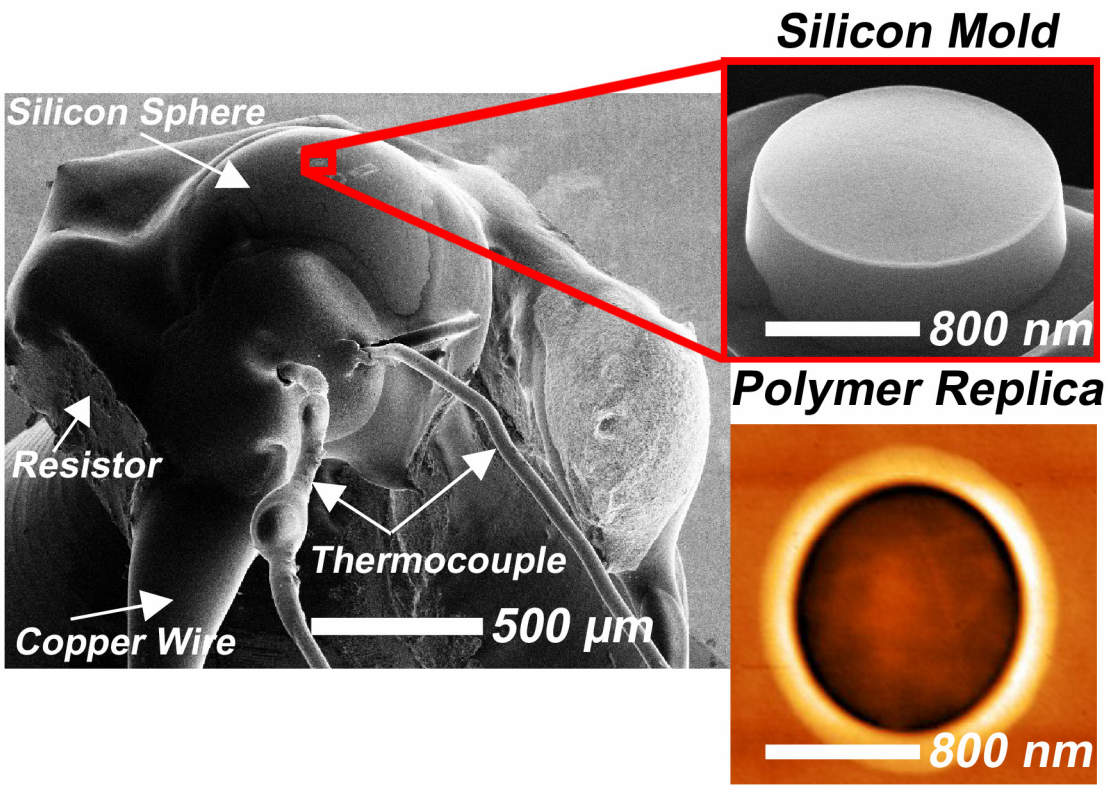

Figure 6-1 Scanning electron micrograph of a silicon instrumented mold. A 1 mm diameter silicon sphere is epoxied to a mount. Three surface mount resistors soldered in series are epoxied to the sphere. Resistors are powered via 100 µm diameter copper wire. A thermocouple of wire diameter 50 µm is epoxied to the sphere. Focused ion beam milling shapes the apex of the sphere into a flat punch mold. An AFM scan shows the silicon flat punch mold replicated in polymer.

(Vishay) in series at right angles forming a 3 kΩ U-shaped resistor. 100 µm diameter copper wire (Goodfellow) was soldered to the U-shaped resistor ends to provide electrical connections. Silicon or Berkovich tip molds then slotted inside the wired U-shaped resistive heater. Thermally conductive epoxy (Electrolube) glued the heater in place below the tip apex and established the heat conduction path from heater to mold after curing at 150 °C for 1.5 hours. A micropositioner stage placed 50 µm wire diameter thermocouple near the mold apex without interfering with the point of contact. The thermocouple was glued to the sphere with thermally conductive epoxy. The thin wire leads of the thermocouple and electrical connections added negligible stiffness to the 80

N/m support springs and negligible mass to the 10 g load shaft, leaving the nanoindenter in a mechanically equivalent state with or without thermal instrumentation. Once instrumented with resistive heater and thermocouple, the molds were focused ion beam milled to control geometry and then ready for use.

For sample side local temperature control, a 2 mm thick thermoelectric heater (RedFish Photonics) was glued with silver paint to a 5 mm thick thermally insulating Macor ceramic disc support fixed to the dual-axis tilt stage. Thermocouple of wire diameter 50 μm was epoxied to the heater stage with thermally conductive epoxy. Samples were glued with silver paint within 2 mm from the thermocouple. The AFM scan in Figure 6-1 shows successful replication of an instrumented silicon flat punch mold in polymer.

6.2.3 Isothermal Contact Calibration

Heat transfer in local temperature-controlled instrumented nanoimprint can be modeled by a one-dimensional point contact with heat loss dominated by spreading resistance at the mold-sample interface. In order to ensure isothermal contact at the sample temperature, the mold temperature T_M *at the point of contact* must be in thermal equilibrium with the sample at the sample temperature T_S. T_M as measured by the mold thermocouple may deviate from the true temperature at the point of contact T_C due to poor thermocouple placement and heat loss along the mold surface. For isothermal contact, T_C must be determined in reference to T_M.

Mold and sample thermocouples were calibrated for isothermal contact by monitoring T_M as the mold approached the surface at T_S. The low thermal mass of the mold in relation to the thermal mass of the sample stage resulted in a sensitive heat flux

dependence on separation distance during a slow surface approach of 5 nm/sec. Figure 6-2a shows T_M normalized by T_M at the time of contact during 5 nm/sec surface approach with 80 °C sample. Sample and mold were heated at 1 °C/min to 80 °C then allowed to

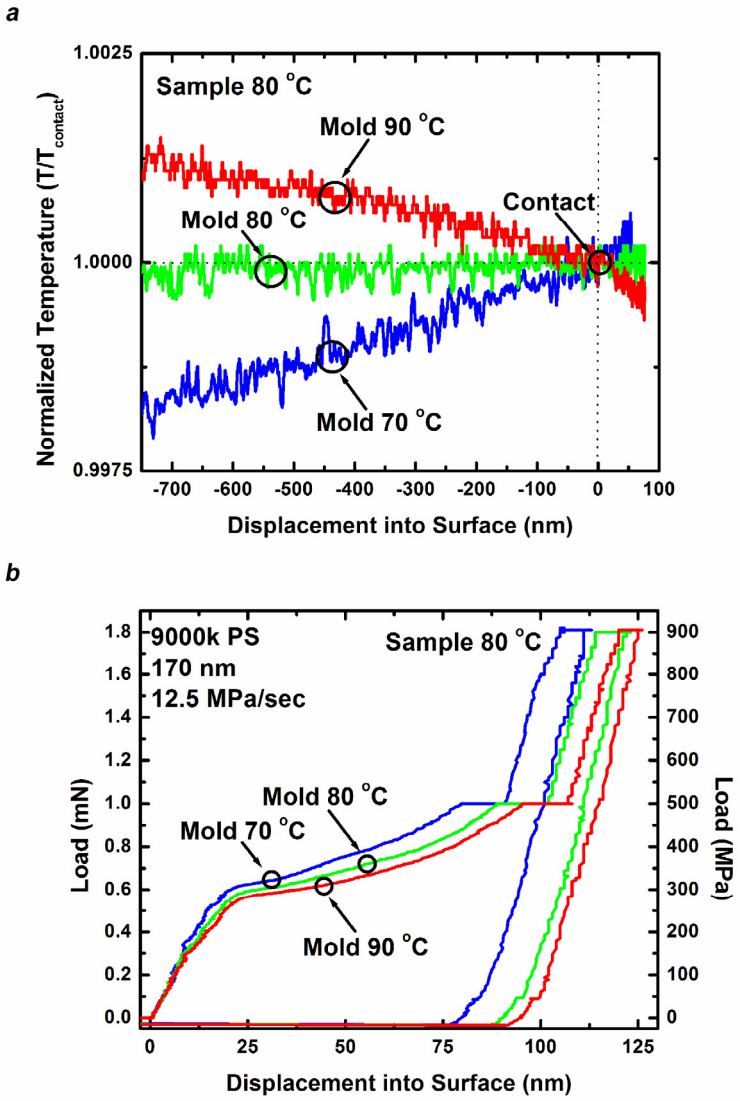

Figure 6-2 Thermocouple temperature calibration. To determine the mold temperature resulting in isothermal contact with the sample stage, independent batch indentation tests are performed sweeping the mold temperature above and below the stage temperature set at 80 °C. (a) The geometry of instrumented imprint displays a sensitive heat flux dependence on separation distance of mold from sample stage. Mold-side heating/cooling occurs when the sample stage is hotter/colder than the mold. Isothermal conditions are determined when the mold temperature does not change when approaching the surface. (b) Load versus displacement curves for squeeze flow polymer testing at stage temperature 80 °C with mold temperature 70 – 90 °C. Flow of heat and associated thermal expansion during nonisothermal conditions impacts measurements.

thermally equilibrate for 3 hours prior to measurements. An additional 30 min thermal equilibration hold time was allowed for each 10 °C mold temperature increment. Thermocouple noise was less than 0.1 °C. Mold heating during surface approach signaled the mold was cooler than the stage while mold cooling during approach signaled the mold was hotter than the stage. Isothermal conditions were determined when the mold temperature remained constant when approaching the surface.

The measurements of directional heat flux to determine contact conditions is reminiscent of thermal dissipation displacement sensing [66] used in AFM-based data storage [6], and could, if calibrated, provide an independent means of mold displacement measurement in nonisothermal cases. In the non-contact region, the temperature varied in a linear manner with sample to mold separation distance, with no change discernable except at very small (<150 nm) separation. This linear function indicated a simple thermal transport mechanism, most likely heat conduction, proportional to separation distance. Below 150 nm, there appeared to be a leveling off of both heating and cooling gradients, which may be related to the mean free path of the air molecules. Upon mechanical contact, much sharper temperature changes were observed for nonisothermal conditions.

Although the exact value of T_C could not be determined with certainty during local temperature-controlled nanoimprint, the steady values of T_M and T_S during measurements indicated isothermal conditions which were likely equal to T_S due to the large thermal mass of the sample stage. In Figure 6-2a, isothermal contact at T_S = 80 °C happened to occur when T_M also measured 80 °C, though $T_M = T_S$ was not necessarily a sufficient condition for isothermal contact due to measured mold temperature depending

on location of thermocouple attachment to the mold. During isothermal contact conditions, T_M was constant to within 0.1 °C as the mold approached the sample from 1000 nm. The slow 5 nm/sec approach and close match of T_M and T_S resulted in minimal heat redistribution on tip-sample contact. Figure 6-2b shows the effect of nonisothermal contact conditions on mechanical measurements of load versus displacement. When the mold was cooler than the stage and absorbed heat during the measurement, thermal expansion of the mold required the nanoindenter control loop to decrease displacement to maintain a given load. Thus nonisothermal measurements with mold heating resulted in measurements that appeared stiffer than isothermal measurements. Similarly, nonisothermal measurements with mold cooling resulted in measurements that appeared softer than isothermal measurements.

It is important to note that the significance of apparent stiffening/softening due to nonisothermal contact becomes vastly amplified near glass transition or phase transition temperatures. Spatial thermal gradients due to non-isothermal contact will result in sharp gradients in mechanical properties in the contact region, alter flow properties [19, 20], and make interpretation of material response difficult to impossible. The method presented here avoids the creation of thermorheological conditions where the thermal flux history at the contact influences the mechanical response.

6.3 Results and Discussion

Local temperature-controlled instrumented nanoimprint measurements were performed in bulk silicon and silicon supported thin polystyrene (PS) films. Mold and sample temperatures were held constant for minimum thermal equilibration times of 30

min per 10 °C of temperature change for each measurement. Slow surface approach at 5 nm/sec ensured isothermal contact conditions. Thermal drift rates in silicon were measured at 80 % maximum loading, while thermal drift rates in polymer were measured at high load under fully elastic conditions after allowing sufficient time for polymer creep to extinguish. Quantifying thermal drift rates is essential to decouple thermal instrument drift from true displacements in local temperature-controlled instrumented nanoimprint.

6.3.1 Indentations in Silicon with Berkovich molds

Indentations into bulk silicon with a locally heated Berkovich diamond mold validated the mechanical testing capability of local temperature-controlled instrumented nanoimprint. All Berkovich indents in silicon followed identical load histories: 1) Approach surface at 5 nm/sec until 15 ° decrease in phase angle of oscillatory displacement to load indicates mold-surface contact. 2) Load at 0.25 mN/sec to 200 nm depth limit. 3) Hold load for 15 sec. 4) Unload at 0.25 mN/sec to 2 mN. 5) Hold load for 30 sec to allow creep then hold load for 30 sec to measure thermal drift displacement rate. 6) Unload at 0.25 mN/sec. Figure 6-3 shows load versus displacement curves and continuous stiffness measurements of modulus versus displacement for isothermal indentation temperatures from 20 to 110 °C. Berkovich indents in silicon showed identical elastic-plastic loading at temperatures from 20 – 110 °C. Due to thermal drift rates up to 0.2 nm/sec during loading times of 30 – 40 sec, depth-limited measurements resulted in different peak loads for indents performed at different temperatures. Thermal drift rates were independent of isothermal temperature conditions and were mostly due to changes in room environment over the time of the experiment. The difference in unloading between indents at 20 and 70 °C and indents from 90 – 110 °C was due to

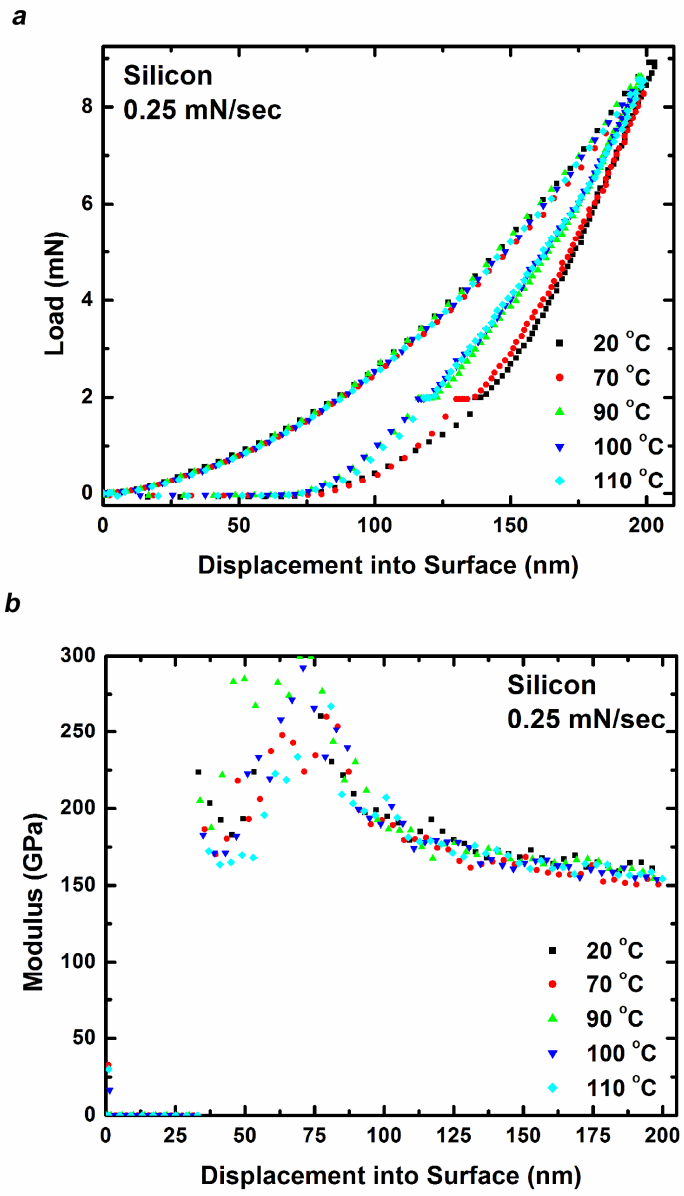

Figure 6-3 Indentations of a Berkovich tip into silicon from 20 – 110 °C. (a) Load versus displacement curves indenting silicon to 200 nm depth loading at 0.25 mN/sec. Indentations from 20 – 110 °C show identical loading behavior. The difference in unloading between indents at 20 °C and indents from 90 – 110 °C is due to influence of thermal drifts during depth-limited loading. (b) Drift-free measurements of silicon modulus approach the bulk value of 150 GPa for indentations from 20 – 110 °C.

unloading from a lower peak load at 90 – 110 °C than at 20 and 70 °C. Although the final depth and thus load were influenced by drift, the load versus displacement curves were identical during loading with local heating up to 110 °C.

Continuous stiffness monitoring provided a drift-independent measure of mechanical properties. Measurements of silicon modulus via continuous stiffness monitoring accurately approached the expected silicon (111) surface modulus value of 150 GPa for indentations from 20 – 110 °C. Measured modulus was independent of temperature for localized heating indents from 20 – 110 °C. Blunting or other nanoscopic defects at the Berkovich tip apex resulted in the overestimation of silicon bulk modulus at depths < 150 nm. The excellent agreement of room temperature Berkovich indents in silicon and Berkovich indents with localized heating demonstrates the ability of local temperature-controlled instrumented nanoimprint to reliably measure dynamical material properties of load, stiffness, and dissipation.

6.3.2 Flat punch squeeze flow measurements in polymer thin films

Local temperature-controlled instrumented nanoimprint allows uniaxial compression and squeeze flow measurements of supported thin polymer films in the glassy and viscoelastic regimes. Focused ion beam milling created smooth flat punch molds of diameter 1600 and 800 nm. PS films were spin cast to 170 nm film thickness. The high aspect ratio of mold diameter to sample film thickness enabled ultra-sensitive surface detection with detectable material modulus for soft polymers in the glassy (GPa) and even viscoelastic (MPa) regime. For molds of diameter > 1 μm, van der Waals attractions and meniscus formation [98] instantaneously pulled the molds into contact with the surface from 10 nm separation when T < 115 °C, resulting in a sharp decrease in phase angle of oscillatory displacement to load signal over a distance < 1 nm. For molds of diameter < 1 μm at all T and molds of diameter > 1 μm at T > 115 °C, the stiffness of the nanoindenter support springs resisted the attractive pull of the surface forces. Under

such conditions, surface detection occured over a distance < 5 nm as the phase angle of oscillatory displacement to load signal quickly decreased by 15 ° near the surface. Local temperature-controlled instrumented nanoimprint measurements followed a standardized approach to ensure isothermal equilibration during loading and unloading and to quantify thermal drift rates for each measurement. For the conditions shown in Figure 6-4 with mold diameter 1700 nm, the measurements followed: 1) Approach surface at 5 nm/sec until phase angle of oscillatory displacement to load signal decreases by 15 ° signaling mold-surface contact. 2) Load at 125 MPa/sec to 500 MPa. 3) Hold load and allow creep for 40 sec. 4) Load at 50 MPa/sec to 800 MPa. 5) Hold load for 20 sec to allow high load creep and then hold load for 20 sec to measure thermal drift displacement rate. 6) Unload at 50 MPa/sec to 50 MPa, hold for 10 sec, then unload at slow load rate of 12.5 MPa/sec to minimize adhesion upon demolding.

Local temperature control modulated material response from glassy deformation with elastic strain, plastic yielding, and post-yield plastic flow, to fully yield-free viscoelastic flow with increasing temperature. The observed temperature dependent material response with local temperature control was identical in character to similar measurements with global temperature control on polymers with a lower T_g [111]. Figure 6-4 shows flat punch squeeze flow measurements with local heating from 20 – 125 °C in 9000k M_W PS films of initial thickness 170 nm. Fully elastic loading occured at 20 °C up to 500 MPa load. Absence of yield during loading to 500 MPa was due to inhibition of secondary molecular motions below the β transition temperature T_β of PS at 50 °C [115]. Increasing T above T_β softened the polymer, enabling yield at lower load than in room temperature indentation. Increasing T above T_g further softened the polymer, unlocking

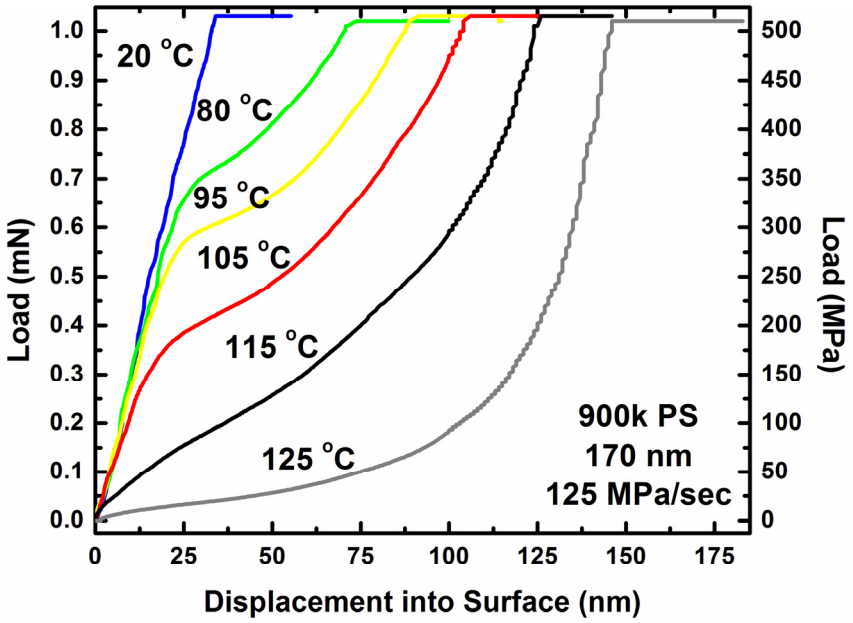

Figure 6-4 Flat punch squeeze flow measurements in polymer with local heating from 20 – 125 °C. Load versus displacement curves show the decrease of yield stress and the transition from elastic deformation to post-yield flow to fully viscoelastic flow with increasing temperature. Polymer response during flat punch squeeze flow measurements with local heating is identical to measurements with global heating.

the α transition and allowing measurements of viscoelastic strains and creep. Continuous stiffness monitoring supplemented load versus displacement measurements over the range of glassy and viscoelastic behavior, recording dynamic in-phase and out-of-phase stiffness for calculation of mechanical moduli. The identical flat punch mechanical signal in the glassy and viscoelastic state for both global [111] and local temperature-controlled instrumented nanoimprint validates the ability of local temperature-controlled instrumented nanoimprint to reliably measure both glassy and viscoelastic nanoscale polymer mechanics.

6.4 Conclusion

This chapter presents material characterization via local temperature-controlled nanoindentation with flat punch molds. This modified nanoindentation materials testing platform is capable of probing a dynamic range of nanoscale glassy and viscoelastic polymer mechanical response under various states of stress and temperature in precisely the same mold-sample system. Focused ion beam milling created flat punch molds with 10:1 aspect ratio of mold diameter to film thickness to ensure detectable material modulus from 1 GPa to 1 MPa. Resistive heaters and thermocouples attached to the mold and sample provided independent heating and thermometry. Calibration of mold and sample thermocouples by directional heat flux on surface approach introduced a novel and convenient means to establish isothermal contact conditions. Berkovich indentations in silicon with local heating from 20 – 110 °C and flat punch squeeze flow in polymer thin films with local heating from 20 – 125 °C properly measured dynamic mechanical properties to validate the experimental method. This work extends the temperature range of nanoindentation to 125 °C, with higher temperatures possible by optimizing resistive heating thermal conduction paths to the mold. Local temperature-controlled nanoindentation, with well-defined contact area and ultra-sensitive surface detection, enables material property characterization of a wide range of materials and temperature-dependent dynamical properties. This technique allows measurements of nanoscale material properties that are directly comparable to measurements of bulk material.

CHAPTER 7

DIRECT MEASUREMENTS OF GLASSY AND VISCOELASTIC POLYMER FLOW IN MOLECULAR-SCALE GAPS

This chapter investigates molecular-scale polymer mechanical deformation during large strain uniaxial compression and squeeze flow measurements of polystyrene (PS) films of thickness near the polymer radius of gyration (R_g). Load-displacement and creep relations were measured during extrusion from initial film thickness 170 nm to residual film thickness 10 nm in PS films of molecular weight (M_W) 9000k, 900k, and 44k, for temperatures (T) from 20 to 125 °C and load rates 12.5 to 1250 MPa/sec. At $T <$ the glass transition temperature (T_g), the polymer glassy response was independent of M_W, as expected from bulk theory. At $T > T_g$, polymer viscoelastic melt response was dependent on the state of polymer entanglements as determined by M_W and initial film thickness. The films of 44k and 900k M_W followed expected bulk response, with 44k M_W showing evidence of enhanced surface-layer mobility, while films of 9000k M_W showed evidence of reduced network entanglements compared to bulk. Loading rate and strain magnitude influenced extrusion depth of high M_W films, with deeper extrusions for loading at high load rates than low load rates. The measurements suggest that for high resolution nanoimprint lithography, mold flash can be reduced for high strain and strain rate loading of high M_W thin films. This unexpected insight could enhance understanding of nanometer-scale mechanical forming processes.

7.1 Introduction

As feature sizes in integrated circuit (IC) fabrication shrink below 20 nm, the demands on resists, masks, and processing equipment may render conventional lithography methods cost prohibitive. Embossing and molding are simple techniques for molecular-scale forming that may overcome challenges to lithography. Studies have shown replication of single walled carbon nanotubes with diameter 2 nm via molding [53] and crack tips of size 0.4 nm via casting [5]. Nanoimprint lithography (NIL) [54] offers scalable molding of sub-10 nm features over large areas [2]. Of the various flow patterns identified in NIL [42, 116, 117], squeeze-like flow has been identified as the most important in governing imprint dynamics for high resolution molding. As IC feature sizes shrink below 20 nm, NIL molding will likely extrude polymer features and residual film thickness to near or below the bulk polymer radius of gyration (R_g). Reliable replication of molecular-scale features will require a fundamental understanding of polymer mechanics at the nanometer scale. This paper investigates molecular-scale polymer mechanical deformation in an approximate squeeze flow geometry during NIL molding of polystyrene (PS) films having thickness near R_g.

The properties of thin polymer films may be different from bulk polymer properties [118, 119]. Recent reviews have highlighted the influence of substrate interaction, stress history, and free surface properties on the glass transition temperature (T_g) and other modes of polymer mobility as film thickness decreases below ~ 100 nm [14, 55]. Confinement of films to thickness < 100 nm resulted in nonuniform T_g profiles across films [57, 58], reduced temperature dependence of viscosity [59], and suppressed particle diffusion [60]. Measurements of the effect of film thickness and molecular

weight (M_W) on T_g of supported and free standing PS thin films are the most common investigations of nanoconfinement effects on mechanical properties [120]. Although there is some disagreement about nanoconfinement effects of M_W on T_g for supported PS films [121], many independent measurements follow the empirical relation developed by ref. [56], which predicts T_g reduction dependent on film thickness and independent of M_W [122]. Measurements of T_g, however, at best provide an indirect measure of chain dynamics, convoluting a time-dependent relaxation function with the temperature dependence of the average relaxation time [120].

Only a few measurements have used a mechanical probe to measure thin film polymer mechanical properties, and the studies have not always agreed, possibly due to differences in measurement method and surface chemistry. Dewetting dynamics studies have investigated supported PS films finding increasing mobility with decreasing film thickness [101] and faster hole growth rates in films of high M_W rather than low M_W [103]. Atomic force microscopy (AFM) measurements of biaxial creep of poly(vinyl acetate) observed rubbery regime stiffening of 26 nm films [123] rather than enhanced mobility. Numerous drainage flow studies with the surface force apparatus (SFA) have emphasized the importance of surface interactions influencing thin film mechanical properties. Polymer squeezed between strongly adsorbing surfaces showed enhanced entanglement interactions beginning at film thickness up to 5 R_g [109] while polymer near non-adsorbing surfaces showed no enhancement of entanglement interactions down to monolayer film thickness independent of M_W [108]. The low stiffness of mica cylinders used in SFA drainage flow studies limits the measurements to either soft films with low M_W or melts with low T_g [105-109].

Compliance-coupling of mechanical probe to polymer modulus has also limited mechanical testing of thin polymer films via nanoindentation. In AFM nanoindentation, the effective compliance of the tested material contact volume must be matched to the cantilever spring: compliant contacts result in no cantilever deflection and thus no load measurement, while stiff contacts allow little relative motion between tip and sample and thus no displacement measurement. Measuring a dynamic range of material properties requires multiple probes that suffer from poorly defined tip contact areas [110]. Traditional nanoindentation testing has been limited in thin polymer films to high modulus glassy measurements due to low load resolution and low polymer compliance [110]. The lack of well-defined polymer nanorheology methods suitable for a wide range of temperatures and materials has resulted in measured thin film properties depending upon mechanical testing method. To better understand polymer mobility modes and effects of spatial confinement on polymer mobility, there is a need for fundamental mechanical property measurements of confined polymer glasses and melts for a range of materials and controlled surface chemistry. Further, translating understanding of nanoscale mechanical properties to optimization of industrial molecular-scale fabrication requires an understanding of nanoscale polymer mechanical behavior in geometries and processing conditions relevant to manufacturing processes such as NIL.

This chapter presents uniaxial compression and squeeze flow measurements of a supported PS thin film using a modified nanoindentation system where the indenter is a flat silicon punch. The experiment features a well defined contact and sufficient material stiffness to probe dynamics of high M_W PS during extrusions from initial film thickness 170 nm at temperatures below and above T_g. This materials testing platform is capable of

probing a dynamic range of material properties while maintaining self-consistent measurements simply by modulating temperature. Temperature-controlled instrumented nanoimprint enables direct measurements of nanoscale polymer properties in confined geometries.

7.2 Experimental Methods

Temperature-controlled instrumented nanoimprint experiments measured polymer mechanical behavior above and below T_g in a squeeze flow geometry with 10:1 indenter diameter to initial film thickness aspect ratio. Figure 7-1 shows the experimental setup. Indenter and substrates were each instrumented with separate, independent heating and thermometry. The PS film had M_W = 9000k, 900k, or 44k with bulk T_g = 100 °C and R_g = 84 nm, 26 nm, and 6 nm, respectively.

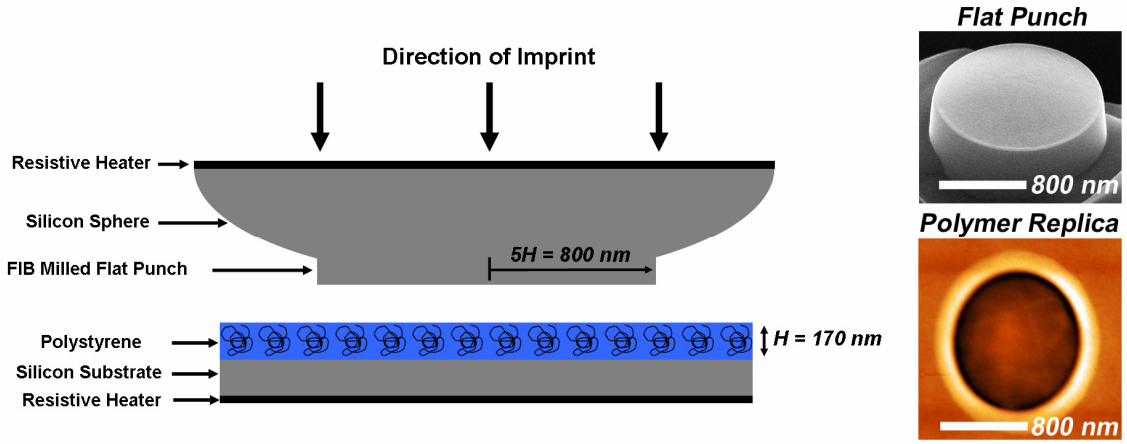

Figure 7-1 Illustration of squeeze flow nanomolding experiment with SEM of flat punch mold and AFM scan of replication in polymer. A flat punch mold indents a thin film of spin cast polystyrene supported by a silicon substrate. A silicon sphere is focus ion beam milled to control contact geometry. The nanoimprint mold and substrate are each instrumented with independent heating and thermometry.

7.2.1 Polymer Sample Preparation

Polystyrene was chosen as a representative amorphous polymer standard with well described film thickness dependence of T_g and non-adhering surface interactions with native silicon oxide surfaces [56, 122]. Three narrow M_W distributions of PS were investigated with two highly entangled polymeric systems and one system just above the critical entanglement molecular weight M_C of 35k [124]. 9000k M_W PS with polydispersity index (PDI) 1.22 was purchased from Polymer Source and 900k M_W PS with PDI 1.10 and 44k M_W PS with PDI 1.07 were purchased from Scientific Polymer.

Thin films were prepared by spin casting dilute solutions of PS in toluene onto lithographic grade polished silicon wafers to thickness 170 nm. Wafers were initially cleaned by sequential acetone, methanol, and DI water rinse followed by 20 min dehydration bake at 120 °C. PS samples were annealed at 150 °C for 120 min to remove spin cast induced internal stresses [125] with heating and cooling ramps < 5 °C/min holding temperature for 15 min every 25 °C increment. PS samples were aged for 5 months at 20 °C prior to testing and showed no signs of large scale dewetting. A Woollam M-2000 ellipsometer measured the resulting film thickness with standard deviation < 5.0 nm.

7.2.2 Temperature-Controlled Instrumented Nanoimprint Setup

A commercial nanoindentation system, Nanoindenter XP from MTS Systems, embossed the polymer films. Details of the modifications to the nanoindentation system for temperature-controlled instrumented nanoimprint are described elsewhere [126] and only briefly summarized here. Focused ion beam milling shaped the 1 mm diameter

polished single crystal silicon sphere nanoindenter tool into a flat punch of height 550 ± 100 nm and diameter 1600 ± 50 nm. Surface mount resistors and a thermocouple were epoxied to the silicon sphere. Silicon supported PS samples were fixed to a thermoelectric heater and a thermocouple was epoxied 2 mm from the PS samples. The heater was glued to thermally insulating ceramic fixed to a tilt stage. All PS samples were aligned to the flat punch silicon molds to less than 0.1 ° as measured by in situ AFM scanning of flat punch replications into polymer. Thermocouples were calibrated for isothermal conditions at 80 °C. The temperature-controlled instrumented nanoimprint measurements were performed at temperatures from 20 – 125 °C. The measurements deviate slightly from true squeeze flow and uniaxial compression tests due to edge constraint of surrounding film, but the high fluid pressure between nanoimprint tool and substrate reduces the influence of edge effects on measured properties.

7.2.3 Molding Measurements

Measurements were performed under DC load control. A supplemental AC mode provided an additional 45 Hz sinusoidal loading that was feedback regulated to provide a constant 2 nm vertical amplitude oscillation. Both the amplitude and phase relative to displacement of the loading signal were recorded. The oscillatory load enabled sensitive surface detection to within 5 nm, as well as dynamic stiffness measurement. All tests followed an identical 5 segment loading history: 1) Detect surface and load at constant load rate to predetermined load or depth. 2) Hold load and allow creep for 40-50 sec. 3) Load at 50 MPa/sec to 800 MPa. 4) Hold load for 20-25 sec to allow high load creep to cease and then hold load for 20-25 sec to measure thermal drift displacement rate. 5) Unload at 50 MPa/sec to 50 MPa, hold for 10 sec, then unload at slow load rate of 12.5

MPa/sec to minimize adhesion upon demolding. Here, load refers to measured force divided by flat punch contact area. Over 2 decades of load rates were tested between 12.5 MPa/sec and 1250 MPa/sec. Three identical tests were recorded for each loading condition at virgin sample locations precisely spaced by 7 μm.

After room temperature alignment and testing, PS samples were heated at 1 °C/min and held at 80 °C overnight for temperature equilibration. Mold and stage thermocouples were calibrated at 80 °C by sweeping the power applied to the nanoimprint mold resistors until the temperature of the nanoimprint mold approaching the PS stage did not change, indicating isothermal conditions at the stage temperature. Measurements were recorded at temperatures up to 125 °C after heating at 1 °C/min and holding the desired temperature for 30 min per 5 °C heating increment to allow thermal equilibration. Thermal drift displacement rates were < 0.25 nm/sec for all temperatures.

The influence of sample preparation on glassy properties was tested by recording measurements in the glassy state after controlled heating and cooling above T_g. Minimal changes in mechanical response before and after heating above T_g indicated only slight influence of physical aging due to sample preparation. Molds were cleaned for 15 min with oxygen plasma before testing pristine PS samples. The oxygen plasma slightly etched the molds, rounding the mold edges after multiple cleanings. Measurements on identical materials before and after multiple cleanings showed no discernible change in mechanical signal.

Figure 7-2 shows representative temperature-controlled instrumented nanoimprint data illustrating the range of measurements recorded. Figure 7-2a shows load versus displacement curves for loading at 125 MPa/sec up to 500 MPa followed by 40 sec creep

at test temperatures from 20 °C to 125 °C. Figure 7-2b shows load versus displacement curves at 120 °C for loading at load rates from 12.5 MPa/sec to 1250 MPa/sec.

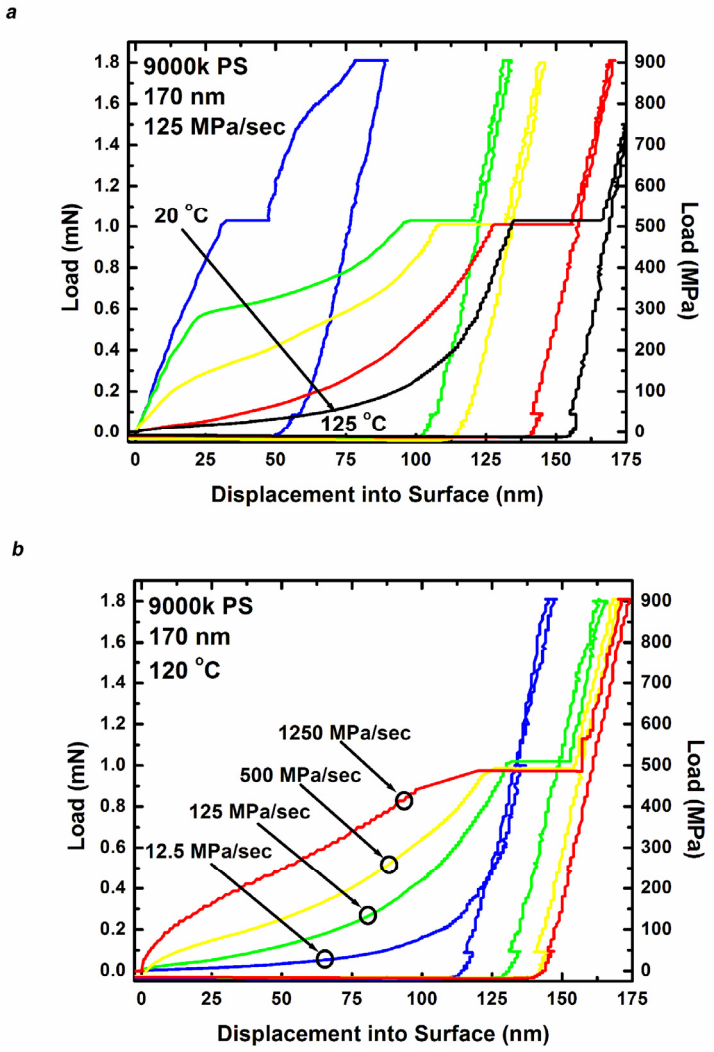

Figure 7-2 Load versus displacement curves molding 9000k M_W PS at 170 nm film thickness illustrating the range of measurements recorded. (a) Load-controlled measurements recorded at isothermal temperatures from 20 °C to 125 °C: load at 125 MPa/sec to 500 MPa, hold for 40 sec to measure creep, load at 50 MPa/sec to 900 MPa, hold for 40 sec to measure thermal drift rates, unload. (b) Two decades of load rates were investigated. Load rate can modulate material response from fully yielded viscoelastic flow at low load rates to glassy behavior with post yield flow at high load rates.

7.3 Results

The experiments investigated polymer mechanical properties under processing conditions relevant to NIL during large strain extrusion from initial film thickness 170 nm to residual film thickness approaching 10 nm. Squeeze flow measurements probed the effect of absolute film thickness in relation to polymer R_g and M_W on glassy and viscoelastic mechanical response.

7.3.1 Glassy Mechanical Response at $T < T_g$

Nanoimprint measurements in 170 nm entangled PS showed identical glassy mechanical properties independent of M_W. Figure 7-3a shows load versus displacement curves loading at 125 MPa/sec to 500 MPa at 20 °C, 80 °C, 95 °C, and 105 °C for films of M_W = 9000k, 900k, and 44k. All three samples showed identical elastic loading, yield stress, and post-yield plastic flow. Fully elastic loading without yield occurred in all PS films at 20 °C up to 500 MPa load. Increasing temperature softened the polymer, allowing yield to occur at lower load than at room temperature. All of the films yielded at the same indentation depth with identical post-yield strain hardening deformation. Films with $M_W < M_C$ could show different post-yield mechanical response due to the absence of chain entanglements. Figure 7-3b shows glassy mechanical response of the entangled amorphous films was identical over 2 decades of load rate and at $T > T_g$ for deformation rates fast enough to induce glassy mechanical response. Yield stress increased with increasing load rates and decreased with increasing temperature. Fully elastic loading with no yield occurred at 80 °C when loading at 1250 MPa/sec to 500 MPa.

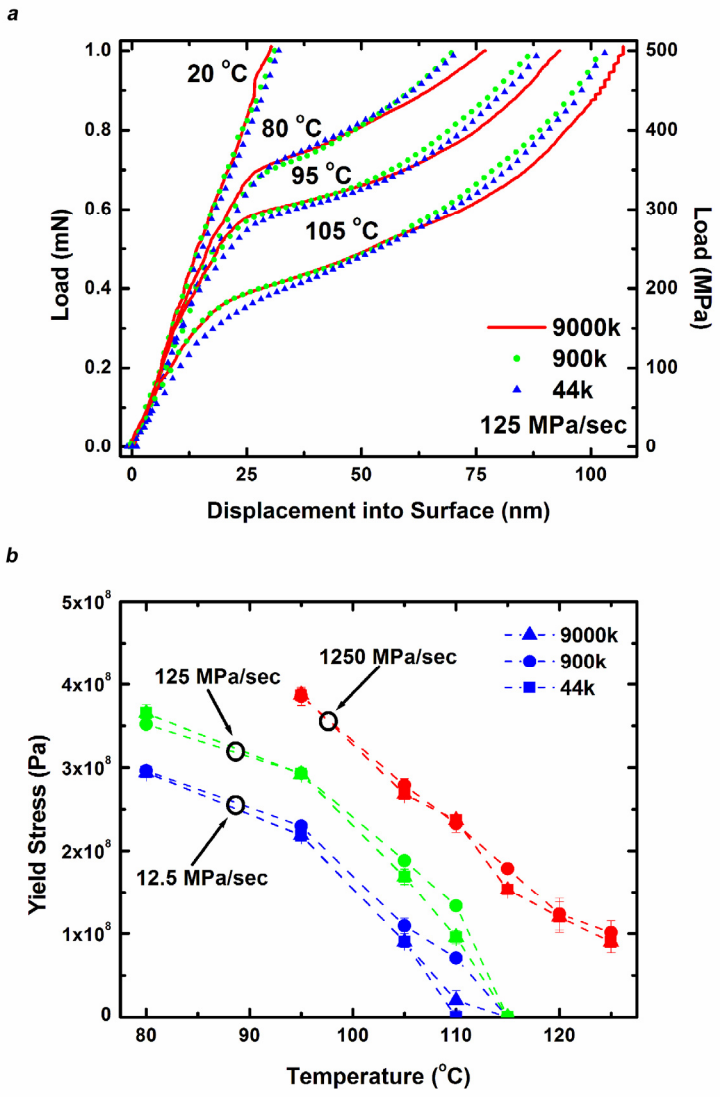

Figure 7-3 Glassy behavior for 9000k, 900k, and 44k M_W PS at 170 nm film thickness. (a) Load versus displacement curves loading at 125 MPa/sec to 500 MPa from 20 °C to 105 °C. All 3 M_W PS exhibit nearly identical glassy behavior during loading. (b) Yield stress measurements loading at load rates from 12.5 MPa/sec to 1250 MPa/sec and temperatures from 20 °C to 125 °C. All 3 M_W PS exhibit nearly identical yield stress during glass material response at all load rates and temperatures. Above 105 °C, 44k M_W PS exhibits a sharper transition from glassy to viscoelastic behavior than 9000k and 900k M_W PS as illustrated by the fully yielded behavior in 44k M_W PS at 110 °C loading at 12.5 MPa/sec.

7.3.2 Viscoelastic Mechanical Response at $T > T_g$

At $T > T_g$, the mechanical response of the viscoelastic melts was a function of molecular weight. All three M_W films showed qualitatively similar viscoelastic mechanical response, though for a given loading condition, 44k M_W extruded to thinner

residual thickness than the higher M_W films. Figure 7-4 shows chain length dependent viscoelastic behavior for the three M_W films at 115 °C following the expected trend of increasing viscosity with increasing M_W.

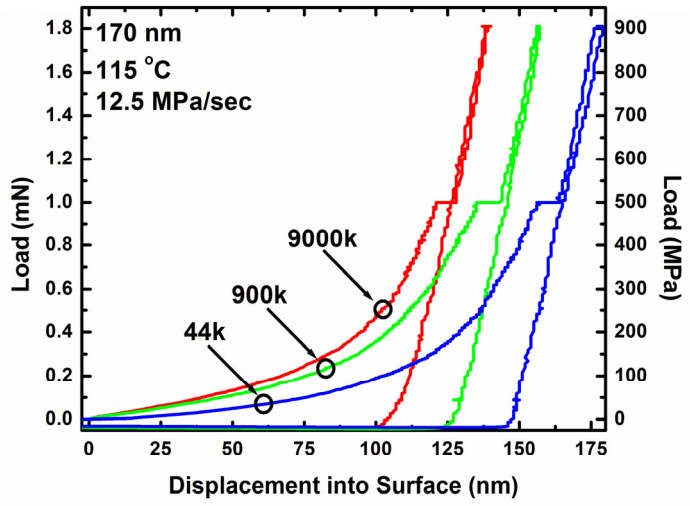

Figure 7-4 Chain length dependent viscoelastic behavior for 9000k, 900k, and 44k M_W PS at 115 °C. 44k M_W PS extrudes to thinner residual film thickness than 900k M_W PS which extrudes to thinner residual film thickness than 9000k M_W PS.

Viscoelastic melt mechanical response was a function of both loading conditions and M_W. Residual film thickness of 9000k and 900k M_W was dependent on load rate, with high load rates resulting in thinner residual film thickness than low load rates. Residual film thickness of 44k M_W PS was independent of load rate and strain magnitude. Figure 7-5a,b shows load versus displacement curves for the 44k and 9000k M_W films at 120 °C during loading to 500 MPa with load rates ranging from 12.5 MPa/sec to 1250 MPa/sec. In the 44k M_W film, residual film thickness after 50 sec creep at 500 MPa was nearly constant regardless of load rate. In the 9000k M_W film, increasing load rate from 12.5 MPa/sec to 125 or 1250 MPa/sec decreased residual film thickness by 30 %. Films

of 900k M_W behaved similarly to films of 9000k M_W. Load rate alone did not modulate indentation depth, however, as strain magnitude coupled with load rate to determine residual film thickness after imprint. Figure 7-5c,d shows creep curves for the 9000k film, holding load constant at 250 MPa and 50 MPa, respectively, after loading at load rates from 12.5 MPa/sec to 1250 MPa/sec. Solid lines in Figure 7-5 represent experimental measurements and dotted lines represent power law creep curve fits at constant load with no-slip boundary conditions. Load rate modulated residual film thickness during creep at 250 MPa while residual film thickness was independent of load rate during creep at 50 MPa.

For small strain loading at $T > T_g$, the observed creep flow of 170 nm films extruded to residual film thickness near 10 nm can be accurately described by bulk viscoelastic melt theory. Figure 7-6 shows creep measurements at constant load for films of M_W = 44k or 9000k after loading at 125 MPa/sec to initial depth 40 nm for temperatures from 105 °C to 125 °C. Solid lines in Figure 7-6 represent experimental measurements and dotted lines represent least squares curve fits for Newtonian or power law fluid creep under constant load. The oscillations in creep measurements at 120 °C and 125 °C were instrumentation artifacts due to dynamic damping of the superimposed harmonic load. Simple Newtonian and power law fluids with no-slip boundary conditions best fit squeeze flow creep measurements for 44k and 9000k M_W, respectively, as full-slip boundary conditions did not properly capture the steep change in film thickness during the initial stages of creep. In Figure 7-6a, no-slip Newtonian curve fits compared well with measurements on 44k M_W films during extrusions down to 10 nm film thickness. Figure 7-6b shows the best fit temperature-dependent Newtonian

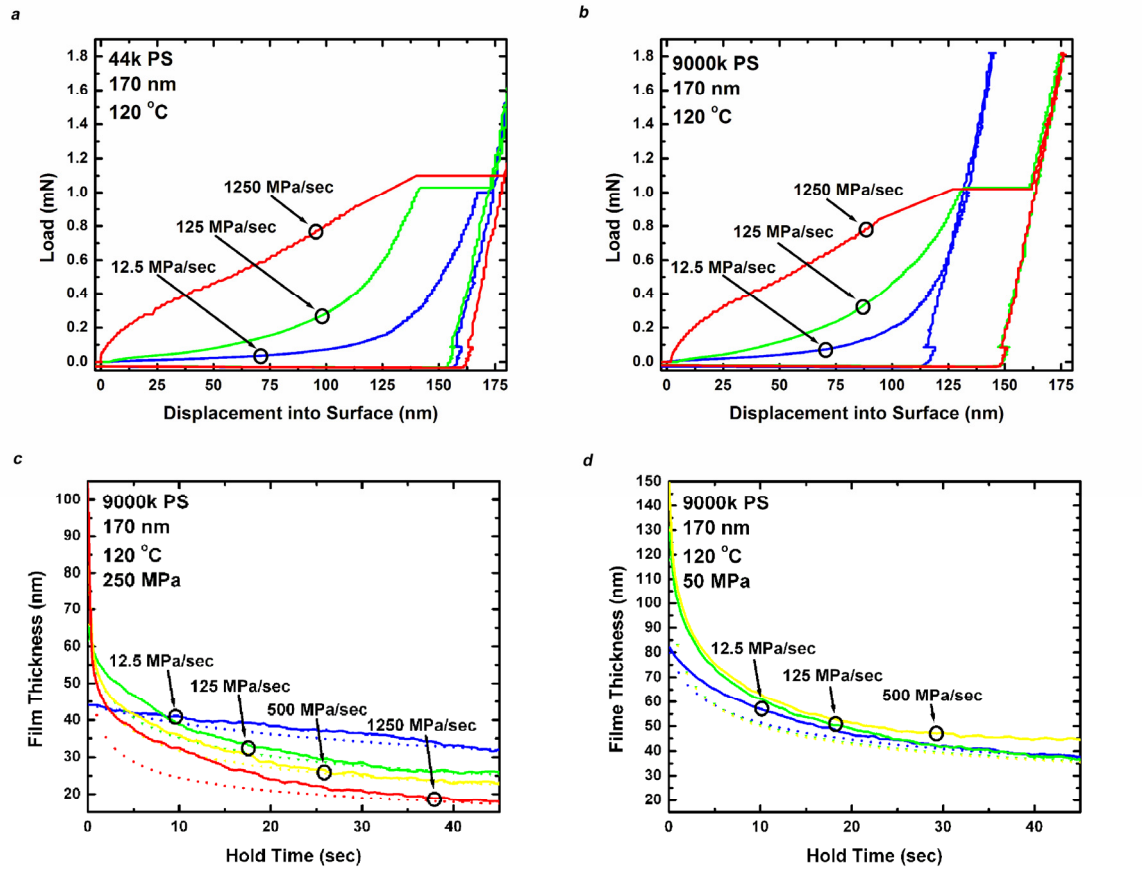

Figure 7-5 Viscoelastic behavior for 9000k and 44k M_W PS at 170 nm film thickness and temperatures from 105 °C to 125 °C. 900k M_W PS behaves similarly to 9000k M_W PS. (a) Load versus displacement curves in 44k M_W PS at 120 °C loading to 500 MPa at rates from 12.5 MPa/sec to 1250 MPa/sec. Final creep depth is independent of load rate. (b) Load versus displacement curves in 9000k M_W PS at 120 °C loading to 500 MPa at rates from 12.5 MPa/sec to 1250 MPa/sec. Final creep depth after loading at 125 and 1250 MPa/sec is greater than final creep depth after loading at 12.5 MPa/sec. (c) Creep curves in 9000k M_W PS at 120 °C after loading to 250 MPa at rates from 12.5 MPa/sec to 1250 MPa/sec. Final creep depth depends on load rate during load. The solid lines represent measurements while the dotted lines are no-slip power law fluid curve fits. (d) Creep curves in 9000k M_W PS at 120 °C after loading to 50 MPa at rates from 12.5 MPa/sec to 500 MPa/sec. Load rate does not influence final creep depth for creep at 50 MPa. Large strains and high load rates modify the entanglement network in high M_W polymer increasing segment mobility resulting in thin residual film thickness following creep.

viscosity for 44k M_W PS to creep curves in Figure 7-6a along with predictions of bulk viscoelastic melt theory. The theoretical curve is the Williams-Landel-Ferry (WLF) fit to 58k M_W PS measurements of [127] scaled by M_W ratio to the 3.4 power. Experimental viscosity versus temperature curves from 110 °C to 125 °C had nearly identical slope as

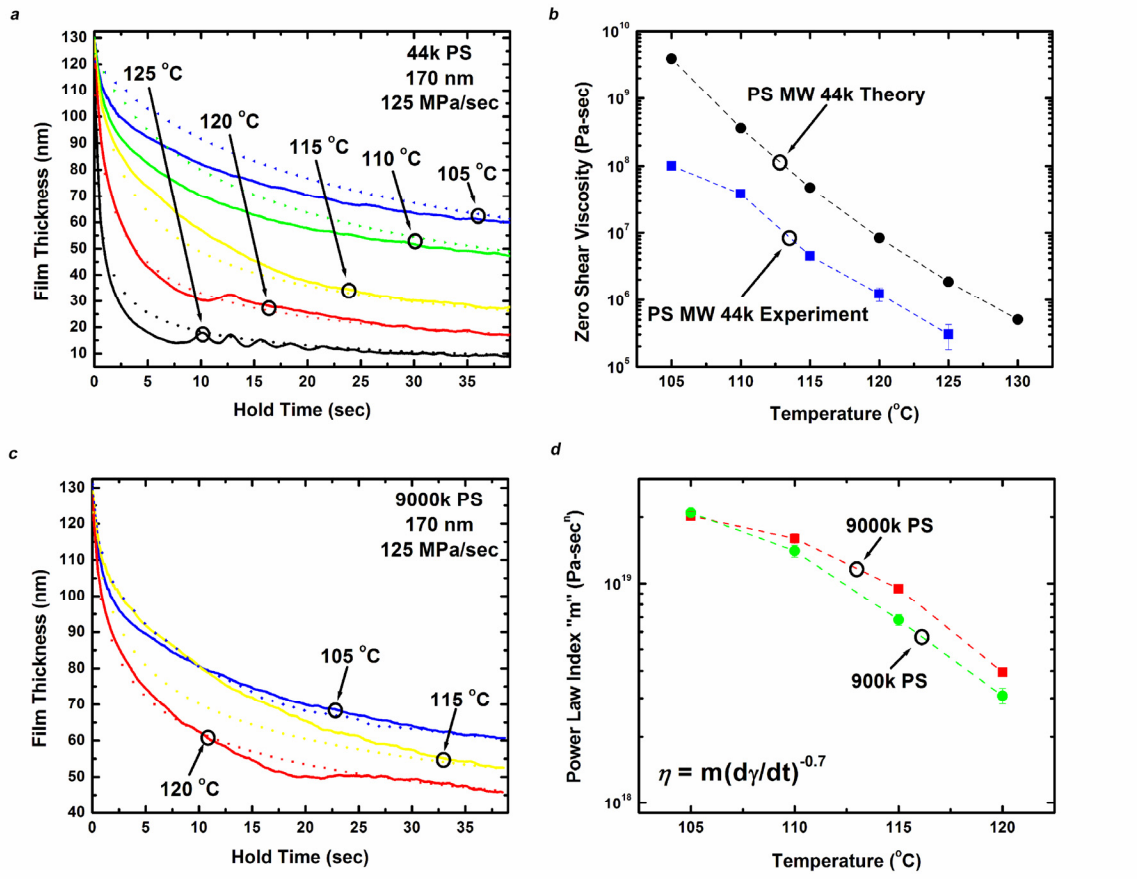

Figure 7-6 Bulk viscoelastic theory with no slip boundary conditions predicts creep response of 9000k, 900k, and 44k M_W PS after small strain loading. The solid lines represent measurements while the dotted lines are no-slip curve fits. (a) Creep measurements in 44k M_W PS and corresponding Newtonian fluid curve fits with no slip boundary conditions. Oscillations in experimental curves are instrumental artifacts due to damping of superimposed harmonic load. (b) Best fit Newtonian viscosity for 44k M_W PS as a function of temperature and corresponding WLF theoretical zero shear viscosity. Experiment shows a constant 5 °C offset from WLF theory likely attributable to heterogeneous polymer dynamical properties across the film thickness. (c) Creep measurements in 9000k M_W PS and corresponding power law fluid curve fits with power law exponent 0.3 and no slip boundary conditions. Creep measurements in 900k M_W PS (not shown) are also well fit by a power law fluid with power law exponent 0.3 and no slip boundary conditions. (d) Best fit power law index for 9000k and 900k M_W PS as a function of temperature. Power law index shows a decrease with increasing temperature and a slight increase with increasing M_W.

theory, though experimental viscosity values were shifted to lower temperatures by a constant 5 °C horizontal offset from the WLF theoretical values.

In Figure 7-6c, no-slip power law fluid curve fits well matched 9000k M_W films during extrusions down to 45 nm residual film thickness. Similarly, no-slip power law predictions compare well to measurements in 900k M_W during extrusions to 40 nm

residual film thickness. Power law curves were best fit assuming a shear-thinning exponent of 0.3, in agreement with squeeze flow measurements of PS in bulk [128]. Figure 7-6d shows the best fit temperature-dependent power law index *m* for 9000k and 900k M_W PS, where $\eta = m\dot{\gamma}^{n-1}$ with η the shear rate dependent viscosity, $\dot{\gamma}$ the shear rate, and *n* the shear-thinning exponent. The power law index showed a decrease with increasing temperature and a slight increase with increasing M_W. Similar values of power law index were also obtained for creep curves beginning from an initial indentation depth of 80 nm.

To compare the best fit power law fluid models for creep of 900k and 9000k M_W films to viscoelastic melt theory, squeeze flow measurements were analyzed in a manner similar to evaluation of capillary rheology measurements [129, 130]. Quasi-steady state viscosities can be obtained from squeeze flow measurements by analyzing shear-rate dependent flow at the outer radius of the flat punch nanoimprint mold. The shear rate at the flat punch rim $\dot{\gamma}_{WR}$ is

$$\dot{\gamma}_{WR} = \frac{R(-\dot{H})}{H^2}\left(2+\frac{1}{n}\right) \tag{7.1}$$

where *R* is the flat punch radius, $\dot{H}$ the flat punch velocity, *H* the film thickness, and the shear-thinning exponent *n* is assigned the value 0.3. The shear stress at the flat punch rim τ_{WR} is

$$\tau_{WR} = (n+3)\frac{HF}{2\pi R^3} \tag{7.2}$$

While the procedure of [129] allows the shear-thinning exponent to vary with shear rate and fits the exponent to measurements, here the exponent was fixed to allow comparisons with bulk theory.

Figure 7-7 shows apparent viscosity $\eta = \tau_{WR} / \dot{\gamma}_{WR}$ versus shear rate $\dot{\gamma}_{WR}$ for nanoimprint creep in 900k and 9000k M_W at $T > T_g$. Solid lines in Figure 7-7 represent power law fluids fit to experimental measurements and dotted lines represent theoretical WLF Carreau fluids of shear-thinning exponent 0.3 and zero infinite shear rate viscosity. The predictions were based on measurements from [127] scaled by M_W ratio to the 3.4 power. For the range of shear rates tested, the no-slip power law fluid response of 900k M_W agreed in magnitude but not slope to theoretical predictions of a shear-thinning Carreau fluid. The no-slip power law fluid response of the 9000k M_W film was similar to that of the 900k M_W film. Both materials displayed similar slopes of experimental viscosity versus shear rate indicating a similar state of viscoelastic melt flow. The magnitude of 9000k M_W experimental viscosity versus shear rate did not agree with theoretical predictions of a shear-thinning Carreau fluid.

7.4 Discussion

Glassy and viscoelastic polymer mechanical properties measured here during squeeze flow extrusions in entangled PS systems mostly agree with bulk viscoelastic response. During glassy loading, the films possess identical glassy mechanical properties as would be predicted by continuum mechanics. During viscoelastic melt loading, the films of 900k and 44k M_W follow bulk viscoelastic trends while films of 9000k M_W exhibit more compliance than continuum theory would predict.

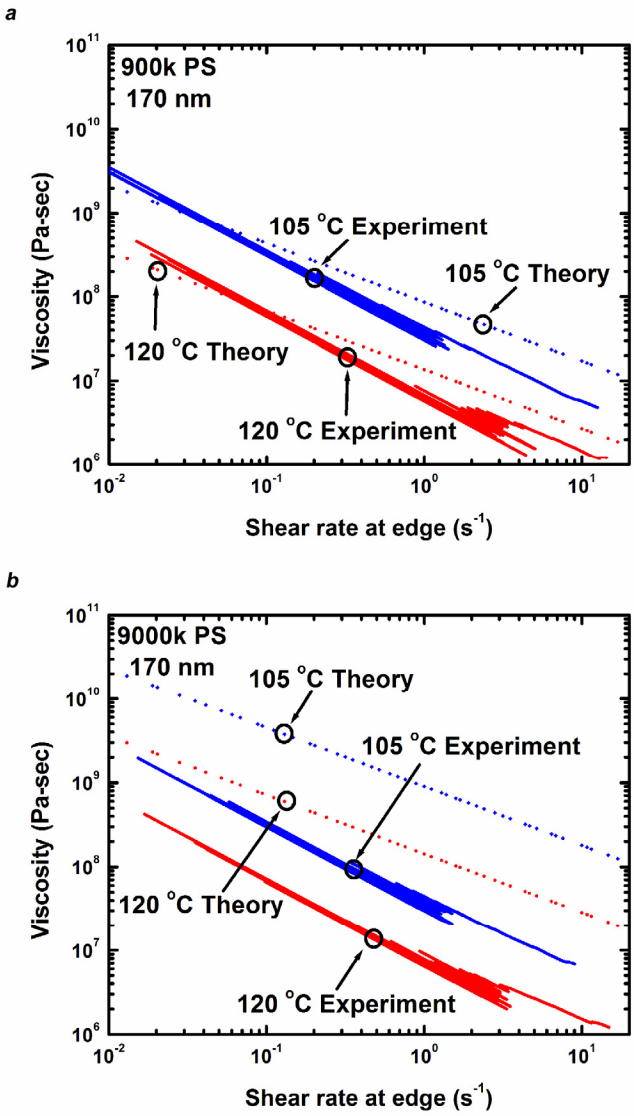

Figure 7-7 Squeeze flow nanorheology of power law fluid with no-slip boundary conditions evaluated at the rim of the flat punch mold. (a) Viscosity versus shear rate data of best fit power law index with exponent 0.3 for 900k M_W PS and theoretical Carreau shear thinning viscosity model with power law exponent 0.3. Experimental measurements of viscosity agree with theory in magnitude but not slope. (b) Viscosity versus shear rate data of best fit power law index with exponent 0.3 for 9000k M_W PS and theoretical Carreau shear thinning viscosity model with power law exponent 0.3. Theory overpredicts experimental measurements, suggesting relaxed scaling from $M_W^{3.4}$ due to reduction of entanglements and network constraints in two-dimensional polymer melts.

Similar to experiments in bulk glassy PS [115, 131], the glassy thin film measurements of this paper result in bulk polymer mechanical properties that are independent of M_W and spatial confinement from initial film thickness 170 nm down to

~50 nm residual film thickness. In bulk polymer, deformations in the glassy state perturb segments of polymer chain less than the entanglement spacing or tube diameter, which is ~5 nm in entangled PS systems. Deformations during elastic loading result from short range molecular motions [132] while deformations during yielding and post-yield plastic flow result in cooperative molecular motions associated with glass-rubber α transitions on the length scale of one tube diameter or smaller [115, 133, 134]. For the thin films measured here, elastic loading, yield stress, and post-yield plastic flow properties are identical for extrusions from initial film thickness 170 nm down to ~50 nm or residual film thickness of 0.6 R_g, 1.9 R_g, and 8.3 R_g for films of M_W = 9000k, 900k, and 44k, respectively.

Similar to bulk viscoelastic melt theory, the thin film viscoelastic melt mechanical properties measured here are dependent on M_W, as conformational changes of extended polymer chain segments are unlocked at $T > T_g$. Short chain 44k M_W PS with M_W just above M_C = 35k behaves as a simple WLF temperature dependent no-slip Newtonian fluid during extrusions from 170 to 10 nm or 1.5 R_g film thickness. However, the experimentally determined zero shear viscosity for a given temperature is lower than bulk WLF theory predicts, with the measured viscosity curve shifted horizontally by 5 °C from the theoretical viscosity curve. The offset between measured viscosity and WLF theoretical viscosity remains constant at 5 °C from 110 °C to 125 °C, indicating final extrusion depth, even down to 10 nm, does not influence measured viscosity. The offset in temperature is not likely due to miscalibration of the true contact temperature, as the measured viscosity values would indicate a contact temperature 5 °C higher, not lower, than measurements. Conversely, measurements at 105 °C still exhibit yield at low load

rates for all M_W PS, and the measured viscosity in 44k M_W at 105 °C deviated from the theoretical WLF trend due to the viscoelastic nature of deformations near T_g. These observations at 105 °C indicate that temperature miscalibration would likely be in the direction of lower temperatures. The offset also could suggest a sample T_g closer to 95 °C than the expected 100 °C bulk T_g, but T_g nanoconfinement effects in thin films of supported PS films do not occur until film thickness is < 100 nm [56].

The 5 °C offset of measured viscosity from bulk theory could also arise from enhanced surface layer mobility [57, 58]. The T_g of a 15 nm PS surface layer atop a 140 nm PS middle layer and 15 nm PS substrate layer deviates from bulk T_g by -32 °C while the 140 nm PS underlayer and 15 nm PS substrate layer maintain bulk T_g [57]. A simple 2-layer weighted average of T_g by layer thickness would predict a 2.5 °C drop in T_g. Although no confinement effect on T_g [122] or elastic modulus [135] is expected at film thickness 170 nm, at $T > T_g$, the enhanced surface layer mobility could result in a reduced effective film compliance from bulk to cause the observed deviation of measured viscosity from bulk theory. Taking into account the depth-independent constant 5 °C offset, zero shear viscosity measurements compare well to bulk theory down to residual film thickness 10 nm.

Films of 900k M_W PS behave as a temperature dependent no-slip power law fluid during extrusions from 170 to 40 nm or 1.5 R_g film thickness. Measured shear rate dependent viscosity of 900k M_W PS can be predicted from bulk theory by a shear-thinning Carreau fluid with WLF temperature dependence. The no-slip power law fluid response of 900k M_W PS agrees in magnitude to theoretical predictions of a shear-thinning Carreau fluid though the slope of the experimental viscosity versus shear rate

curve deviates from the slope of the theoretical Carreau fluid. The different slope between theory and experiment is likely due to variation of the power law exponent with shear rate [129, 130] and influence of elasticity at large extrusion depths.

Films of 9000k M_W PS behave surprisingly similar to 900k M_W PS as a temperature dependent no-slip power law fluid. The shear rate dependent viscosity of 9000k M_W differs only slightly in magnitude from and agrees in slope with that of 900k M_W during creep measurements extruding to 45 nm or 0.5 R_g film thickness of 9000k M_W. Measured shear rate dependent viscosity of 9000k M_W does not agree with theoretical predictions of a shear-thinning Carreau fluid in magnitude or slope over the range of experimentally observed shear rates. The relaxation time constant in the Carreau shear-thinning model scales by M_W ratio to the 3.4 power, shifting theoretical 9000k M_W viscosities to higher values at a given shear rate than theoretical 900k M_W viscosities. The absence of bulk M_W scaling in viscosity measurements of 9000k M_W implies a reduction of network constraints and entanglements from bulk. Recent measurements of PS films with R_g of similar size to initial film thickness H found that thin free standing films are more compliant than thick films [136] and supported films of high M_W show faster hole growth rates than low M_W films [103]. Squeeze flow nanoimprint measurements of this work suggest 170 nm or 2 R_g films of 9000k M_W represent a two-dimensional polymer melt composed of non-ideal segregated polymer chains, where intermolecular interactions and chain overlap are reduced relative to intramolecular interactions [118, 136, 137]. The self consistent measurements for all M_W thin films of this chapter, during extrusions to residual film thicknesses from 10 – 60 nm at temperatures from 105 to 125 °C, suggest the initial state of the film thickness, rather

than the extruded film thickness, governs polymer mechanical properties during squeezing.

For both two- and three-dimensional entangled polymer melts, large strain deformations at high load rates can reduce the residual film thickness of high M_W materials during squeeze flow. High strain rate loading at $T > T_g$ can force polymer melts to respond in an elastic mode, deforming network constraints and entanglement orientation rather than freely moving polymer. For highly entangled systems, the deformation occurs at time scales well below full chain diffusion time constants, as structural reorganization governed by full chain diffusion scales with $M_W^{3.4}$ at $T > T_g$. Large strain loading $\geq$ 125 MPa/sec was fast enough to change the mechanics of extrusions in highly entangled 9000k and 900k M_W but not in slightly entangled 44k M_W. The change in mechanics results from elastic deformation aligning the entanglement network, possibly due to slip at the polymer-silicon interface and thus a state of biaxial extensional flow. Segmental alignment could also result from yield processes, as molecular dynamics simulations suggest [138]. Holding load for creep after aligning network constraints allows polymer relaxations to occur in a state of enhanced flow properties. For low M_W samples such as 44k M_W, the short polymer chains quickly relax and dissipate any elastic stresses of network strain built in during loading. Thus ultimate residual film thickness following creep after loading is independent of load rate for short chain polymers.

7.5 Conclusion

This chapter investigates molecular-scale polymer mechanical deformation during large strain squeeze flow processing conditions relevant to NIL. Instrumented nanoimprint experiments probed the effect of polymer R_g and M_W on glassy and viscoelastic melt mechanical response, extruding PS films from initial thickness 170 nm to residual film thickness 10 nm. Load-displacement and creep relations were measured in 9000k, 900k, and 44k M_W PS over temperatures ranging from 20 to 125 °C and load rates 12.5 to 1250 MPa/sec.

The measurements showed the structure of the initial film thickness determines the state of polymer entanglements, allowing bulk polymer mechanics to predict polymer flow during extrusions down to 10 nm residual film thickness. Thin films of 44k M_W PS showed evidence of enhanced surface-layer mobility while films of 9000k M_W PS showed evidence of reduced network entanglements from bulk. During large strain extrusions of high M_W polymer melts, high load rates resulted in thinner residual films than low load rates. The measurements suggest a counterintuitive approach to reducing mold flash in high resolution NIL: high strain and strain rate loading of high M_W thin films.

With well-defined contact area and surface interactions, nanoimprint squeeze flow can investigate polymer physics from length scales near the polymer tube diameter to well above the polymer coil radius. Reliable materials testing of thin polymer films could assist the engineering of nanostructured materials and processes.

CHAPTER 8

LARGE STRAIN NANOSCALE POLYMER PROCESSING FLOWS

Large strain polymer deformation is present in many manufacturing processes but is poorly understood at the nanometer scale. We present evidence that dimensional scaling violations occur in driven, large strain polymer flows related to mechanical nanostructure fabrication. Polystyrene thin films behaved unexpectedly during uniaxial compression and squeeze flow, for film thickness 36 – 170 nm and molecular weight (M_W) 44k – 9000k. Measurements probed elasticity, yield, and post-yield plasticity below the glass transition temperature (T_g) and viscoelasticity above T_g. Our key observation is that short range elastic molecular motions depend strongly on film thickness and only slightly dependent on M_W, whereas long range plastic and viscoelastic molecular motions depend strongly on both film thickness and M_W.

8.1 Introduction

Perhaps the most widely used manufacturing processes are those that employ large strain polymer deformation. A deep understanding of polymer rheology is required to predict the polymer response during these processes, which include forging, extrusion, and molding. While it is well known that polymer properties may be significantly different at the nanometer scale compared to bulk [14, 55], there is very little understanding of large strain polymer flow at the nanometer scale. This lack of

understanding limits the development of manufacturing processes that exploit nanometer-scale polymer flow [6, 54].

Polymer behavior near surfaces and in confined systems remains a central challenge in condensed matter physics. The observed glass transition in confined polymer systems can be different from that in the bulk, as measured in nanometer-sized pores [99] or films [56, 139]. In general, confinement effects are important below about 100 nm [14, 140], suggesting the existence of polymer mobility [141] and segmental cooperation [142] not observed in bulk materials. Mechanical property measurements can provide insight into molecular-scale polymer behavior [143]. Bending beam [144], buckling [135], biaxial extension [123], tensile stretching [136], and uniaxial stretching [145] measurements of ultrathin polymer films have shown either reduced [136, 144], enhanced [123], or identical [135] mechanical modulus compared to bulk samples, with the result depending on material composition and experimental method. A major obstacle to producing consistent measurements of nanometer-scale polymer mechanical behavior has been the lack of experiments that probe polymer properties over a broad range of spatial and temporal scales within a single experimental system. Furthermore, nearly every measurement of nanometer-scale polymer properties has not measured an industrially relevant flow process and thus does not provide the insight required to guide nanostructure formation.

This chapter presents large strain measurements of thin polymer film compliance at the 10-200 nm scale. The experiments identify distinct scale-dependent mechanical properties resulting from molecular motions associated with elastic strain, yield, post-yield plastic flow, and fully-yielded viscoelastic melt flow. We introduce a self-

consistent testing approach that systematically subjects a given polymer film to a wide variety of thermomechanical load conditions. This measurement provides a unique ability to distinguish scale-dependent mobility modes that provide insight into the dependence of glass transition on length scale and M_W.

8.2 Experimental Methods

Figure 8-1a shows the experiment in which a modified nanoindenter using load control performed finely aligned, isothermal embossing of a thin layer of supported polymer. The indenter and polymer sample were each fixed with independent heating and thermometry, enabling detection of true isothermal contact conditions. The indenter was a flat punch silicon mold shaped by focused ion beam milling to diameter ten times the initial film thickness, providing geometrically self-similar extrusion of silicon supported thin PS films of thickness 36, 80, and 170 nm. The experiments deviate slightly from true squeeze flow and uniaxial compression tests due to asymmetric contact and pileup of extruded material, but the high fluid pressure between nanoimprint tool and substrate should reduce the influence of edge effects on measured properties.

Three narrow M_W distributions were investigated: 9000k, 900k, and 44k M_W PS with bulk T_g = 100 °C and radius of gyration (R_g) = 84 nm, 26 nm, and 6 nm, respectively. All samples were above the bulk entanglement threshold M_W of 35k [124]. Thin films were prepared by spin casting dilute solutions of 0.4 – 2.5 wt. % PS in toluene onto clean silicon wafers. Figure 8-1b shows a 330 nm diameter silicon mold and corresponding replication into 36 nm 9000k M_W PS after room temperature extrusion. Figure 8-1c shows a typical family of load versus displacement measurements from 20 –

125 °C, here from a 1600 nm diameter mold extruding 9000k M_W PS from initial film thickness 170 nm. Load was applied at a controlled load rate up to 1.0 mN (500 MPa) and then held constant to measure creep. After creep, load was applied up to 1.8 mN (900 MPa) to measure thermal drift displacement rates (0.1 nm/s typical) before unloading. An extremely sensitive AC surface detect method ensured the dimensional integrity of the experiment even for highly softened films at high temperature. Further details on sample preparation and experimental methods are available in Chapters 6 and 7.

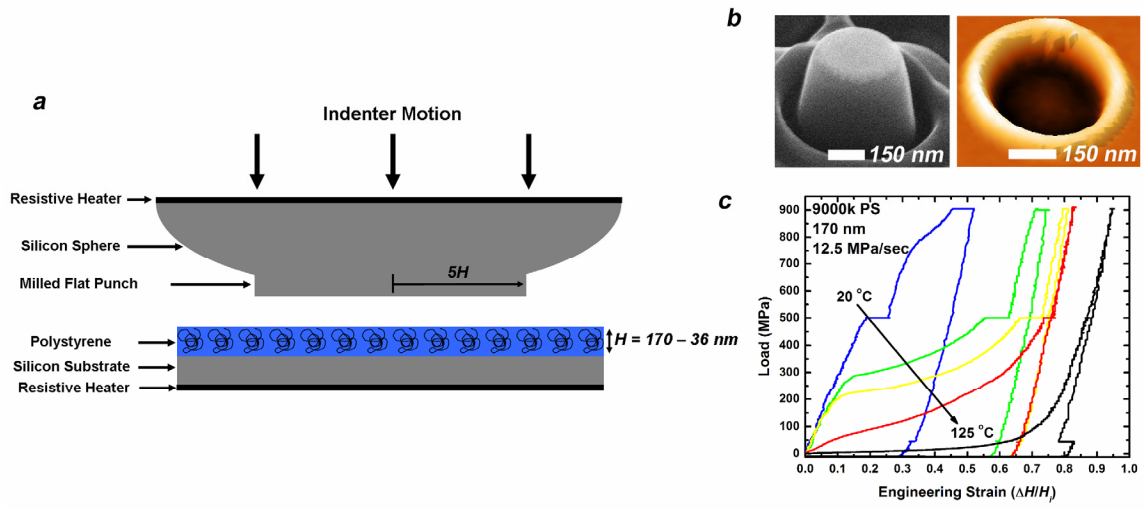

Figure 8-1 (a) Illustration of the experiment. Flat punch silicon molds with 10:1 aspect ratio of mold diameter to initial film thickness emboss thin PS films supported by silicon. (b) SEM viewgraph of the instrumented silicon mold showing a close-up of the smallest diameter molds tested. An AFM scan shows corresponding replication in 36 nm 9000k M_W PS. (c) Load versus strain measurements recorded at 170 nm film thickness above and below T_g.

8.3 Results and Discussion

It is expected that short range molecular motions contribute to elastic response [132, 140], cooperative molecular motions on the length scale of one tube diameter or smaller contribute to yielding and post-yield plastic flow [115, 133, 134, 146, 147], and

conformational changes of extended chain sequences contribute to viscoelastic melt flow above the α transition temperature T_α [124]. Here for nanoscale polymer films we find that small strain, elastic molecular motions depend strongly on film thickness and are only slightly dependent on M_W, whereas large strain, plastic and viscoelastic molecular motions depend strongly on both film thickness and M_W.

Initial film thickness affects glassy mechanical properties of polymer in unconfined conditions, i.e. when R_g is less than the initial film thickness. Figure 8-2a presents measurements of stress (load divided by mold contact area) versus engineering strain (indentation depth divided by initial film thickness) in 44k M_W PS from initial film thickness 170 nm (28 R_g) – 36 nm (6 R_g). The 80 nm film was of 9000k M_W PS. The 170 and 80 nm films showed nearly identical glassy response, while the 36 nm film showed reduced modulus (initial slope of stress vs. strain) and yield stress (stress at intersection of elastic and plastic slope) than the thicker films. At 20 °C, 170 and 80 nm films did not yield during loading to 500 MPa while 36 nm films yielded near strain 0.2 and load 260 ± 50 MPa and exhibited post-yield plastic flow. However, at 80 °C, 170 and 80 nm films yielded at 280 ± 25 MPa while 36 nm films yielded at 210 ± 30 MPa.

Figure 8-2b summarizes the small strain glassy (20 and 80 °C) nanomechanical properties measured in 44k, 900k, and 9000k M_W films from initial film thickness 36, 80, and 170 nm. For all of the PS films tested, elastic modulus and yield stress depended strongly on initial film thickness below 80 nm, regardless of M_W. At film thickness 36 nm, both elastic modulus and yield stress were reduced 25 – 60 % compared to bulk for samples of all M_W. Films of 9000k M_W at 36 nm had slightly lower modulus and yield compared to films lower M_W. The small strain response summarized in Figure 8-2b

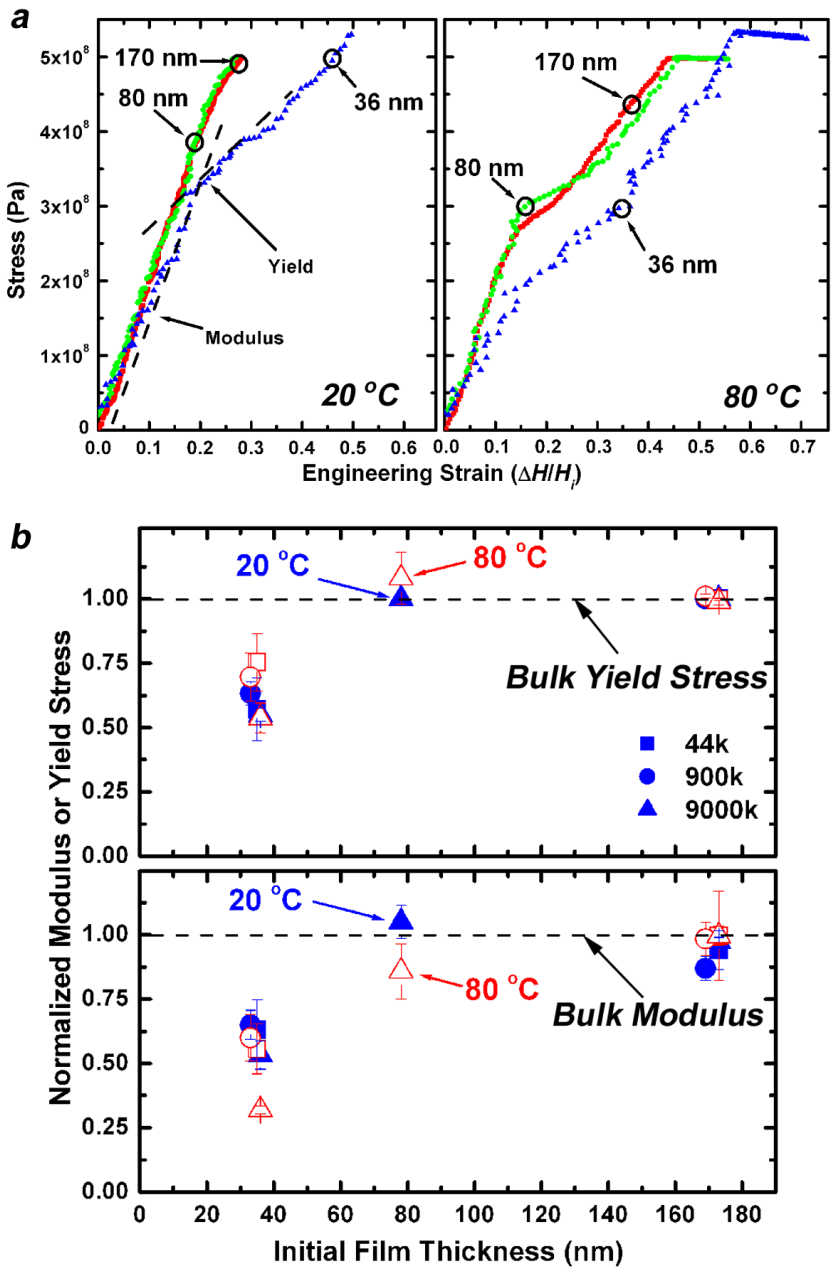

Figure 8-2 PS glassy mechanical properties depend strongly on absolute film thickness. (a) Stress versus strain curves at low load rates for 170 and 36 nm 44k M_W PS and 80 nm 9000k M_W PS at 20 °C and 80 °C. Films of 36 nm show a lower elastic stiffness and yield stress than 80 and 170 nm films. Films of 80 and 170 nm are nearly identical during elastic loading, yield, and post-yield plastic flow. Post-yield plastic flow at 80 °C is similar for both 170 and 36 nm films with a horizontal offset due to lower yield in 36 nm films. (b) At 36 nm film thickness, yield stress and modulus are reduced 25 – 65 % from bulk for all M_W. Yield stress and modulus at each temperature are normalized by the measured bulk value at 170 nm film thickness. The dashed lines correspond to a bulk value normalized to 1. The curves are shifted vertically for clarity. At 36 nm film thickness, 9000k M_W films show slightly lower yield stress and modulus than 44k and 900k M_W films.

indicates that the short-range molecular interactions that govern elastic response are largely independent of M_W, as expected for an entangled polymer film. However, the short-range interactions may act over a distance relevant for the thinnest films in this study.

Our key observation is that short range elastic molecular motions depend dominantly on film thickness and are only slightly dependent on M_W, whereas long range plastic and viscoelastic molecular motions depend on *film thickness and* M_W. Figure 8-3 shows stress versus strain measurements for films of M_W 44k, 900k, and 9000k, where the initial film thickness was 36 nm. At 20 °C and 80 °C, all of these films followed nearly identical linear stress versus strain response up to yield strain. Figure 8-3a and Figure 8-3b show all M_W films yielded near strain 0.2. The yield stress was 290 ± 25 MPa at 20 °C and 190 ± 30 MPa at 80 °C. Films of 44k and 900k M_W showed identical mechanical response over all glassy deformation modes of elastic strain, yield, and post-yield plastic flow. The films of M_W 9000k behaved similarly to the lower M_W films in terms of elastic strain and yield, but had significantly lower plastic flow stress and reduced strain hardening.

Varying the temperature during measurements allows us to separate the effects of short range elastic molecular motions from long range plastic or viscoelastic molecular motions. At high temperature, the polymer molecules are more mobile and thus long range molecular motions can be probed at the same strain rate when there is sufficient time for elastic stresses to relax. Figure 8-3c shows fully viscoelastic loading above T_g at 110 °C, where a 30 °C increase in temperature from Figure 8-3b resulted in fully viscoelastic melt flow, with no observable yield stress. 44k and 900k M_W PS exhibited

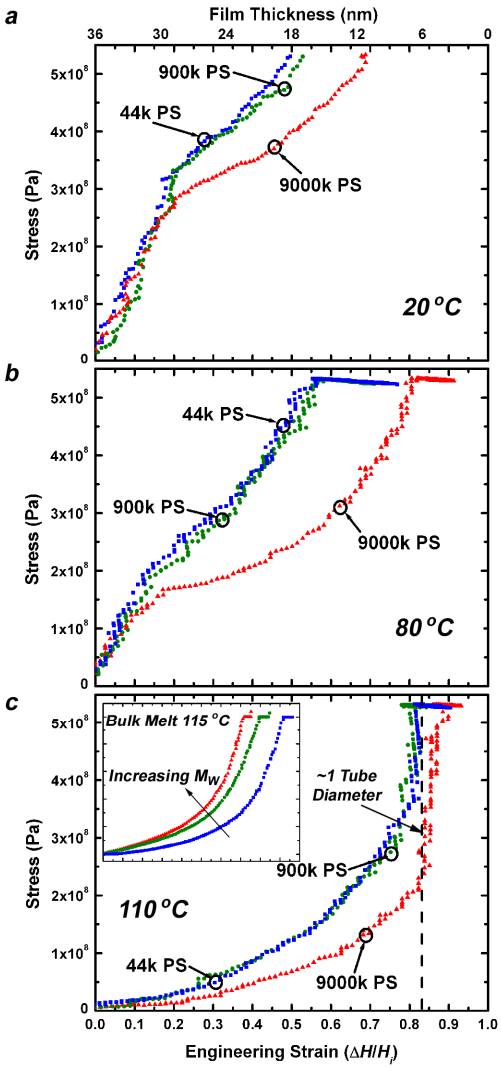

Figure 8-3 Load versus strain curves at 36 nm film thickness for 44k, 900k, and 9000k M_W PS. All materials show similar elastic modulus and yield stress. (a-b) 9000k M_W PS post-yield plastic flow is more compliant than lower M_W PS at 20 and 80 °C while 44k and 900k M_W PS show identical mechanical response. (c) Fully viscoelastic melt response. 9000k M_W PS shows much more compliant viscoelastic behavior at 110 °C than lower M_W PS. All M_W PS show a pronounced kink indicating an increase in material stiffness near strain 0.8 or residual film thickness ~7 nm. The inset shows typical melt response for bulk materials at 170 nm film thickness, with high M_W polymer having higher viscosity than low M_W polymer.

similar viscoelastic melt loading. While the melt response was similar for the films of M_W 44k and 900k, the films of M_W 9000k showed significantly *more compliant* viscoelastic melt flow than the lower M_W PS. The inset in Figure 8-3c shows the

expected bulk scaling from measurements of films of 170 nm initial thickness, where higher M_W films are less compliant than lower M_W films.

For films of 36 nm initial thickness, the higher compliance of 9000k than 44k M_W films indicates a decrease in effective viscosity of 9000k M_W films below the continuum theoretical limit for infinite shear rate viscosity [81, 82, 85]. Figure 8-4 shows the measured viscosity of thin films deviating from bulk theory. In bulk films, the zero shear viscosity of 44k M_W films will be near the zero shear viscosity of M_C = 35k M_W, where the zero shear viscosity of M_C represents the infinite shear rate Rouse viscosity [81, 82, 85, 86]. At initial film thickness 36 nm, the measured effective viscosity of 9000k M_W is lower than the infinite shear rate Rouse viscosity approximated closely by 44k M_W. At initial film thickness 170 nm, measured viscosity of 44k and 900k M_W closely matches expected bulk viscosity values [148], however measured viscosity of 9000k M_W was nearly identical viscosity to that of 900k M_W [148].

The observed behaviors of elastic, plastic, and viscoelastic flows of the films of different thickness and M_W can provide insight into the molecular motions in entangled thin polymer films. For all films measured here, the elastic modulus, associated with short range molecular motions [132, 140], and yield stress, associated with cooperative intramolecular and intermolecular α motions [115, 133, 134, 146, 147], were mostly independent of M_W, as expected from bulk theory of glassy entangled polymers [140]. However, as shown explicitly in Figure 8-2a for 44k M_W and more generally for all M_W,

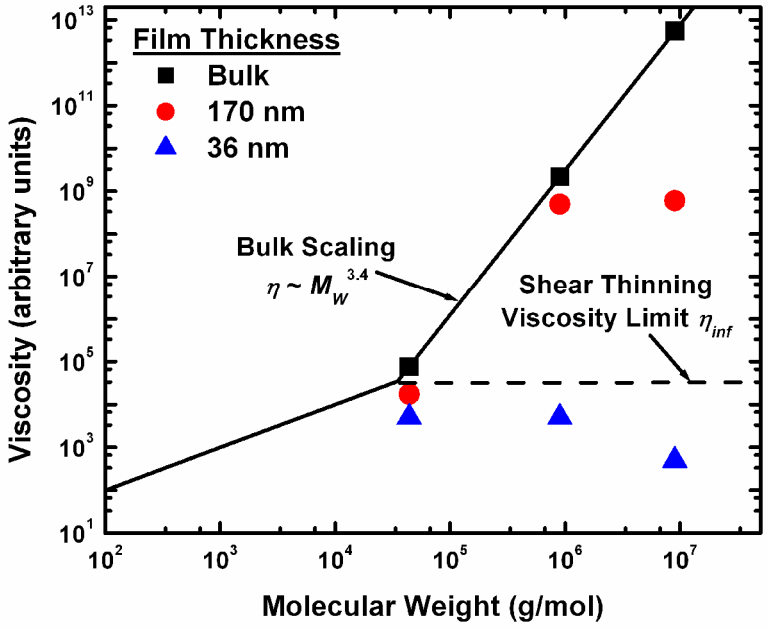

Figure 8-4 Thin film viscosity deviates from bulk theoretical predictions. Values for bulk and 170 nm films represent zero shear viscosities. Values for 36 nm films represent effective viscosities. At 170 nm film thickness, the viscosity of 44k and 900k M_W corresponds closely to bulk values while the viscosity of 9000k M_W is lower than expected. At 36 nm film thickness, the effective viscosity of 9000k MW is lower than the infinite shear rate Rouse viscosity approximated closely by 44k M_W.

the elastic modulus and yield stress of 36 nm films were 25 – 60 % lower than bulk, as evidence of molecular configuration and/or cooperative motions not present in bulk. The enhanced elastic compliance likely results from increasing correlation distance with confinement as film thickness decreases [149] or increasing relative contributions of a highly mobile surface layer [57] to the overall mechanical properties of the film. Any effects of a surface layer observed in these measurements imply the experimental timescale was insufficient to allow polymer structural reorganization between the indenter tool and substrate.

The enhanced cooperativity of short range elastic mobility modes observed here as enhanced elastic compliance is likely the cause of other previously reported

nanoconfinement effects independent of M_W. Thin film buckling experiments have also measured reduced elastic modulus for film thickness < 40 nm independent of PS M_W [135, 150]. Enhanced cooperativity of short range elastic modes in supported PS thin films could also cause the decreasing magnitude of change in thermal expansivity and the broadening of the transition region as T_g is approached upon heating from the glassy state [56, 57, 125, 151-154]. M_W-independent T_g reduction in freely standing PS films for M_W < 380k [139] could also be attributed to enhanced cooperativity of short range elastic mobility modes in thin films.

The enhanced plastic and viscoelastic melt compliance of 9000k M_W films reveals another nanoscale behavior distinct from the M_W-independent enhanced elastic compliance. For all films measured here, 44k and 900k M_W exhibited identical post-yield plastic flow, indicating identical entanglement effects. Films of 9000k M_W also showed identical post-yield plastic flow to films of lower M_W at 80 and 170 nm film thickness. However, 9000k M_W films exhibited much larger post-yield strains than lower M_W films at 36 nm initial film thickness, indicating a reduction of network constraints and entanglements. At temperature above bulk T_g, 36 nm 9000k M_W again showed dramatically *more compliant* fully-yielded viscoelastic melt flow than 36 nm 44k and 900k M_W, reinforcing indications of a reduction of network constraints and entanglements. Similar squeeze flow measurements above T_g at 170 nm film thickness showed the opposite trend, with lower M_W PS more compliant than higher M_W PS [148] as expected from bulk theory [82, 124].

The enhanced post-yield plastic flow and fully-yielded viscoelastic melt flow properties of 36 nm 9000k M_W PS suggests the film was a two-dimensional polymer melt.

The film thickness was initially about 0.4 of the bulk R_g, and was extruded to a thickness of about 0.1 R_g. In this melt of non-ideal segregated polymer chains, the effect of intermolecular interactions and chain overlap were reduced relative to intramolecular interactions [118, 136, 137]. In bulk three-dimensional melts, total chain length affects entanglement spacing only up to a critical molecular weight. Here in two-dimensional melts, this non-intuitive effect of the total chain length above a critical molecular weight affecting an ostensibly much shorter range property is better understood by consideration of the concept of pervaded volume: in two dimensions, the long chain 9000k M_W polymer interferes with the intermolecular entanglement process by excluding foreign chain segments from pervading the space it occupies. This effect of enhanced dynamics due to reduced entanglements at high ratios of R_g to initial film thickness has been similarly observed as M_W-dependent enhanced compliance during tensile testing of thin free standing PS films [136] and M_W-dependent reduced viscosity during dewetting rate studies [103, 145] and squeeze flow nanorheology of PS films [148]. Reduced entanglements in two-dimensional melts are also the likely cause of M_W-dependent reduction in T_g of freely standing PS thin films for M_W > 380k [139]. We hypothesize that this cutoff M_W near 380k observed in freely standing PS films defines the transition point between competing effects of enhanced elastic cooperativity-dominated mechanical properties from reduced entanglement-dominated mechanical properties.

The reduced entanglement structure of two-dimensional melts will also result in a decrease in the α transition temperature T_α from expected bulk values, since intermolecular α motions are directly correlated with chain entanglement. Our large strain measurements of 44k – 9000k M_W PS at initial film thickness 170 – 36 nm support

the reported dielectric [151, 152] and aging [154] measurements that independently measure M_W-dependent T_α and M_W-independent apparent T_g. The glassy post-yield plastic flow and fully-yielded viscoelastic flow measurements of this chapter show reduction of entanglement network constraints in two-dimensional polymer melts [118, 137] governs the observed decrease in T_α as the ratio of film thickness to R_g decreases. The elastic strain and yielding measurements of this chapter show M_W-independent enhanced cooperativity of short range elastic mobility modes governs the observed decrease in and broadening of apparent T_g as film thickness decreases.

The ability to distinguish film thickness-dependent molecular motions from M_W-dependent molecular motions helps clarify conflicting views of thin film M_W-dependency of T_g. The apparent discrepancy is likely due to different measurement techniques probing a different time and length scale of molecular relaxation. M_W-independent nanoconfinement effects on apparent T_g are governed by short range, low strain molecular motions. M_W-dependent nanoconfinement effects on T_α are governed by long range molecular motions of network entanglements. Steady state x-ray reflectivity [125] and ellipsometry measurements [121] that allowed sufficient time for long range α relaxations due to reduced entanglements observed M_W-dependent thin film T_g. Transient ellipsometry [56] and high frequency dielectric [151] measurement methods that probed short time and length scale changes in cooperativity of elastic modes observed no M_W-dependence of T_g nanoconfinement. Somewhat surprisingly, steady state density sensitive fluorescence measurements of T_g did not show M_W-dependent thin film T_g [57, 122]. It is possible that the short 200 nsec timescale of chromophore excited-state

lifetime [155] was only sensitive to the short range rotational fluctuations due to enhanced cooperative coupling of elastic modes.

A point of interest from this data set not yet discussed regards extrusions from initial film thickness 36 nm to residual film thickness below 10 nm. Figure 8-3c shows a sudden increase in material stiffness independent of M_W at 0.8 strain or ~ 7 nm residual film thickness. The increased stiffness was not due to contact of silicon mold and silicon substrate since 44k M_W PS showed creep during the 50 sec hold at 500 MPa. Within experimental error, the residual film thickness at 0.8 strain ranged from 3 to 10 nm. This final residual thickness was on the order of the tube diameter, the size of the cooperatively rearranging region, and the fitted value of a "dead layer" to the measurements of [56]. This monolayer film thickness during drainage flow between nonadhering surfaces is similar to that measured by SFA measurements [108] and perhaps represents the ultimate minimum thickness of mold flash in nanoimprint lithography [1].

8.4 Conclusion

This chapter presents measurements of glassy and viscoelastic polymer mechanical behavior during large strain processing flows at the nanometer scale. We identify the scale-dependent properties of confined entangled polymers and two-dimensional polymer melts. The enhanced compliance of two-dimensional melts could improve molecular-scale molding during NIL. The technique could be adapted to investigate any polymer and compressive deformation geometries while controlling surface interactions. Experiments probing large strain flows in confined geometries can

elucidate outstanding questions and motivate new theoretical insights in polymer dynamics.

CHAPTER 9

SUMMARY AND RECOMMENDATIONS

9.1 Summary

This work presented simulations and experiments investigating the physics underlying polymer deformation during thermomechanical manufacturing of polymer microstructures and nanostructures. The research investigated two main areas of interest: 1) mass transport during micromolding, and 2) polymer mechanical properties during nanomolding at length scales < 100 nm.

The first area of interest investigated polymer flow in microembossing and nanoimprint lithography (NIL) with feature sizes 100 nm – 1 mm to establish rational process design rules for NIL. Microembossing measurements of features 1 – 100 μm showed the influence of mold cavity size resulting in different shapes of polymer deformation. Viscous flow, local stress, and shear-thinning phenomena governed polymer deformation during micromolding. Simulations of microembossing and NIL with feature sizes 100 nm – 1 mm showed polymer deformation and fill time governed by location and rate of polymer shear during imprinting. Dimensionless ratios of mold geometry, polymer thickness, and bulk material and process properties predicted flow by viscous or capillary forces, shape of polymer deformation, and mold fill time. Simulations of embossing molds having irregular spacings and sizes showed individual cavity size dominates replication time, with large differences in individual cavity size resulting in non-uniform, squeeze flow filling. The simulations and experiments of

microembossing and NIL allow for predictive design of molding processes to optimize wafer-scale replication.

The second area of interest investigated polymer mechanical properties at length scales < 100 nm during atomic force microscope (AFM) nanoindentation and nanoscale uniaxial compression and squeeze flow measurements. Continuum simulations of isothermal AFM nanoindentation accurately modeled sub-continuum polymer mechanical deformation based on shear-thinning bulk material behavior. Nonisothermal AFM nanoindentation simulations showed polymer-tip interface temperature to govern the indentation process. Simulation results suggested continuum material models could be improved by modifying bulk material models based on measurements of polymer nanorheological properties. The development of temperature-controlled nanoindentation enabled nanoscale material property characterization of a wide range of materials and temperature-dependent dynamical properties. Nanoscale uniaxial compression and squeeze flow measurements of polymer nanomechanical properties showed initial film thickness determines the entangled state of the polymer. For polymers with film thickness > 100 nm and small molecular size relative to film thickness, bulk polymer mechanics accurately predicted polymer flow during extrusions down to 10 nm residual film thickness. For polymers with large molecular size relative to film thickness, bulk polymer mechanics overpredicted the effects of polymer entanglement. For polymers with film thickness < 100 nm, cooperative polymer motions were distinct from those observed in bulk. The simulations and experiments of nanomolding highlight the importance of nanoscale physical processes distinct from bulk during mechanical processing and could enhance understanding of polymer physics.

9.2 Recommendations and Future Research

This plan for future research addresses measurements of fundamental nanoscale polymer physics and materials properties, design of micro/nanoscale engineering processes by simulation and experiment, and applications of polymer processing technologies for manufacturing of functional integrated systems. The research would seek to develop and enhance nanoscale materials testing capabilities to enable engineering of thermomechanical manufacturing systems that capitalize on the unique properties of nanoscale materials. Figure 9-1 provides an overview of the proposed research.

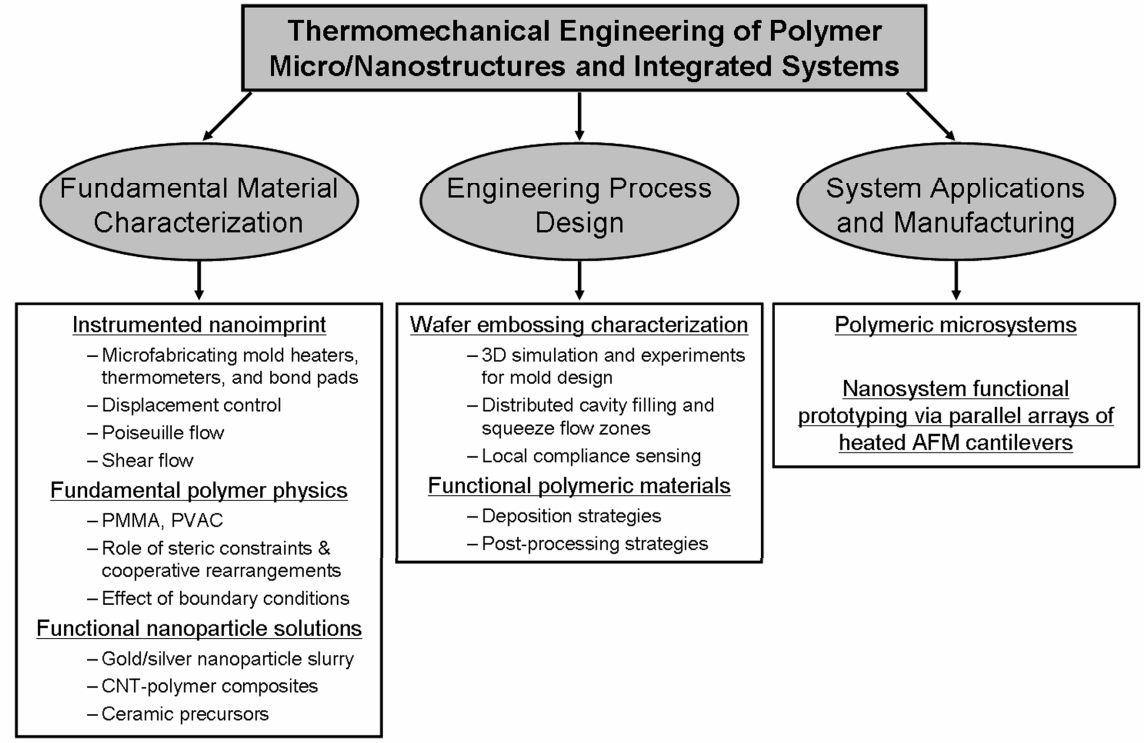

Figure 9-1 Overview of planned future research.

9.2.1 Fundamental Material Characterization

This research would continue investigations of nanoscale material properties and polymer physics. Improvements in control and instrumentation of temperature-controlled instrumented nanoimprint could allow measurements of nanoscale material properties via displacement control during squeeze flows as well as viscometric Couette shear flows and Poiseuille flows. Addition of piezoelectric transducers below the substrate could enable vertical displacement control measurements that allow for true strain rate testing for comparisons to analytical results. Shear piezoelectric transducers could enable horizontal displacement control to investigate Couette shear flows. The ability to probe oscillatory shear would enhance similar tribological measurements of adhesion and friction using the surface force apparatus [156] by allowing measurements on high molecular weight polymer melts in both the glassy and viscoelastic state. Microfabrication of flat punch molds with recessed areas could enable investigation of the properties of flexible polymers in nanopores [157] during coupled Poiseuille and squeeze flows. Improving mold design instrumentation could enable temperature-controlled instrumented nanoimprint on other commercial nanoindentation systems. Current mold fabrication where heaters and thermocouples are fixed to the mold by hand is not optimized. Design and microfabrication of heaters, thermocouples, and bond pads directly integrated into the molds could enable a more robust experimental setup.

Further development of and measurements with local temperature-controlled instrumented nanoimprint could potentially help illucidate outstanding theoretical questions of polymer physics [14]. At film thickness < 100 nm, polymers such as polymethylmethacrylate (PMMA) [158] and polyvinylacetate (PVAC) [123] exhibit

material specific properties not explained by universal bulk characteristics. Instrumented nanoimprint experiments with controlled chemical surface interactions could investigate PMMA, PVAC, PS, and other polymers of controlled tacticity or steric constraints to investigate cooperative length scales of polymer physics. Instrumented nanoimprint experiments could also investigate nanorheological flow properties of colloidal suspensions and mixtures of functional materials in polymers. Understanding the chemical and physical nanorheology of functional materials such as ceramic precursors, colloidal suspensions of gold and silver nanoparticles, and polymer solutions of carbon nanotubes could aid selection of materials and process design for nanosystem manufacturing.

9.2.2 Engineering Process Design

This research would investigate thermomechanical manufacturing processes for micro/nanosystem fabrication. One area of interest would investigate optimized mold design for wafer scale embossing. Defects can arise during wafer scale embossing due to local stress variations and related distortions [159] as well as mold bending [160]. Experiments and simulations would investigate combined polymer and mold deformation mechanisms across disparate length scales during local cavity filling and long range polymer transport. Microfabricated molds with integrated strain sensing would investigate distribution of mold compliance. Flow visualization experiments and 3-dimensional simulations would investigate polymer flow during local cavity filling and squeeze flow coupled with long range polymer transport.

Another area of interest would investigate thermomechanical manufacturing strategies and post-processing chemical reactions for directed deposition of functional

materials. Non-vacuum polymer processing techniques such as spin-casting, roll-coating, inkjet printing, and self assembly would be applied to investigate multi-level functional and structural material deposition strategies. Thermal or radiative curing, sintering, or material removal would probe post-processing techniques to functionalize material. This research would seek to develop materials and processes for polymer-based micro/macroelectronic device fabrication.

9.2.3 System Applications and Manufacturing

This research would integrate knowledge of fundamental nanoscale material properties, thermomechanical process design, and functional material deposition to develop system level applications. Research would investigate fabrication of polymer microsystems as well as applications of heated AFM cantilever arrays as an automated benchtop micro/nanosystem manufacturing platform, similar to stereolithography prototyping. AFM cantilever arrays have been demonstrated for data storage applications [6] and dip pen nanolithography [161]. This work would apply cantilever arrays to locally crosslink polymer and/or sinter ceramic or electronic nanoparticles to create multi-layer three dimensional structures and systems.

REFERENCES

1. Chou, S. and P. Krauss, *Imprint lithography with sub-10 nm feature size and high throughput.* Microelectronic Engineering, 1997. **35**: p. 237-240.

2. Khang, D. and H. Lee, *Wafer-scale sub-micron lithography.* Applied Physics Letters, 1999. **75**: p. 2599-2601.

3. Austin, M.D., et al., *Fabrication of 5 nm linewidth and 14 nm pitch features by nanoimprint lithography.* Applied Physics Letters, 2004. **84**(26): p. 5299-5301.

4. Hua, G., et al., *Polymer Imprint Lithography with Molecular-Scale Resolution.* Nano Letters, 2004. **4**(12): p. 2467-2471.

5. Xu, Q., et al., *Approaching Zero: Using Fractured Crystals in Metrology for Replica Molding.* Journal of American Chemical Society, 2005. **127**: p. 854-855.

6. Vettiger, P., et al., *The "Millipede"-Nanotechnology Entering Data Storage.* IEEE Transactions on Nanotechnology, 2002. **1**(1): p. 39-55.

7. Chui, B.W., et al., *Low-Stiffness Silicon Cantilevers with Integrated Heaters and Piezoresistive Sensors for High-Density AFM Thermomechanical Data Storage.* Journal of Microelectromechanical Systems, 1998. **7**(1): p. 69-78.

8. Guo, L., P. Krauss, and S. Chou, *Nanoscale silicon field effect transistors fabricated using imprint lithography.* Applied Physics Letters, 1997. **71**: p. 1881-1883.

9. Guo, L. and C. Chao, *Polymer microring resonators fabricated by nanoimprint technique.* Journal of Vacuum Science and Technology B, 2002. **20**: p. 2862-2866.

10. Lee, G., et al., *Microfabricated plastic chips by hot embossing methods and their applications for DNA separation and detection.* Sensors and Actuators B, 2001. **75**: p. 142-148.

11. Grochowski, E. and R.F. Hoyt, *Future Trends in Hard Disk Drives.* IEEE Transactions on Magnetics, 1996. **32**: p. 1850-1854.

12. Jung, G.-Y., et al., *Circuit Fabrication at 17 nm Half-Pitch by Nanoimprint Lithography.* Nano Letters, 2006. **6**(3): p. 351-354.

13. Brochard Wyart, F. and P.G. de Gennes, *Viscosity at small scales in polymer melts.* The European Physical Journal E, 2000. **1**: p. 93-97.

14. Alcoutlabi, M. and G.B. McKenna, *Effects of confinement on material behaviour at the nanometre size scale.* Journal of Physics: Condensed Matter, 2005. **17**: p. R461-R524.

15. Charest, J., et al., *Hot embossing for micro patterned cell substrates.* Biomaterials, 2004. **25**: p. 4767-4775.

16. Henderson, C., et al. *Microsystems Manufacturing via Embossing of Thermally Sacrificial Materials*. in *Materials Research Society Symposium*. 2004.

17. Heyderman, L.J., et al., *Flow behaviour of thin polymer films used for hot embossing lithography.* Microelectronic Engineering, 2000. **54**: p. 229-245.

18. Scheer, H.C. and H. Schulz, *A contribution to the flow behaviour of thin polymer films during hot embossing lithography.* Microelectronic Engineering, 2001. **56**: p. 311-332.

19. Juang, Y.-J., L.J. Lee, and K.W. Koelling, *Hot Embossing in Microfabrication. Part I: Experimental.* Polymer Engineering and Science, 2002. **42**(3): p. 539-550.

20. Juang, Y.-J., L.J. Lee, and K.W. Koelling, *Hot Embossing in Microfabrication. Part II: Rheological Characterization and Process Analysis.* Polymer Engineering and Science, 2002. **42**(3): p. 551-566.

21. Shen, X.J., L.-W. Pan, and L. Lin, *Microplastic embossing process: experimental and theoretical characterizations.* Sensors and Actuators A, 2002. **97-98**: p. 428-433.

22. Jeong, J.-H., et al., *Flow Behavior at the Embossing Stage of Nanoimprint Lithography.* Fibers and Polymers, 2002. **3**(3): p. 113-119.

23. Cross, G.L.W., B. O'Connell, and J.B. Pethica. *Mechanical Aspects of Nanoimprint Patterning*. in *Nanoimprint and Nanoprint Technology*. December 2003. Boston, MA.

24. Clariant, *AZ4620 MSDS*.

25. Williams, M.L., R.F. Landel, and J.D. Ferry, *Temperature Dependence of Relaxation Mechanisms.* Journal of American Chemical Society, 1955. **77**: p. 3701-3707.

26. Gere, J.M., *Mechanics of Materials.* 2001: p. 139-143.

27. Yao, D. and B. Kim, *Simulation of the filling process in micro channels for polymeric materials.* Journal of Micromechanics and Microengineering, 2002. **12**: p. 604-610.

28. van Krevelen, D.W., *Properties of Polymers*. 1990, Amsterdam: Elsevier.

29. Rowland, H.D. and W.P. King, *Polymer deformation and filling modes during microembossing.* Journal of Micromechanics and Microengineering, 2004. **14**: p. 1625-1632.

30. Cross, G.L.W., et al., *The Mechanics of Nanoimprint Forming.* Materials Research Society Symposium Proceedings, 2004. **841**.

31. Hirai, Y., et al., *Study of the resist deformation in nanoimprint lithography.* Journal of Vacuum Science and Technology B, 2001. **19**(6): p. 2811-2815.

32. Hirai, Y., et al., *Simulation and experimental study of polymer deformation in nanoimprint lithography.* Journal of Vacuum Science and Technology B, 2004. **22**(6): p. 3288-3293.

33. Martin, C., L. Ressier, and J.P. Peyrade, *Study of PMMA recoveries on micrometric patterns replication by nano-imprint lithography.* Physica E, 2003. **17**: p. 523-525.

34. Haagh, G.A.A.V. and F.N. Van De Vosse, *Simulation of Three-Dimensional Polymer Mould Filling Processes using a Pseudo-Concentration Method.* International Journal for Numerical Methods in Fluids, 1998. **28**: p. 1355-1369.

35. Pitchumani, R., et al. *Analysis of a Process Replication of Electroforming Molds with Integral Microscreens*. in *Micromachining and Microfabrication Process Technology IX*. 2004. San Jose, CA: Proceedings of SPIE.

36. Sackinger, P.A., P.R. Schunk, and R.R. Rao, *A Newton-Raphson Pseudo-Solid Domain Mapping Technique for Free and Moving Boundary Problems: A Finite Element Implementation.* Journal of Computational Physics, 1996. **125**: p. 83-103.

37. Schunk, P.R., et al., *Goma 4.0- A Full-Newton Finite Element Program for Free and Moving Boundary Problems with Coupled Fluid/Solid Momentum, Energy, Mass, and Chemical Species Transport: User's Guide*. 2002, Sandia National Laboratories.

38. Schunk, P.R., *TALE: An Arbitrary Lagrangian-Eulerain Approach to Fluid-Structure Interaction Problems*, in *Sandia Technical Report*. 1999 (unpublished), Sandia National Laboratories.

39. Fuchs, K., C. Friedrich, and J. Weese, *Viscoelastic Properties of Narrow-Distribution Poly(methyl methacrylates).* Macromolecules, 1996. **29**: p. 5893-5901.

40. Fox, R.W. and A.T. McDonald, *Introduction to Fluid Mechanics*. 5th ed. 1998, New York: John Wiley & Sons, Inc. 762.

41. Deen, W.M., *Analysis of Transport Phenomena*. Topics in Chemical Engineering, ed. K.T. Gubbins. 1998, New York: Oxford University Press. 597.

42. Rowland, H.D., et al., *Impact of polymer film thickness and cavity size on polymer flow during embossing: toward process design rules for nanoimprint lithography.* Journal of Micromechanics and Microengineering, 2005. **15**: p. 2414-2425.

43. Cross, G.L.W., et al., *Mechanical Aspects of Nanoimprint Patterning.* IEEE-Nano (San Francisco, 2003), 2003. **2**: p. 494-497.

44. Yu, Z., H. Gao, and S.Y. Chou, *In situ real time process characterization in nanoimprint lithography using time-resolved diffractive scatterometry.* Applied Physics Letters, 2004. **85**(18): p. 4166-4168.

45. Cross, G.L.W., B.S. O'Connell, and J.B. Pethica, *Influence of Elastic Strains on the Mask Ratio in Glassy Polymer Nanoimprint.* Applied Physics Letters, 2005. **86**(8): p. 081902.

46. Gourgon, C., et al., *Influence of pattern density in nanoimprint lithography.* Journal of Vacuum Science and Technology B, 2003. **21**(1): p. 98-105.

47. Schulz, H., M. Wissen, and H.C. Scheer, *Local mass transport and its effect on global pattern replication during hot embossing.* Microelectronic Engineering, 2003. **67-68**: p. 657-663.

48. Young, W.-B., *Analysis of the nanoimprint lithography with a viscous model.* Microelectronic Engineering, 2005. **77**: p. 405-411.

49. Cheng, X. and L.J. Guo, *One-step lithography for various size patterns with a hybrid mask-mold.* Microelectronic Engineering, 2004. **71**: p. 288-293.

50. Colburn, M., et al. *Step and flash imprint lithography: a new approach to high-resolution patterning*. in *SPIE Emerging Lithographic Technologies III*. 1999: SPIE.

51. Xia, Q., et al., *Ultrafast patterning of nanostructures in polymers using laser assisted nanoimprint lithography.* Applied Physics Letters, 2003. **83**(21): p. 4417-4419.

52. Kim, H.Y., K.-s. Kim, and B.-h. Kim. *Micro/nano patterning characteristics in hot embossing process*. in *AIP Conference Proceedings*. 2004.

53. Hua, F., et al., *Polymer Imprint Lithography with Molecular-Scale Resolution.* Nano Letters, 2004. **4**(12): p. 2467-2471.

54. Chou, S.Y., P.R. Krauss, and P.J. Renstrom, *Imprint of sub-25 nm vias and trenches in polymers.* Applied Physics Letters, 1995. **67**(21): p. 3114-3116.

55. Granick, S., et al., *Macromolecules at surfaces: Research challenges and opportunities from tribology to biology.* Journal of Polymer Science Part B-Polymer Physics, 2003. **41**(22): p. 2755-2793.

56. Keddie, J.L., R.A.L. Jones, and R.A. Cory, *Size-dependent depression of the glass-transition temperature in polymer-films.* Europhysics letters, 1994. **27**(1): p. 59-64.

57. Ellison, C.J. and J.M. Torkelson, *The distribution of glass-transition temperatures in nanoscopically confined glass formers.* Nature Materials, 2003. **2**: p. 695-700.

58. Sills, S., et al., *Interfacial glass transition profiles in ultrathin, spin cast polymer films.* Journal of Chemical Physics, 2004. **120**(11): p. 5334-5338.

59. Li, C., et al., *Viscosity Measurements of Very Thin Polymer Films.* Macromolecules, 2005. **38**: p. 5144-5151.

60. Frank, B., et al., *Polymer Mobility in Thin Films.* Macromolecules, 1996. **29**: p. 6531-6534.

61. Mamin, H.J. and D. Rugar, *Thermomechanical writing with an atomic force microscope tip.* Applied Physics Letters, 1992. **61**(8): p. 1003-1005.

62. Brochard, F. and P.G. de Gennes, *Viscosity at small scales in polymer melts.* The European Physical Journal E, 2000. **1**: p. 93-97.

63. Hinz, M., et al., *Temperature dependent nano indentation of thin polymer films with the scanning force microscope.* European Polymer Journal, 2004. **40**: p. 957-964.

64. Miyake, K., N. Satomi, and S. Sasaki, *Elastic modulus of polystyrene film from near surface to bulk measured by nanoindentation using atomic force microscopy.* Applied Physics Letters, 2006. **89**: p. 031925.

65. Sills, S., et al., *Strain shielding and confined plasticity in thin polymer films: Impacts on thermomechanical data storage.* Tribology Letters, 2005. **19**(1): p. 9-15.

66. King, W.P., *Thermomechanical Formation of Polymer Nanostructures*, in *Mechanical Engineering*. 2002, Stanford University: Palo Alto, CA. p. 135.

67. Mackay, M.E., *A Simple Model for the Millipede Write Technique.* IEEE Transactions on Nanotechnology, 2005. **4**(5): p. 641-644.

68. Glotzer, S.C. and W. Paul, *Molecular and Mesoscale Simulation Methods for Polymer Materials.* Annu. Rev. Mater. Res., 2002. **32**: p. 401-436.

69. ten Bosch, B.I.M., *On an extension of Dissipative Particle Dynamics for viscoelastic flow modelling.* Journal of Non-Newtonian Fluid Mechanics, 1999. **83**: p. 231-248.

70. Koumoutsakos, P., *Multiscale Flow Simulations Using Particles.* Annu. Rev. Fluid Mech., 2005. **37**: p. 457-487.

71. Ashbaugh, H.S., et al., *Mesoscale model of polymer melt structure: Self-consistent mapping of molecular correlations to coarse-grained potentials.* Journal of Chemical Physics, 2005. **122**: p. 104908-1 - 104908-5.

72. Cahill, D.G., et al., *Nanoscale thermal transport.* Journal of Applied Physics, 2003. **93**(2): p. 793-818.

73. Schunk, P.R., et al., *Goma 4.0- A Full-Newton Finite Element Program for Free and Moving Boundary Problems with Coupled Fluid/Solid Momentum, Energy, Mass, and Chemical Species Transport: User's Guide.* Sandia National Laboratories Technical Report, 2002. **SAND2002-3204**.

74. Stay, M.S. and V.H. Barocas, *Couple lubrication and Stokes flow finite elements.* International Journal for Numerical Methods in Fluids, 2003. **43**(2): p. 129-146.

75. Fan, H.Y., et al., *Rapid prototyping of patterned functional nanostructures.* Letters to Nature, 2000. **405**(6782): p. 56-60.

76. Rowland, H.D., et al., *Simulations of nonuniform embossing: The effect of asymmetric neighbor cavities on polymer flow during nanoimprint lithography.* Journal of Vacuum Science and Technology B, 2005. **23**(6): p. 2958-2962.

77. Sethian, J.A., *Level Set Methods and Fast Marching Methods*. 1999: Cambridge University Press.

78. Baer, T.A., et al. *A Level Set Approach to 3D Mold Filling of Newtonian Fluids*. in *ASME Symposium on Flows in Manufacturing Processes*. 2003. Honolulu, Hawaii.

79. Granick, S., H.-W. Hu, and G.A. Carson, *Nanorheology of Confined Polymer Melts. 2. Nonlinear Shear Response at Strongly Adsorbing Surfaces.* Langmuir, 1994. **10**: p. 3867-3873.

80. Awati, K.M., et al., *Wall slip and shear stresses of polymer melts at high shear rates without pressure and viscous heating effects.* Journal of Non-Newtonian Fluid Mechanics, 2000. **89**: p. 117-131.

81. Tsenoglou, C., *Non-Newtonian Rheology of Entangled Polymer Solution and Melts.* Macromolecules, 2001. **34**: p. 2148-2155.

82. Doi, M. and S.F. Edwards, *The Theory of Polymer Dynamics*. The International Series of Monographs on Physics, ed. J. Birman, et al. Vol. 73. 1999, Oxford: Oxford University Press.

83. Wapperom, P. and R. Keunings, *Simulation of linear polymer melts in transient complex flow.* Journal of Non-Newtonian Fluid Mechanics, 2000. **95**: p. 67-83.

84. Cox, W.P. and E.H. Merz, *Correlation of Dynamic and Steady Flow Viscosities.* Journal of Polymer Science, 1958. **28**(118): p. 619-622.

85. Graessley, W.W., *Some Phenomenological Consequences of the Doi-Edwards Theory of Viscoelasticity.* Journal of Polymer Science: Polymer Physics Edition, 1980. **18**(1): p. 27-34.

86. Hieber, C.A. and H.H. Chiang, *Some correlations involving the shear viscosity of polystyrene melts.* Rheologica Acta, 1989. **28**(4): p. 321-332.

87. Priestley, R.D., L.J. Broadbelt, and J.M. Torkelson, *Physical Aging of Ultrathin Polymer Films above and below the Bulk Glass Transition Temperature: Effects of Attractive vs Neutral Polymer-Substrate Interactions Measured by Fluorescence.* Macromolecules, 2005. **38**: p. 654-657.

88. Fryer, D.S., P.F. Nealey, and J.J. de Pablo, *Thermal Probe Measurements of the Glass Transition Temperature for Ultrathin Polymer Films as a Function of Thickness.* Macromolecules, 2000. **33**: p. 6439-6447.

89. Frank, C.W., et al., *Structure in Thin and Ultrathin Spin-Cast Polymer Films.* Science, 1996. **273**: p. 912-915.

90. Panton, R.L., *Incompressible Flow*. 2nd ed. 1996: John Wiley & Sons, Inc. 837.

91. Capella, B. and G. Dietler, *Force-distance curves by atomic force microscopy.* Surface Science Reports, 1999. **34**: p. 1-104.

92. Phan-Thien, N., et al., *Squeeze Film Flow of Ideal Elastic Liquids.* Journal of Non-Newtonian Fluid Mechanics, 1985. **18**: p. 227-254.

93. Brenner, H., *The slow motion of a sphere through a viscous fluid towards a plane surface.* Chemical Engineering Science, 1961. **16**: p. 242-251.

94. Nelson, B.A. and W.P. King, *Measuring material softening with nanoscale spatial resolution using heated silicon probes.* Review of Scientific Instruments, 2007. **78**: p. 023702.

95. Stevens, J.R., et al., *The pressure variation of the glass transition temperature in atactic polystyrene.* Journal of Chemical Physics, 1986. **84**(2): p. 1006-1014.

96. Priestley, R.D., et al., *Structural Relaxation of Polymer Glasses at Surfaces, Interfaces, and In Between.* Science, 2005. **309**: p. 456-459.

97. Kurabayashi, K., et al., *Measurement of the thermal conductivity anisotropy in polyimide films.* Journal of Microelectromechanical Systems, 1999. **8**: p. 180-191.

98. Bhushan, B., *Handbook of Nanotechnology*. 2004, Berlin, Germany: Springer-Verlag. 1222.

99. Jackson, C.L. and G.B. McKenna, *The glass transition of organic liquids confined to small pores.* Journal of Non-Crystalline Solids, 1991. **131-133**: p. 221-224.

100. Reiter, G., *Dewetting of Thin Polymer films.* Physical Review Letters, 1992. **68**(1): p. 75-78.

101. Reiter, G., *Mobility of polymers in films thinner than their unperturbed size.* Europhysics letters, 1993. **23**(8): p. 579-584.

102. Reiter, G., et al., *Residual stresses in thin polymer films cause rupture and dominate early stages of dewetting.* Nature Materials, 2005. **4**: p. 754-758.

103. Xavier, J.H., et al., *Dynamics of Ultrathin Films in the Glassy State.* Langmuir, 2005. **21**: p. 5069-5072.

104. Bodiguel, H. and C. Fretigny, *Viscoelastic dewetting of a polymer film on a liquid substrate.* The European Physical Journal E, 2006. **19**: p. 185-193.

105. Chan, D.Y.C. and R.G. Horn, *The drainage of thin liquid films between solid surfaces.* Journal of Chemical Physics, 1985. **83**(10): p. 5311-5324.

106. Israelachvili, J.N., *Measurements of the viscosity of thin fluid films between two surfaces with and without adsorbed polymers.* Colloid & Polymer Science, 1986. **264**: p. 1060-1065.

107. Hu, H.-W. and S. Granick, *Viscoelastic Dynamics of Confined Polymer Melts.* Science, 1992. **258**: p. 1339-1342.

108. Peanasky, J., L.L. Cai, and S. Granick, *Nanorheology of Confined Polymer Melts. 3. Weakly Adsorbing Surfaces.* Langmuir, 1994. **10**: p. 3874-3879.

109. Granick, S. and H.-W. Hu, *Nanorheology of Confined Polymer Melts. 1. Linear Shear Response at Strongly Adsorbing Surfaces.* Langmuir, 1994. **10**: p. 3857-3866.

110. VanLandingham, M.R., et al., *Nanoindentation of Polymers: An Overview.* Macromolecules Symposia, 2001. **167**: p. 15-43.

111. O'Connell, B.S. and G. Cross, *(unpublished).* 2006.

112. Schuh, C.A., C.E. Packard, and A.C. Lund, *Nanoindentation and contact-mode imaging at high temperatures.* Journal of Materials Research, 2006. **21**(3): p. 725-736.

113. Schuh, C.A., J.K. Mason, and A.C. Lund, *Quanitative insight into dislocation nucleation from high-temperature nanoindentation experiments.* Nature Materials, 2005. **4**: p. 617-621.

114. Beake, B.D. and J.F. Smith, *High-temperature nanoindentation testing of fused silica and other materials.* Philosophical Magazine A, 2002. **82**(10): p. 2179-2186.

115. Quinson, R., et al., *Yield criteria for amorphous glassy polymers.* Journal of Materials Science, 1997. **32**: p. 1371-1379.

116. Cross, G.L.W., *The production of nanostructures by mechanical forming.* Journal of Physics D: Applied Physics, 2006. **39**: p. R363-R386.

117. Schulz, H., et al., *Impact of molecular weight of polymers and shear rate effects for nanoimprint lithography.* Microelectronic Engineering, 2006. **83**: p. 259-280.

118. De Gennes, P.G., *Scaling Concepts in Polymer Physics*. 1979: Cornell University Press. 324.

119. Jones, R.L., et al., *Chain conformation in ultrathin polymer films.* Letters to Nature, 1999. **400**: p. 146-149.

120. Forrest, J.A., *A decade of dynamics in thin films of polystyrene: Where are we now?* The European Physical Journal E, 2002. **8**: p. 261-266.

121. Singh, L., P.J. Ludovice, and C.L. Henderson, *Influence of molecular weight and film thickness on the glass transition temperature and coefficient of thermal expansion of supported ultrathin polymer films.* Thin Solid Films, 2004. **449**: p. 231-241.

122. Ellison, C.J., M.K. Mundra, and J.M. Torkelson, *Impacts of Polystyrene Molecular Weight and Modification to the Repeat Unit Structure on the Glass Transition-Nanoconfinement Effect and the Cooperativity Length Scale.* Macromolecules, 2005. **38**: p. 1767-1778.

123. O'Connell, P.A. and G.B. McKenna, *Rheological Measurements of the Thermoviscoelastic Response of Ultrathin Polymer Films.* Science, 2005. **307**: p. 1760-1763.

124. Ferry, J.D., *Viscoelastic Properties of Polymers*. 3rd ed. 1980, New York, NY: John Wiley & Sons. 641.

125. Miyazaki, T., K. Nishida, and T. Kanaya, *Thermal expansion behavior of ultrathin polymer films supported on silicon substrate.* Physical Review E, 2004. **69**: p. 061803-1 - 061803-6.

126. This work, *Chapter 6.*

127. Schulz, H., et al., *Choice of the molecular weight of an imprint polymer for hot embossing lithography.* Microelectronic Engineering, 2005. **78-79**: p. 625-632.

128. Hsu, T.C. and I.R. Harrison, *Measurement of the Equibiaxial Elongational Viscosity of Polystyrene using Lubricated Squeezing.* Polymer Engineering and Science, 1992. **32**(14): p. 931-938.

129. Laun, H.M., *Rheometry towards complex flows-squeeze flow technique.* Makromolekulare Chemie-Macromolecular Symposia, 1992. **56**: p. 55-66.

130. Macosko, C.M., *Rheology: Principles, Measurements, and Applications*. 1994, New York: Wiley-VCH. 550.

131. Richeton, J., et al., *Influence of temperature and strain rate on the mechanical behavior of three amorphous polymers: Characterization and modeling of the compressive yield stress.* International Journal of Solids and Structures, 2006. **43**: p. 2318-2335.

132. Tanguy, A., F. Leonforte, and J.-L. Barrat, *Plastic response of a 2D Lennard-Jones amorphous solid: Detailed analysis of the local rearrangements at very slow strain rate.* The European Physical Journal E, 2006. **20**: p. 355-364.

133. Robertson, R.E., *Theory for the Plasticity of Glassy Polymers.* Journal of Chemical Physics, 1966. **44**(10): p. 3950-3956.

134. Wu, J.J. and C.P. Buckley, *Plastic Deformation of Glassy Polystyrene: A Unified Model of Yield and the Role of Chain Length.* Journal of Polymer Science: Part B: Polymer Physics, 2004. **42**: p. 2027-2040.

135. Stafford, C.M., et al., *Elastic Moduli of Ultrathin Amorphous Polymer Films.* Macromolecules, 2006. **39**: p. 5095-5099.

136. Si, L., et al., *Chain Entanglement in Thin Freestanding Polymer Films.* Physical Review Letters, 2005. **94**: p. 127801-1 - 127801-5.

137. Brown, H.R. and T. Russell, *Entanglements at Polymer Surfaces and Interfaces.* Macromolecules, 1996. **29**: p. 798-800.

138. Lyulin, A.V., et al., *Molecular Dynamics Simulation of Uniaxial Deformation of Glassy Amorphous Atactic Polystyrene.* Macromolecules, 2004. **37**: p. 8785-8793.

139. Dalnoki-Veress, K., et al., *Molecular weight dependence of reductions in the glass transition temperature of thin, freely standing polymer films.* Physical Review E, 2001. **63**: p. 031801.

140. Haward, R.N., *The Physics of Glassy Polymers*. 2 ed. 1997, New York: Applied Science Publishers Ltd. 620.

141. De Gennes, P.G., *Glass transitions in thin polymer films.* The European Physical Journal E, 2000. **2**: p. 201-205.

142. Ngai, K.L., *Mobility in thin polymer films ranging from local segmental motion, Rouse modes to whole chain motion: A coupling consideration.* The European Physical Journal E, 2002. **8**: p. 225-235.

143. Johannsmann, D., *The glass transition and contact mechanical experiments on polymer surfaces.* The European Physical Journal E, 2002. **8**: p. 257-259.

144. Zhao, J.-H., et al., *Thermal stress and glass transition of ultrathin polystyrene films.* Applied Physics Letters, 2000. **77**(18): p. 2843-2845.

145. Bodiguel, H. and C. Fretigny, *Reduced Viscosity in Thin Polymer Films.* Physical Review Letters, 2006. **97**: p. 266105.

146. Argon, A.S., *A theory for the low-temperature plastic deformation of glassy polymers.* Philosophical Magazine, 1973. **28**: p. 839-865.

147. Richeton, J., et al., *A formulation of the cooperative model for the yield stress of amorphous polymers for a wide range of strain rates and temperatures.* Polymer, 2005. **46**: p. 6035-6043.

148. This work, *Chapter 7.*

149. Leonforte, F., et al., *Continuum limit of amorphous elastic bodies. III. Three-dimensional systems.* Physical Review B, 2005. **72**: p. 224206.

150. Stafford, C.M., et al., *A buckling-based metrology for measuring the elastic moduli of polymeric thin films.* Nature Materials, 2004. **3**: p. 545-550.

151. Fukao, K. and Y. Miyamoto, *Glass transition temperature and dynamics of alpha-process in thin polymer films.* Europhysics letters, 1999. **46**(5): p. 649-654.

152. Fukao, K., et al., *Relaxation dynamics in thin supported polymer films.* Journal of Non-Crystalline Solids, 2002. **307-310**: p. 517-523.

153. Kawana, S. and R.A.L. Jones, *Character of the glass transition in thin supported polymer films.* Physical Review E, 2001. **63**: p. 021501.

154. Kawana, S. and R.A.L. Jones, *Effect of physical ageing in thin glassy polymer films.* The European Physical Journal E, 2003. **10**: p. 223-230.

155. Hall, D.B., A. Dhinojwala, and J.M. Torkelson, *Translation-Rotation Paradox for Diffusion in Glass-Forming Polymers: The Role of the Temperature Dependence of the Relaxation Time Distribution.* Physical Review Letters, 1997. **79**(1): p. 103-106.

156. Maeda, N., et al., *Adhesion and Friction Mechanisms of Polymer-on-Polymer Surfaces.* Science, 2002. **297**: p. 379-382.

157. De Gennes, P.G., *Flexible Polymers in Nanopores.* Advances in Polymer Science, 1999. **138**: p. 92-105.

158. Roth, C.B., et al., *Molecular-weight dependence of the glass transition temperature of freely-standing poly(methyl methacrylate) films.* The European Physical Journal E, 2006. **20**: p. 441-448.

159. Li, N., W. Wu, and S.Y. Chou, *Sub-20-nm Alignment in Nanoimprint Lithography Using Moire Fringe.* Nano Letters, 2006. **6**(11): p. 2626-2629.

160. McClelland, G.M., et al., *Contact mechanics of a flexible imprinter for photocured nanoimprint lithography.* Tribology Letters, 2005. **19**(1): p. 59-63.

161. Salaita, K., et al., *Sub-100 nm, Centimeter-Scale, Parallel Dip-Pen Nanolithography.* Small, 2005. **1**: p. 940-945.